Innovative control techniques of a modular multilevel converter for improving the efficiency of electrified ships

Original Citation:
Innovative control techniques of a modular multilevel converter for improving the efficiency of electrified ships / D'Amato, Davide. - ELETTRONICO. - (2024). [10.60576/poliba/iris/d-amato-davide_phd2024]

Published version
Politecnico di Bari
DOI:10.60576/poliba/iris/d-amato-davide_phd2024

Politecnico
di Bari

Department of Electrical and Information Engineering

ELECTRICAL AND INFORMATION ENGINEERING

Ph.D. Program

SSD: ING/IND-32 - CONVERTERS, ELECTRICAL MACHINES AND DRIVES

Final Dissertation

Innovative Control Techniques of a Modular Multilevel Converter for Improving the Efficiency of Electrified Ships

by

Davide D'Amato

Supervisor:

Prof. Vito Giuseppe Monopoli

Coordinator of Ph.D Program:

Prof. Mario Carpentieri

XXXVI Cycle - November 1st, 2020 - October 31st, 2023

Abstract (eng)

This thesis work reports the results of three years of activities carried out during the XXXVI cycle of the doctoral course in Electrical and Information Engineering at Bari Polytechnic University. The PhD is funded by Isotta Fraschini Motori S.p.A., a company of Fincantieri S.p.A. The title of the PhD research activity program is ”Hybrid-electric propulsion systems for naval applications”. Indeed, Isotta Fraschini Motori S.p.A. has the aim to develop a naval propulsion system based on innovative technologies to minimize operating costs, fuel consumption, and greenhouse gas emissions into the atmosphere as required by the objectives set by the European Union. Therefore, during the three years of the Ph.D. program, short-term research activities with a high level of Technology Readiness Level (TRL) are carried out for company work, and research activities with a low TRL have been developed at the Power Electronics laboratory of the Politecnico di Bari. The activities carried out at the company during the three years of the Ph.D. program include design optimization of a new diesel generator for Medium Voltage Direct Current marine applications, preliminary design of a shipboard hybrid propulsion system, and sizing of a shipboard power generation system consisting of batteries and fuel cells. The latter project is carried out abroad at the Norwegian University of Science and Technology NTNU in Aalesund in collaboration with Vard Electro S.r.l, a company of Fincantieri S.p.A.

The main objective of this work is to study the control techniques of Modular Multilevel Converter in DC Medium Voltage for marine applications. Modular Multilevel Converters are becoming increasingly attractive for many high-voltage and high-power applications. However, due to their topology and operation, they present technical challenges in control system implementation, such as balancing submodule capacitor voltages and suppressing circulating currents. The circulating current introduces additional power losses, increases the current stress on power devices, and reduces their lifetime. Specifically, in this thesis work, a novel control technique is proposed for eliminating circulating current by injecting a low-frequency alternating signal into a single submodule of each converter arm, to also achieve a reduction in voltage ripple across capacitors, benefiting their lifetime.

The proposed control technique will be described in detail both through the analytical model of the circular interactions governing the operation of the MMC and through simulations and experimental tests on the set-up present at the Power Electronics Laboratory of the Politecnico di Bari. The entire prototype of the three-phase modular multilevel converter was designed, implemented, and tested during the research activity carried out at the university. The analytical steady-state model of the Modular Multilevel Converter is intended to describe mathematically the expressions of the harmonics of the electrical quantities present in the converter so that the effects of the injection signal on converter performance can be investigated and guidelines for calibration of the proposed control can be defined. Experimental results performed on a seven-level converter are presented to validate the proposed technique and compare its performance over techniques already present in the literature. The proposed control can suppress the circulating current flowing in the converter and reduce the voltage ripple, improving the efficiency of the converter and reducing the overall power losses. Eventually, the same technique is extended to pursue another control objective, namely, balancing the voltages of the submodule capacitors. The proposed technique has been validated through experimental results showing good performance.

Abstract (it)

Questo lavoro di tesi riporta i risultati di tre anni di attività svolte durante il XXXVI ciclo del corso di dottorato in Ingegneria Elettrica e dell'Informazione del Politecnico di Bari. La borsa di studio è finanziata da Isotta Fraschini Motori S.p.A., un Azienda del gruppo Fincantieri S.p.A., dal titolo "Sistemi di propulsione ibridi-elettrici per applicazioni navali". Isotta Fraschini Motori S.p.A ha come obiettivo di sviluppare un sistema di propulsione navale basato su tecnologie innovative per minimizzare i costi operativi, il consumo di carburante e le emissioni di gas serra nell'atmosfera come richiesto dagli obiettivi fissati dall'Unione Europea. Pertanto, durante i tre anni di dottorato sono state svolte attività di ricerca a breve termine con un livello di maturità tecnologica, Technology Readiness Level (TRL), alta per lavori aziendali e attività di ricerca sviluppate in laboratorio con un TRL basso. Le attività svolte in Azienda durante i tre anni di dottorato comprendono l'ottimizzazione della progettazione di un nuovo generatore diesel per applicazioni marine in Media Tensione in Corrente Continua, la progettazione preliminare di un sistema di propulsione ibrido a bordo nave e il dimensionamento di un sistema di generazione dell'energia elettrica a bordo nave composto da batterie e celle a combustibile. Quest'ultimo progetto è stato svolto all'estero presso l'università norvegese di scienza e tecnologia NTNU ad Alesund in collaborazione con Vard Electro S.r.l Azienda del gruppo di Fincantieri S.p.A.

L'obiettivo principale di questo lavoro è lo studio delle tecniche di controllo del Convertitore Modulare Multilivello in media tensione in corrente continua per

applicazioni marine. I convertitori modulari multilivello stanno diventando sempre più interessanti per molte applicazioni ad alta tensione e ad alta potenza. Tuttavia, a causa della loro topologia e del loro funzionamento, presentano sfide tecniche nell'implementazione del sistema di controllo, come il bilanciamento delle tensioni dei condensatori dei sottomoduli e la soppressione delle correnti di circolazione. La corrente di circolazione introduce ulteriori perdite di potenza, aumenta la sollecitazione di corrente sui dispositivi di potenza e ne riduce la durata. In particolare, in questo lavoro viene proposta una tecnica di controllo innovativa per l'eliminazione della corrente di circolazione iniettando un segnale alternato a bassa frequenza in un singolo sottomodulo di ciascun braccio del convertitore, per ottenere anche una riduzione del ripple di tensione attraverso i condensatori, a vantaggio della loro durata.

La tecnica di controllo proposta sarà descritta dettagliatamente sia attraverso l'analisi analitica delle interazioni circolari che governano il funzionamento del MMC che attraverso simulazioni e test sperimentali sul set-up presente presso il laboratorio di Elettronica di Potenza del Politecnico di Bari. L'intero prototipo del convertitore modulare multilivello trifase è stato progettato, implementato e testato durante l'attività di ricerca svolta in Università. Il modello analitico dello stato stazionario del convertitore modulare multilivello ha lo scopo di esprimere analiticamente le espressioni delle armoniche delle grandezze elettriche tensione e corrente presenti nel convertitore in modo da poter approfondire gli effetti del seganle di iniezione sulle performance del convertitore e definire delle linee guida per la taratura del controllo proposto. I risultati sperimentali eseguiti su un convertitore a sette livelli sono presentati per convalidare la tecnica proposta e confrontare le prestazioni rispetto agli approcci già presenti in letteratura. Il controllo proposto è in grado di sopprimere la corrente circolante che scorre nella maglia interna del convertitore e ridurre il ripple di tensione, migliorando l'efficienza del convertitore e riducendo le perdite di potenza complessive. In fine, la stessa tecnica è stata estesa per perseguire un altro obiettivo di controllo, ovvero il bilanciamento delle tensioni dei condensatori dei sottomoduli del convertitore. La tecnica proposta è stata validata attaverso i risultati sperimentali mostrando delle buone performance.

”Non è elettronica di potenza se non esplode !”

Ringraziamenti

Il lavoro di tesi di Dottorato è uno dei più impegnativi, perchè è frutto di un percorso formativo e di crescita personale nel quale si sceglie di mettersi personalmente in gioco. Pertanto desidero ringraziare il Politecnico di Bari e Isotta Fraschini Motori S.p.A per avermi offerto l'opportunità di intraprendere il Dottorato di Ricerca e di avermi accolto in Azienda.

Ringrazio sinceramente il mio Tutor, Prof. Vito Giuseppe Monopoli per avermi dato l'opportunità di entrare a contatto con il mondo della ricerca, per la sua guida instancabile, il suo costante sostegno, per i suoi preziosi consigli ed insegnamenti. Collaborare al suo fianco è stato un privilegio, arricchendo il mio bagaglio tecnico e umano. Grazie, Prof. per avermi offerto l'opportunità di contribuire alla crescita del gruppo di Elettronica di Potenza del Politecnico di Bari.

Un ringraziamento speciale va a Rinaldo Consoletti, il ”Boss” del laboratorio, il cui contributo è stato fondamentale. Le sue maniere burbere, animalesche e brutali nascondono saggezza ed esperienza, hanno sicuramente contribuito a plasmare il mio percorso accademico e personale.

Grazie Riccardo, che nel corso dell'ultimo anno di dottorato hai dimostrato una dedizione straordinaria nel seguirmi e nell'aiutarmi a migliorare tecnicamente.

Un ringraziamento affettuoso a Lara e a Gianmarco, compagni di avventure di dottorato. Grazie per la vostra compagnia, il vostro sostegno morale e le risate condivise che hanno reso più leggero questo percorso impegnativo.

Desidero inoltre esprimere la mia gratitudine ai ragazzi e alle ragazze che ho avuto l'onore di seguire per il loro lavoro di tesi durante i tre anni di dottorato: Carmen, Michelangelo, Valentina, Michele, Caterina, Luca e Nicoletta. Ognuno di voi ha contribuito in modo unico al mio percorso, trasmettendo esperienze preziose. Il vostro impegno e la vostra dedizione sono stati fonte di ispirazione.

Desidero ringraziare la mia famiglia, mio padre Vito, mia madre Annamaria e i miei due fratelli Giuseppe e Diego per avermi sopportato e supportato durante tutto questo percorso. Mi sento incredibilmente fortunato ad aver incontrato Simona, la mia straordinaria ragazza. La sua presenza nella mia vita ha portato gioia, amore e una leggerezza che ha reso ogni momento speciale. Grazie per tutti i bellissimi momenti condivisi, per il coraggio che mi hai trasmesso e per il continuo sostegno che mi offri, rendendo questo percorso più facile da affrontare. Sono grato per la tua presenza costante nella mia vita.

Contents

List of Figures

Chapter 1

Introduction

New generations of ships face new challenges, especially in terms of energy efficiency, environmental impact, and increased reliability. One of the future goals of shipbuilding is to reduce the impact of ship emissions to satisfy the existing and future International Maritime Organization (IMO) regulations on greenhouse gas emissions and pollution. Today, the trend to design more efficient and versatile ships leads to the development of hybrid propulsion systems and new power generation systems using thermal engines, electric motors, battery and fuel cell storage systems. In this context, Isotta Fraschini Motori S.p.A. funded my doctoral research project entitled ”Hybrid-electric propulsion systems for marine applications” with the objective of developing a marine propulsion system based on innovative technologies to minimize operating costs, fuel consumption and greenhouse gas emissions to the atmosphere as required by the targets set by the European Union.

During the three years of my doctoral research project, I carried out various activities both in the company and in the research laboratory of Power Elettronics at the Politecnico di Bari. These works can be split into short-term research activities with a high level of technological maturity, Technology Readiness Level (TRL), for company works and research activities developed in the laboratory with a low TRL.

This thesis work described all the activities that I conducted during my industrial PhD work, as well as the results that I developed on the experimental set-up reflected in research papers published and submitted to scientific journals in the field of Power Electronics.

1.1 Energy Transition in Marine Transportation

Since the XVIII century, with the first industrial revolution, to the present day, the use of energy resources has greatly improved the living conditions of human beings. The industrialisation has made energy widely accessible and usable through the development of new and advanced distribution systems. However, this intensive exploitation of non-renewable resources has caused environmental problems such as pollution. Today, the main challenge is to find sustainable ways to meet the growing global demand for energy through the energy transition to renewable energy sources [1]. Renewable energy sources (RES) are playing an increasingly important role in the formulation of many governments' sustainable development strategies [2, 3]. However, the transition from traditional fossil fuels to RES is a complex task that requires effective coordination of resource management, technological innovation and policy advocacy [4]. The directives proposed by the European Commission in 2008 concerning climate and energy, within the framework of Horizon 2020 [5], focus on two main objectives: the reduction of greenhouse gas emissions and the increase of renewable energy production. One of the central elements is the electrification of transport, which is regarded as one of the first goals to be achieved. The transport sector is a major source of greenhouse gas emissions, contributing 25% of total CO2 emissions in Europe. Consequently, the electrification of means of transport has become one of the central objectives in international treaties to reduce CO2 emissions and promote the use of renewable energy sources [5–8]. Although the rail sector is considered an environmentally friendly option due to its low greenhouse gas emissions per passenger transported, it still contributes 4.2 $\%$ (336 million tons of CO_2) to total global transport emissions [8]. Maritime transport has seen an increase in greenhouse gas emissions in recent years and the need for stricter regulations to reduce pollution has arisen. The International Maritime Organisation (IMO) [9], a specialised agency of the United Nations, plays a crucial role in establishing international regulations to tackle marine pollution and greenhouse gas emissions from ships. Its primary function is to establish a fair and effective regulatory framework for the shipping industry and to promote the universal adoption of these rules. The Marine Environment Protection Committee at its 75th session (MEPC 75), held from 30 March to 3 April 2020, deliberated on important amendments to MARPOL Annex VI [10]. These amendments concern the implementation of a maximum limit of 0.50 $\%$ sulphur in fuels used on board ships. The strict enforcement of this standard, which entered into force on 1 January 2020, plays a key role in promoting a cohesive and effective implementation of this global sulphur limit. The aim of these changes is to significantly reduce emissions of air pollutants containing SO_x and particulate matter from ships' combustion engines, protecting both human health and the marine environment. A further parameter to be considered is the maximum permissible sulphur content of marine fuels in so-called Emission Control Areas (ECAs), or sulfur emission control areas (SECAs), set at 0.1 $\%$ [11]. Dealing with current and future IMO regulations on greenhouse gas emissions and pollutants requires considerable effort for all industries and companies working in this sector. Indeed, the design of new generations of ships is focused on minimising fuel consumption and reducing CO_2 emissions. The electrification of propulsion systems and the integration of renewable energy sources into the on-board power distribution network emerge as key solutions for developing more efficient and environmentally friendly ships.

1.1.1 Medium Voltage Direct Current System

Strict regulations have introduced new challenges for ship designers and owners, leading to the development of new generations of ships with both hybrid diesel/electric and fully electric propulsion systems [12] and with the possibility of interconnecting to new sources of low-emission electricity generation such as fuel cells [13]. However, it is well to clarify that electric propulsion is not a new concept, but is a propulsion configuration that has been widely used since the early 20th century for different types of vessels such as cruise ships, icebreakers, research vessels and submarines have implemented electrical motors for flexible manoeuvring during their operations and low emissions [14–16]. Today, the majority of full-electric ships utilize alternating current (AC) distribution systems [17]. However, in recent years, there has been a growing interest in high and medium voltage direct current (DC) electrical transmission systems on board ships, driven by advancements in power electronics and the integration of new renewable energy sources [18–20].

These DC systems offer several advantages, including the ability to transmit power with minimal losses, interconnect various sources of generation, and reduce transmission losses compared to conventional alternating current systems [21]. As a result, they enhance energy flow management within shipboard power systems and contribute to overall system stability. In fact, the concept of DC distribution on ships is gaining traction due to the following reasons:

- No need for phase angle synchronization of the generation units, simplifying connection and disconnection for energy generation and storage devices.
- Reduction in the size of power panels, onboard cables, and elimination of bulky low-frequency transformers.
- Decreased volume and weight through the use of high-speed rotating generators interfaced with the DC network through one or more rectifiers.

- Allows for reconfiguration after faults occur.
- Enables primary motors to operate at their optimal speeds, resulting in significant fuel savings.
- Facilitates interconnection with energy storage systems, reducing the number of conversion stages.

In recent years, a technical guideline, IEEE Stand 1709, has been developed [22]. It defines two main types of MVDC distribution: Radial and Zonal. The first is characterised by the obvious simplicity of the system and low implementation costs. Zonal distribution on the other hand has the advantage of maintaining a good continuity of service even if it is more complicated to design.

The MVDC distribution system can be simplified in the diagram [23] in Fig. 1.1. In general, the MVDC distribution system of a ship is made up of three subsystems,each dedicated to a specific operation: production (energy sources), distribution (network) and utilisation of electrical energy (loads).

The benefits that a DC medium-voltage distribution system can bring are obvious, but these distribution systems present many technical challenges [24], such as network stability, system protection and fault location. In fact, one of the most compelling technical challenges concerns the interruption of DC faults; DC short-circuit currents are generally limited by power converters and DC circuit breakers, but as yet there are no suitable and standardised MVDC protection devices on the market for the grid's operating DC voltages. Furthermore, as can be seen, in a medium-voltage DC power transmission system, the intensive use of power converters is required for the conversion of different DC/AC, AC/DC or DC/DC stages necessary to connect equipment to the MVDC bus. For this reason, power electronics plays a primary role in the realisation of DC distribution systems [25], and the research and development of new, increasingly reliable and efficient power convert-

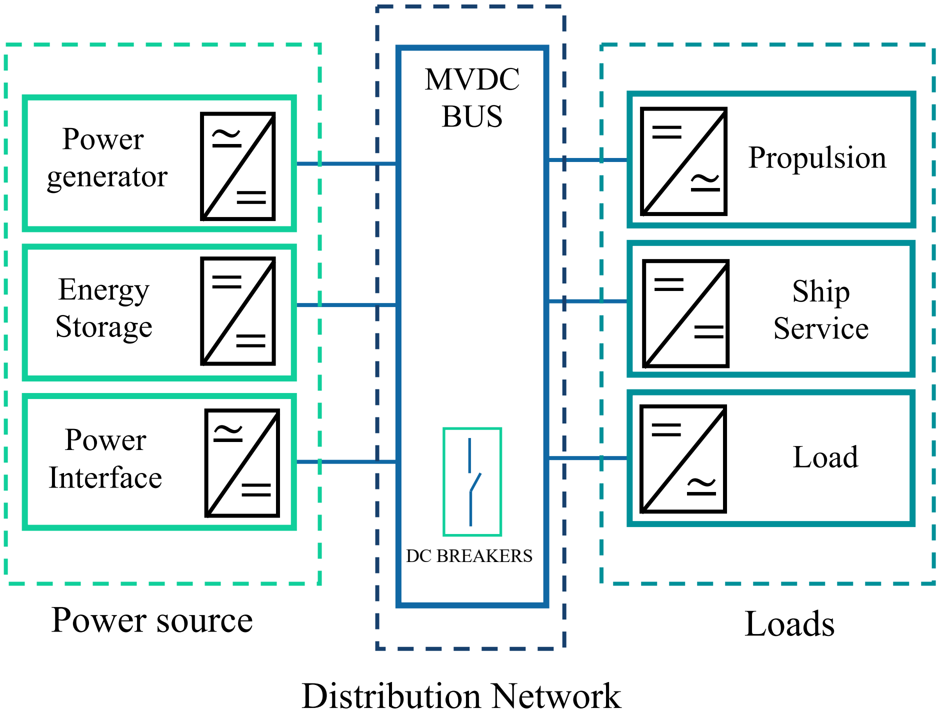

Figure 1.1: Generic layout of MVDC distribution system.

ers will be fundamental to the proper functioning of these new power transmission systems.

1.1.2 Role of Power Electronics

Renewable energy sources cannot be directly integrated into current distribution grids either because these grids are not designed to be able to meet the total demand for electricity or because there is a need for power electronic converters whose task is to manage the energy flows between RES and the distribution grid [25]. Power converters enable the conversion of electrical energy and the efficient interconnection of energy sources, storage systems and loads. The most common and widely used are conventional two-stage power converters, so called because the voltage at the output on the AC side of each phase is divided into two stages corresponding to the electrical potentials of the terminals on the DC side. These converters enable the conversion of electrical energy from DC to AC and are driven through pulse-width modulation (PWM) producing quasi-sinusoidal waveforms of the output voltage.

However, as the world's energy demand increases, power converters must handle higher powers and/or voltages, requiring advances in semiconductor technology or new converter topologies [26]. Indeed, the integration and utilisation of RES leads to an increasingly distributed energy network in the current and future electricity grid, involving multiple energy sources, energy storage and loads.

In this context to meet the growing needs for power conversion and integration of renewable energy sources into the power grid, multilevel converters are considered a promising solution compared to conventional two-level converters due to their ability to reach medium and high voltages with a mature technology of low-rated power devices and high-quality output waveforms [27–30].

Several multilevel converter topologies exist in the literature and on the market, including the neutral point converter (NPC), the cascaded H-bridge converter (CHB) and the flying capacitor converter (FC) [31, 32]. All these topologies have been commercialised in industrial applications, each of which possesses unique characteristics and is therefore suitable for different application scenarios [33].

The Modular Multilevel Converter (MMC), introduced in 2003 [34], has emerged as a highly suitable choice for HVDC - MVDC applications [35–38], attracting significant attention from both the academic community and the power electronics industry. The MMC is characterized by a series of independent power cells, commonly referred to as submodules (SMs), connected in cascade. This modular structure imparts the MMC with the following features and properties.

The MMC offers scalability in terms of voltage and power with minimal dv/dt stress. This allows for achieving very high voltages and powers by simply adding lower-power SMs connected in series. When a sufficient number of SMs is employed, the MMC ensures excellent and nearly perfect sinusoidal waveform quality for voltage and current at the terminals. This eliminates the need for bulky input/output filters to mitigate low-order harmonics, resulting in a compact design.

The modularity of the MMC imparts robustness against fault conditions and facilitates fault-tolerant operation, increasing system reliability. The modular structure and adopted standards simplify system manufacturing and maintenance.

1.2 Motivations and Goals of the Thesis

Isotta Fraschini Motori S.p.A is a Fincantieri company specializing in the design of disel engines and generator sets for marine applications. In recent years due to regulations introduced for the reduction of polluting gases and CO_2, Isotta Frsachini Motori S.p.A. has undertaken a project to develop modern marine propulsion systems in the near future by implementing hybrid architectures in which the potential of internal combustion engines and electric motors will be integrated. Innovative energy sources such as fuel cells and battery storage systems for efficient energy management will be used in the project. In this context Isotta Fraschini Motori funded my Ph.D. fellowship with the aim of developing the modular multilevel converter capable of integrating new renewable energy sources on board ship, minimising operating costs, consumption and greenhouse gas emission into the atmosphere.

Fig. 1.2 shows in synthesis the case study to be analysed in this thesis work, in which the central topic is the modular multilevel converter. The objective of this thesis work is to investigate and develop innovative control techniques for the Modular Multilevel Converter, addressing the latest technical challenges that this converter presents, such as circulating current reduction, output current control, and voltage balance techniques. After describing the converter topology structure, component sizing and MMC operation, an overview of the MMC control techniques already developed in the literature is given, followed by a description of the innovative techniques implemented in the experimental setup during the research activity.

The techniques proposed in this thesis work are based on injecting a signal proportional to the circulating current into one of the submodules of the MMC in order to develop an innovative circulating current reduction control. In addition, the same technique is explored for another control objective, namely, to balance capacitor voltages at the same time that the circulating current is reduced.

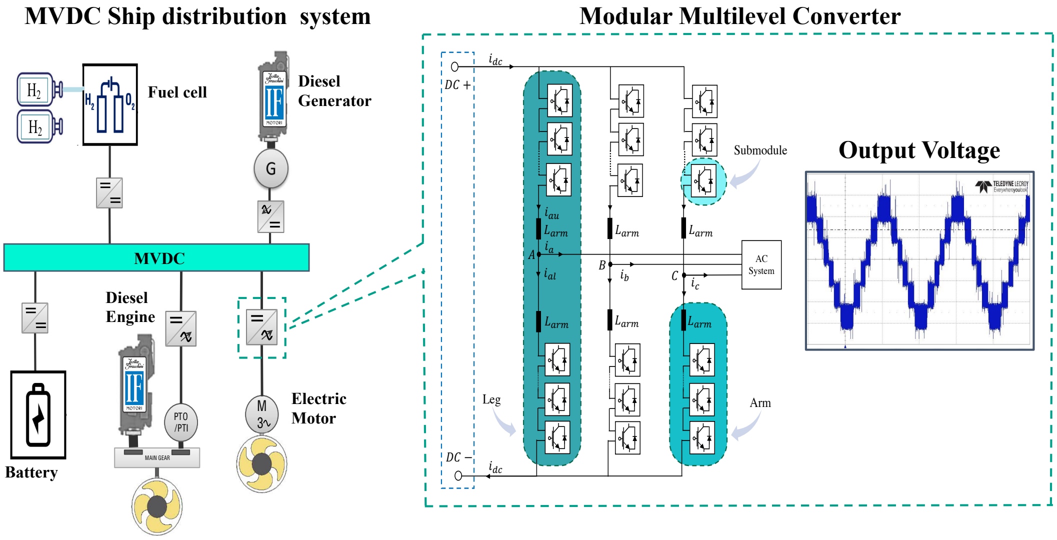

Figure 1.2: The motivation and goals of the thesis.

1.3 Structure of the Thesis

The thesis has been organized as follows.

- The second chapter is dedicated to a description of the main projects and activities I have developed at Isotta Fraschini Motori S.p.A. These research activities are aimed at short-term implementation with a high level of technological maturity and are of fundamental importance for the electrification of the company.
- The third chapter deals with the Modular Multilevel Converter. After a description of the topology and structure of this converter, its operation, its technical challenges, the most common modulation techniques and the mathematical model are shown.

- Conventional MMC control techniques are analysed in the fourth chapter, where a distinction is made between primary and secondary control techniques. The description start with the techniques of phase current control, capacitor voltage balancing strategies and circulating current control.

- The circulating current reduction technique proposed in this work is described in detail in Chapter 5. The chapter begins with an analysis of the steady-state model implemented for the definition of the circular iterations in the converter, then the control method implemented to reduce the circulating current based on the injection of a signal is shown.

- The experimental set-up of the Modular Multilevel Converter that is implemented during the PhD course, is described in Chapter 6. Then the results of the proposed control technique are reported. A comparison between the implemented and conventional technique is also shown, highlighting the main performance differences in terms of circulating current reduction and control complexity.

- An interesting extension of the proposed technique based on injections is presented in the Chapter 7, where, in addition to reducing the circulating current, it was used to pursue a second control target based on the balancing of capacitor voltages.

- Finally, the main conclusion are drawn in the final chapter.

1.4 List of Scientific Publications

1.4.1 Journals

1. D. D’Amato, R. Leuzzi, V. G. Monopoli *et al.*, Voltage Balance Strategy Based on a Single-Cell Injection Method in Modular Multilevel Converter. in *IEEE Transactions on Industrial Electronics.* (submitted).
2. D. D’Amato, R. Leuzzi, V. G. Monopoli *et al.*, Steady State Analysis Based on Circular Interaction in Modular Multilevel Converter. in *IEEE Transactions on Industrial Electronics.* (submitted).
3. D. D’Amato *et al.*, Circulating Current Control of MMC Based on Injection method. in *IEEE Transactions on Industry Applications.* (submitted).
4. D. D’Amato *et al.*, Design Procedure and Testing for the Electrification of a Maintenance Railway Vehicle. in *Energies 2023.* https://doi.org/10.3390/en16031205
5. D. D’Amato *et al.*, Impact of PWM Voltage Waveforms in High-Speed Drives: A Survey on High-Frequency Motor Models and Partial Discharge Phenomenon. in *Energies 2022.* https://doi.org/10.3390/en15041406

1.4.2 Conference Proceedings

1. D. D’Amato, R. Leuzzi, V. G. Monopoli, ”Single-Cell-Based Injection Method for Circulating Current Control in MMC” *2023 IEEE Energy Conversion Congress and Exposition (ECCE)*, 2023. (final paper) date of conference 28 October 2023.
2. G. Saponaro, D. D’Amato, M. Stefanizzi, E. Franchini, O. Osen, A. Hasan, S. M. Camporeale, V. G. Monopoli, ”Fuel-Cell Hybrid Power System Preliminary Design Optimization for Ferry Application” *2023 IEEE Energy Conver-*

sion Congress and Exposition (ECCE), 2023. (final paper) date of conference 28 October 2023.

3. G. Saponaro, M. Stefanizzi, D. D'Amato, E. Franchini, F. Fornarelli, M. Torresi, S. M. Camporeale, Modeling and design optimization of a hybrid power generator for full-electric naval propulsion, *Journal of Physics: Conference Series*,2022.

Chapter 2

Industrial company project

Isotta Fraschini Motori S.p.A is a Fincantieri company specializing in the design of diesel engines and generators for marine applications. In recent years due to regulations introduced to reduce polluting gases and CO_2, Isotta Fraschini Motori S.p.A. has undertaken a project to develop in the near future modern marine propulsion systems by implementing hybrid architectures in which the potential of internal combustion engines and electric motors will be integrated. This chapter has described the main projects and activities carried out during the three years of doctoral studies at the company.

2.1 Modeling and design optimization of a hybrid power generator for full-electric naval propulsion

A major advantage for a DC power transmission network over a conventional AC power transmission grid is that it is possible to develop new diesel generators with variable frequency so that the size can be reduced at the same power and the frequency can be adjustable according to the type of load. Therefore, one of the projects developed during the PhD program is to develop a mathematical model of a variable-speed diesel generator for optimizing fuel consumption and power transmission system efficiency.

There are average-value models (AVMs) of generators in the literature, but these have not been developed and designed to be able to simulate the behavior of the generator at different frequencies other than the design ones (50Hz or 60 Hz), so the purpose of this work is to provide the company Isotta Fraschini Motori S.p.A with an average model capable of simulating both the dynamic behavior of the genset at variable revolutions and its relative fuel consumption during the operating cycle. In addition, a procedure is developed to minimize the specific fuel consumption for a given load by making the variable-rpm generator work optimally. The idea for this project arose from being able to provide the company with a qualitative tool to test its engines for new networks in MVDC and to be able to start a new project toward smaller size and higher speed generators with higher efficiency. The generic layout of the system studied in this project is shown in Figure 2.1.

The following tasks were performed during the project:

- A set of bench tests is conducted using Isotta Fraschini Motori S.p.A.'s VL1716C2-MLL engine to acquire experimental data on engine behavior under various load and speed conditions.

- Based on the experimental data collected, an average-value model of variable-speed diesel engine is developed that takes into account the dynamic behavior of the engine and fuel consumption during the operating cycle.

- The model is validated in the basis of the acquired experimental data.

- Once the optimization procedure is completed, the improvement in specific fuel consumption compared with fixed-speed operation under different load conditions will be evaluated.

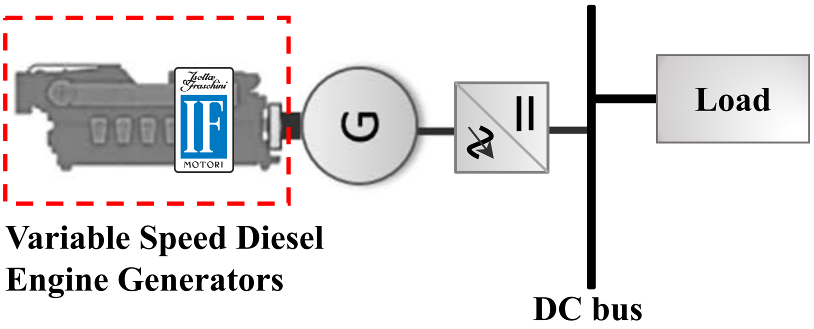

Figure 2.1: General scheme of variable speed diesel generator, electrical generator and power converter on board.

In Figure 2.2 shows the engine map, where it was possible to identify for each power required the correct speed in order to minimize the specific fuel consumption (SFOC).

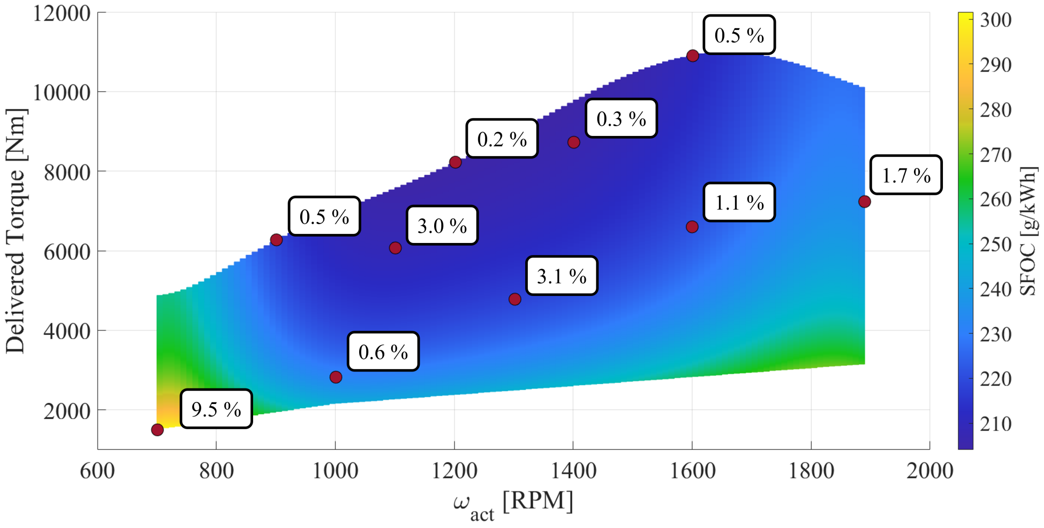

Figure 2.2: Engine delivered torque map with SFOC [g/kWh] by the proposed calculation, showing the relative error in percent for some of the experimental validation data.

2.1.1 Result

The simulation results were obtained by implementing the optimal speed, ω_{opt}, as reference speed for the model. This optimal speed was calculated in order to optimize the specific fuel consumption for each load connected to the system. Figure

2.3 illustrates the engine speed ω_{act}, follows the reference speed, ω_{opt}. Nevertheless, many factors, such as fuel quality, temperature, engine installation altitude and others, may cause the selected optimal speed to not perfectly match the load power and the minimum SFOC for a given power demand is not achieved.

The load profile required to the generator and the power delivered are shown in figure 2.4. In the first part, every five seconds the required power increases by 10% up to 90%, of the maximum deliverable power. After that, once the engine is brought to deliver the minimum power, it is required to take two more steps, one up to 20% and then up to 90% of the maximum power, respectively. Then the required power will be gradually reduced to 30%.

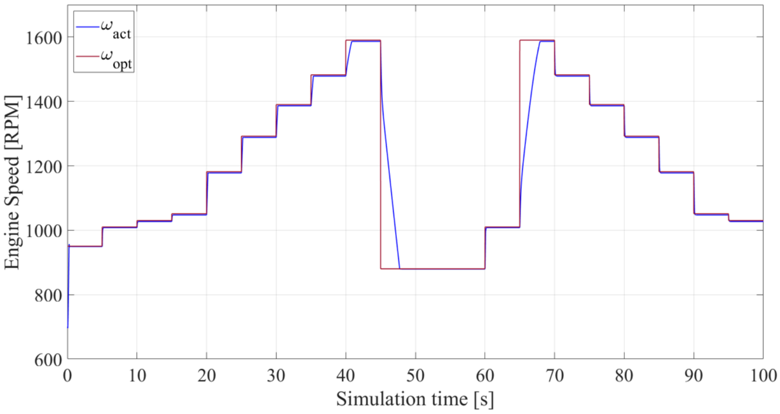

Figure 2.3: Resulting speed response of the engine, in blue, following the optimal speed reference, in red, to reach the applied load.

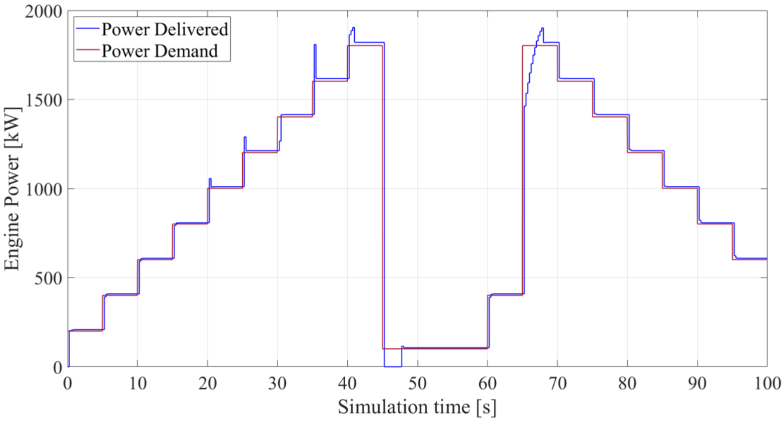

Figure 2.4: Power demanded at the generator, in red, and the engine response, in blue.

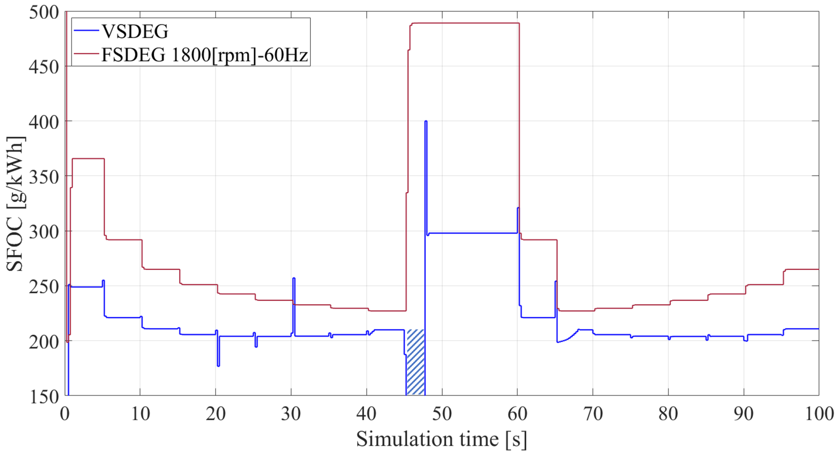

Figure 2.5: Simulation results in term of SFOC [g/kWh] for variable and fixed speed modes.

In Figure 2.5 are shown the results regarding the specific fuel consumption, calculated for the described duty cycle, for both the variable and fixed speed model. Working at variable speed, the engine follows the optimal speed reference ω_{opt}. Whereas, the chosen fixed speed was 1800 rpm to match the operating speed of a 4-pole electric machine working at 60 Hz. Table 2.1 shows the SFOC values at different loads for both VSDEG and FSDEG modes with the relative improvement in percentage. The considerable fuel savings at partial loads is a significant result since, for several naval applications, most of the operating time the power demand is less than 40% of the power installed.

Table 2.1: SFOC improvement according to the applied load for both variable (VSDEG) and fixed speed (FSDEG) modes.

Power Load $[\%]$	$[g/kWh]$ VSDEG (ω_{opt})	$[g/kWh]$ FSDEG	SFOC $[\%]$
10	249	366	32
20	221	292	24
30	211	265	20
40	206	251	18
50	204	243	16
60	204	237	14
70	204	233	12
80	206	230	10
90	210	227	8

2.2 Hybrid/Electric propulsion system

In response to climate change, governments around the world have committed to reducing greenhouse gas emissions, which contribute to global warming, through the energy transition from fossil fuels to renewable energy sources and the electrification of transportation. This company project outlines the design procedure for the electrification of a ship, and this approach can be applied to any other means of transportation. The methodology consists of the design of both an all-electric propulsion system and a storage system with the aim of zero emissions when the ship is operating. After highlighting the characteristics of the ship under consideration, a simulation model of the propulsion and generation system was developed to calculate the energy consumption of the entire ship system. The design procedure, summarised in Figure 2.6, was based on the implementation in MATLAB/Simulink of the mathematical model of the entire ship from which the technical solutions of the storage system and the propulsion system can be simulated. The proposed model was able to estimate the energy consumption of the entire storage system and the power that the propulsion system would have to provide to ensure the proper operation of the ship. Through the simulation results, it was possible to size the electric motor, converters, battery. This approach, based on mathematical modeling, has allowed the preliminary sizing of a propulsion system for various boats and the development of solutions for a hybrid propulsion system with electric and internal combustion motors developed by the company Isotta Fraschini Motori S.p.A. the generic layout is shown in Figure 2.7.

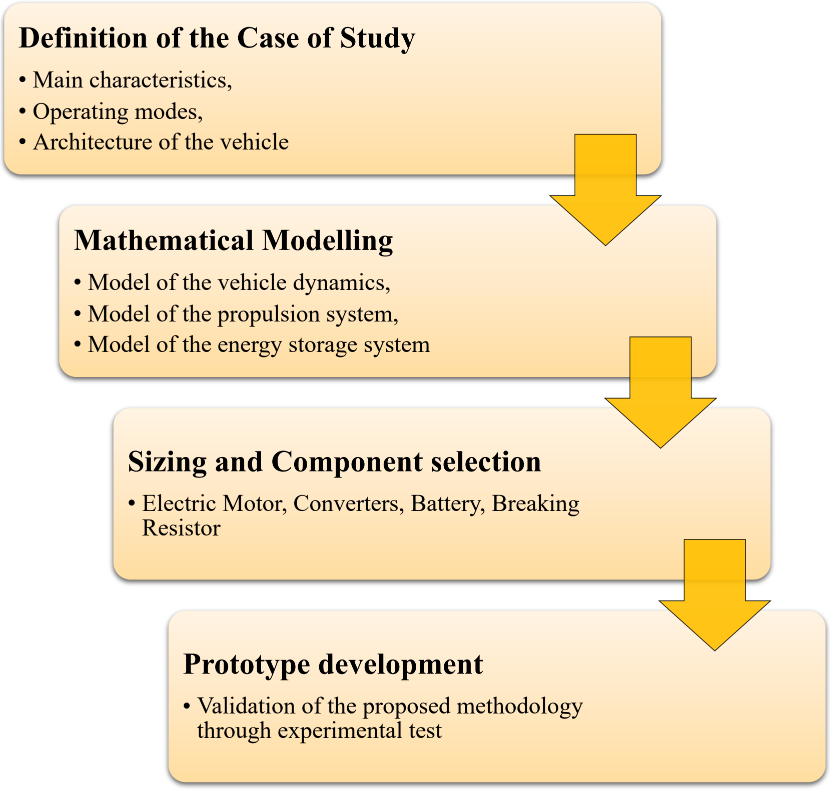

Figure 2.6: The mechanical characteristic and efficiency curves of the designed electric motor.

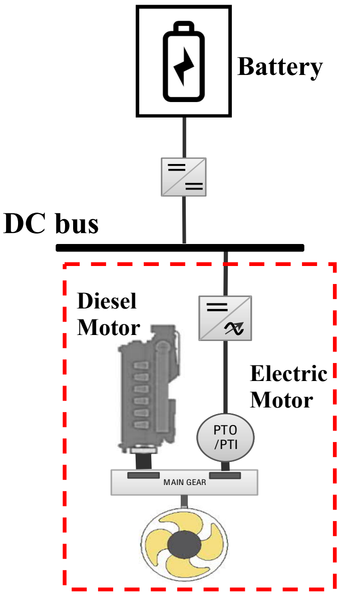

Figure 2.7: General scheme of hybrid propulsion system on board.

2.2.1 Mathematical Modelling

In this project work, the simulation aimed to model the dynamics of the ship/vehicle, the entire propulsion system, and the storage system to obtain an estimate of the energy consumption of the ship system required for the sizing of the entire power train. The proposed design procedure consisted of identifying the optimal technical solutions for the electric motor, inverter, and battery. The software used to develop the simulation models was MATLAB/Simulink because it allows the entire ship system to be implemented in a very simple and intuitive manner using a block diagram language. The dynamics of the various components were implemented through subsystems so that they could be easily modified and replaced. In addition, the implemented simulation provided acceptable results, and allowed even very long work cycles to be simulated in a few seconds.

The study of the electrical power required by the ship can be conducted by adopting different analysis methods; two different simulation approaches can be distinguished according to the ”direction” of the calculation method adopted: forward or backward. In a forward simulation approach, there is a control block that sends control actions such as acceleration or braking commands to the different components of the system to follow the desired speed of the vehicle. The driving model will then modify its command according to the proximity of the track. In contrast, in the backward method, the controller is not present and the analysis is made starting from the desired driving cycle of the vehicle, i.e., the time evolution of the vehicle speed. The value of the desired speed is transferred from the ship’s dynamic model to the transmission and the motor to analyse the performance of the components and derive the required power for the power system.

In this work, the model was based on the forward approach. Figure 2.8 shows the block diagram of the model. Indeed, an integral proportional speed control was implemented in order to reduce the difference between the actual speed of the ve-

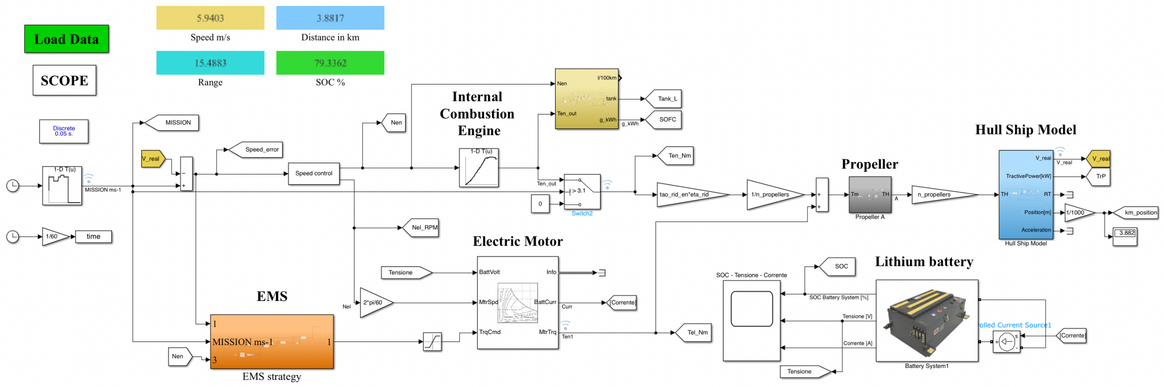

Figure 2.8: Block diagram of the implemented forward model.

hicle and the reference profile. From the output of the control block comes the command that influences the operation of the electric motor, which then receives the torque reference from the motor. In addition, isoefficiency curves were implemented for both the electric motor and the inverter to take into account the internal power losses that need to be considered when performing an energy analysis of the drive system.

Therefore, using the overall efficiency of the drive system at various values of torque and rotational speed, it is possible to derive the electrical power required to power the system from the mechanical power required at the axis. This electrical power will be drawn from the storage system. By varying the voltage at the ends of the accumulator system, it is possible to know the electric current required to power the system and provide the desired torque. The model of the storage system incorporates the value of the current to know the discharged capacity and estimate its state of charge.

a. Hull Ship Model

The ship model essentially represents the longitudinal dynamics such as the resistances to motion present when the ship moves with a given velocity profile, then the model of the ship's hull can be described through Newton's equation, as follows:

$$(m + m_a) \times \frac{dV}{dt} = T - R_t \tag{2.1}$$

where m is the mass of the ship, m_a is the mass of water that the ship moves during its operation, V is the speed of the ship, T is the thrust provided by the propeller, and R_t is instead the thrust required by the hull.

b. Electric Drive Model

To create the electric motor model, the mechanical characteristics of the motor, i.e., the angular torque–velocity curve, were taken into account. The study conducted was an energy analysis, and therefore, it was sufficient to assess the overall efficiency of the electric drive. To do this, the efficiencies of the inverter and motor were considered, which made it possible to determine the power absorbed and, consequently, the power supplied by the batteries. The electrical machine was subject to various types of losses during its operation, both losses in the conductors that make up the windings, typically copper, and losses in the iron and mechanical losses, due to friction and ventilation, which must be taken into due account. Through the calculation of internal motor losses, it is possible to trace the electrical power supplied to the input of the electric motor by knowing the mechanical power supplied to the shaft. The behavior of the electric motor can be effectively described using the mechanical characteristic and isoefficiency curves, as show in Figure 2.10. Even about the inverter, it is possible to model the losses that occur inside it more accurately, since the objective is to obtain the electrical power supplied by the storage system. The total losses of the inverter are therefore related to the conduction and switching losses in all the devices, both in the IGBTs or MOSFETs, and in the freewheeling diodes. In this work, these losses were taken into account through the inverter efficiency η_{Inv}, which is usually made available by the manufacturer. The efficiency of the inverter depends on the power supply concerning the rated power data of the inverter itself. The following Figure 2.9, purely indicative, represents the variation in efficiency with respect to the percentage of output power normalized with respect to the nominal power.

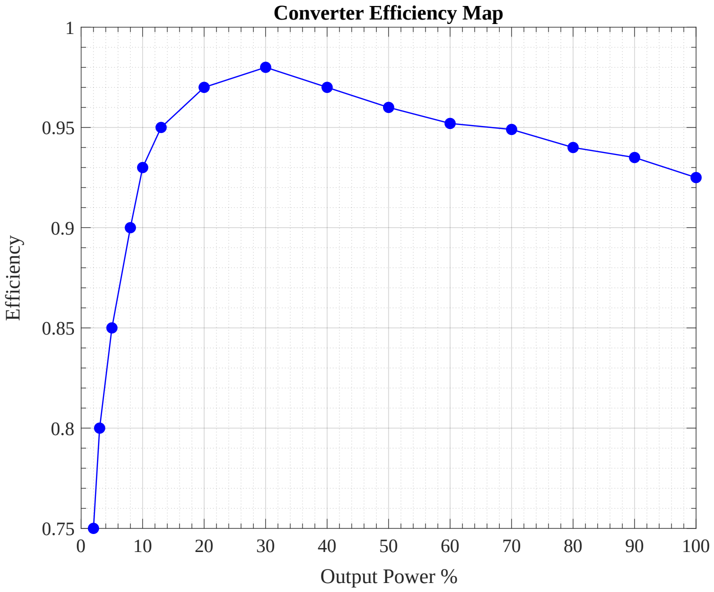

Figure 2.9: Converter efficiency map.

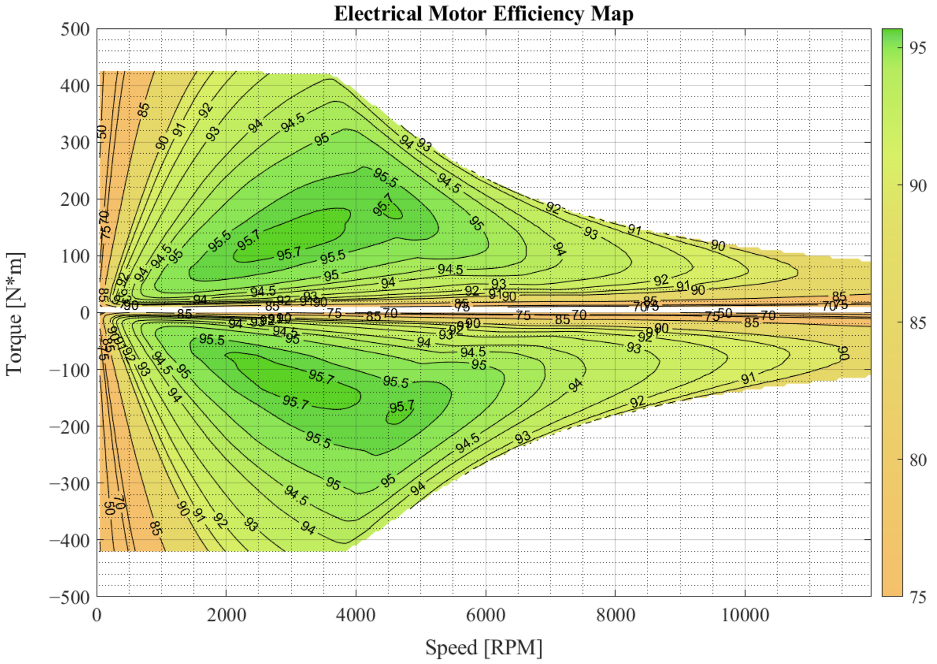

Figure 2.10: The mechanical characteristic and efficiency curves of the designed electric motor.

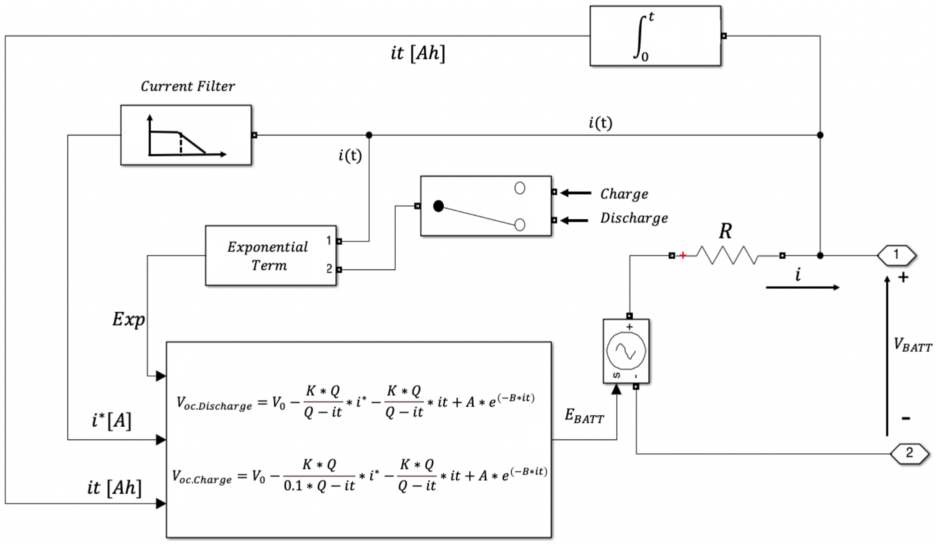

Figure 2.11: Schematic diagram of the battery model.

c. Battery Model

In the literature, there are mainly three categories of battery models, depending on the type of approach with which they are implemented and the kind of battery. These models are divided into electrochemical models, electrical circuit models, and mathematical models. However, the battery models proposed for sizing the storage system for all types of vehicle systems are based on mathematical models or equivalent circuit models. In this work, the battery model available in MATLAB/Simulink software for a lithium-ion battery was used. The circuit in this model consists of a controlled voltage generator, which allows the open-circuit voltage of the battery and its variation as a function of the state of charge (SOC) to be modeled, and a series resistor R, which allows internal voltage drops to be taken into account. In order to better represent the non-linear behavior of the open-circuit voltage, the polarisation parameter K was added. The battery current $i*$ was filtered through a low-pass filter to avoid the algebraic loop during the simulation. Fig. 2.11 shows the schematic of the proposed model. The proposed model was validated at a steady state through the experimental data of the dynamic performance provided by the battery manufacturer. Experimental tests were performed on the battery and compared with those obtained through the simulation to prove the validity of the model, as shown in Figure 2.12.

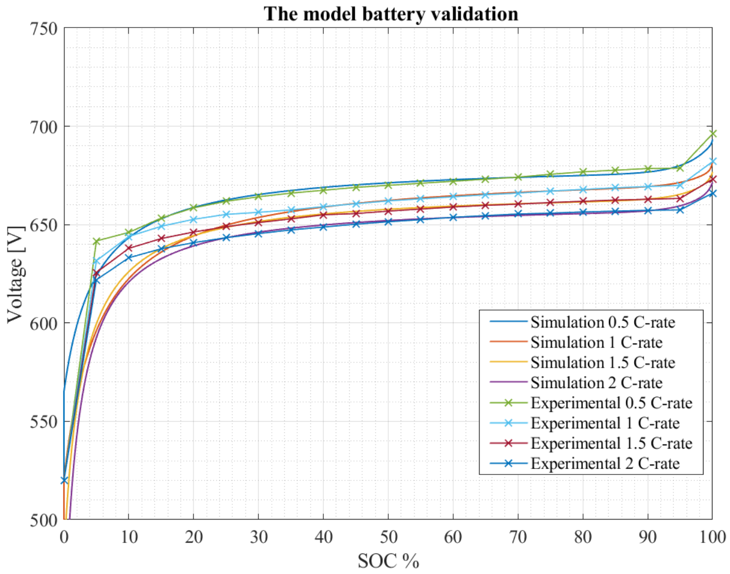

Figure 2.12: Comparison of the voltage-discharge curve values obtained from the model with the values carried out during the experimental tests on the battery.

2.2.2 Results

The model is validated following the performance specifications given by the company Isotta Fraschini Motori S.p.A. in order to develop a hybrid propulsion system for various vessels. Figure 2.13 shows the trend of the reference speeds and the speed simulated by the model. The second graph shows the trend in torques of the designed electric motor and the company's internal combustion engine. It can be seen that the electric motor is only used for speed transients and to reach steady state speed.

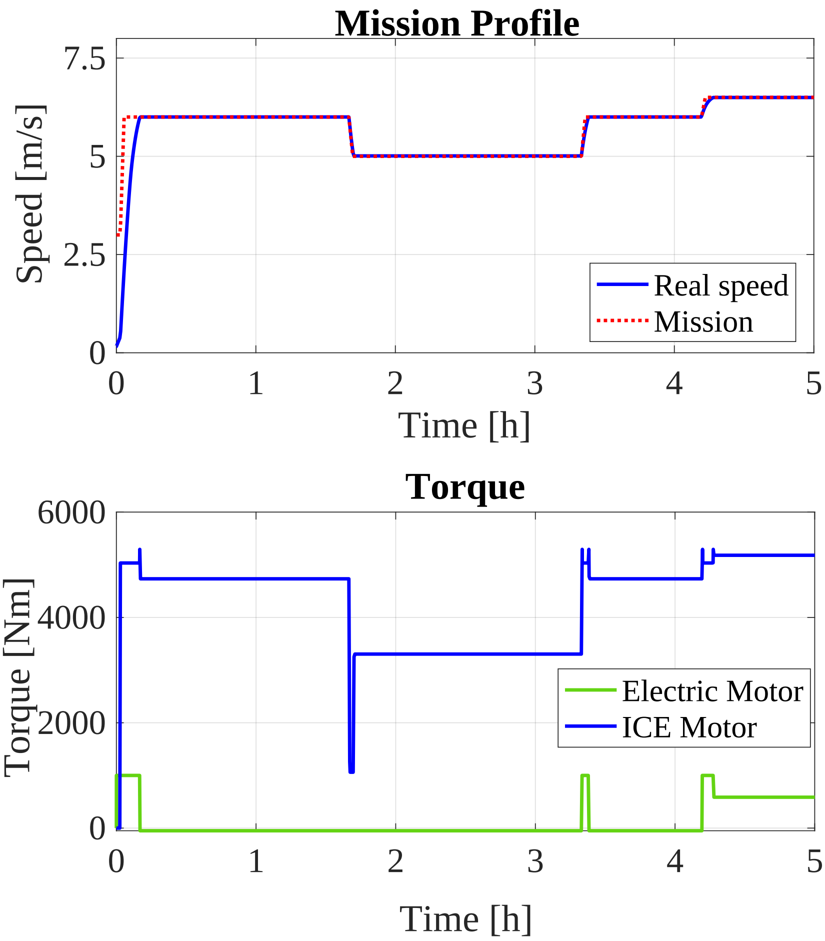

Figure 2.13: Ship speed and torques of the proposed hybrid propulsion system during a generic mission.

2.3 Hybrid Fuel-Cell/Battery Ferry Power System Retrofit Design

The use of hydrogen-based technologies for onboard power generation is having a significant impact on the shipping industry due to their potential to support decarbonization. In this context, Isotta Fraschini Motori S.p.A. wanted to develop the retrofit design of a diesel-battery power generation system for a ferry, using a fuel cell and battery layout. This project is carried out abroad at the Norwegian University of Science and Technology (NTNU) in Aalesund in cooperation with Vard Electro S.r.l a company in the Fincantieri S.p.A. group. The research aims to improve the efficiency of the power generation system by implementing a prescriptive digital twin. Simulations will take into account the power distribution among components, proposing an energy management strategy during the preliminary design phase. By sizing components to meet the energy demand of a real mission, this work aims to propose a solution that takes into account energy efficiency and operational costs. The results of this study are valuable for the future development of fuel cell technology for the maritime industry and provide an effective tool in sizing the power generation system on board all-electric propulsion vessels.

2.3.1 Fuel Cell in Marine Applications

The challenge of achieving zero pollution emissions in maritime transport cannot be met by relying solely on batteries to power ships. Batteries, due to their limited energy density, aren't suitable for medium and long distances, resulting in excessive weight, bulk, and time lost during recharging stops. A more efficient and cost-effective approach is to use a hybrid configuration, combining batteries with other power sources like fuel cells or internal combustion engines [39].

Proton Exchange Membrane Fuel Cells (PEMFCs), powered by hydrogen, have seen rapid development in recent decades, offering better power density and transient performance compared to other fuel cell types [13]. However, they have lower efficiency and face constraints related to fuel. In transport applications, PEMFCs are typically used in conjunction with batteries or supercapacitors to enhance overall efficiency and transient power handling capability [40]

The degradation of the PEMFC system is a current research topic, with scientific and especially economic implications. PEMFC residual life prediction method, validated via experiment, and economic lifetime is studied in [41]. In [42] the method of predicting the lifetime of PEMFCs using the current degradation law enhances the use of degradation information in current density. In the maritime transport sector, PEMFCs can be effectively utilized in ferries, either as alternatives to batteries or in combination with them [13, 39, 40]. The authors in [40] suggest a holistic design approach to designing coastal hybrid ships, focusing on optimizing a plug-in hybrid system that combines fuel cells and batteries. This optimization is based on two case studies and considers the degradation of power sources and the optimal management of energy from multiple sources. In [43], the research assesses the economic feasibility of a fuel cell-powered ferry in comparison to diesel and biodiesel, considering both current and future scenarios, and utilizing real-world operational data. Furthermore, in [44], the authors tackle the complex task of concurrently optimizing energy management and component sizing for emissions-free ferry vessels.

The primary aim of this company project is to create a predictive digital twin, which offers a comprehensive design for the fuel cell system. This is intended to maximize the performance and minimize stack degradation over the vessel's experimental missions. The PEMFC system illustrated in Figure 2.14, includes a simplified model of the fuel cell stack, the oxidizer humidification system, the hydrogen supply, the oxidizer supply line, and the efficiency of the DC/DC converter.

The proposed numerical model, developed within the Matlab/Simulink environment, adds complexity to the power system and introduces design optimization as discussed earlier. This holistic design study of the PEMFC takes into consideration its interaction with the fuel cell's auxiliary components, the battery's energy storage system, and the shore grid. It offers an energy management strategy for optimal operation. Finally, the initial design optimization employs a genetic algorithm provided by the GA Matlab function to determine the right number of fuel cell stacks, batteries, and the optimal time constant for managing the fuel cell to minimize stack degradation.

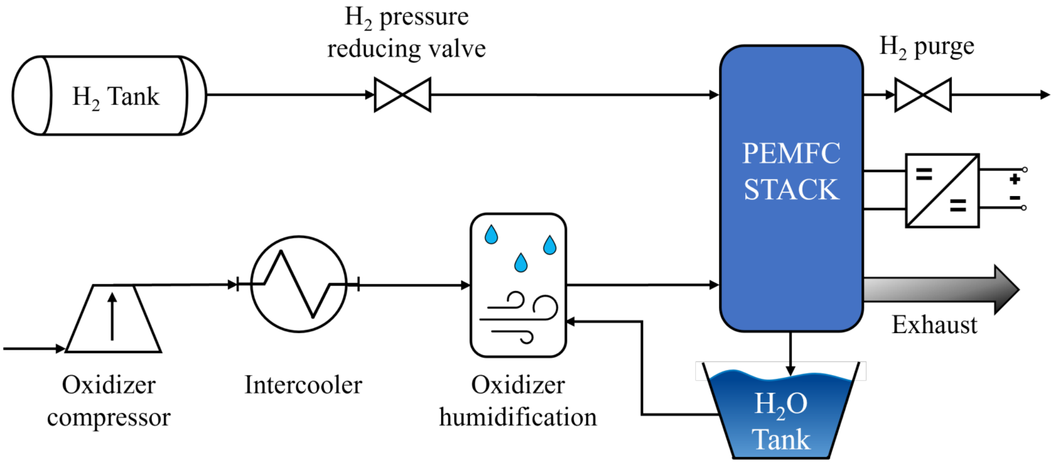

Figure 2.14: Caption

2.3.2 The Digital Model

The numerical model used in this work simulates the electrochemical and thermodynamic perspective of the PEMFC system [45] and it is tuned on the characteristic curves of the PEMFC Ballard FCvelocity™ HD6 (150 kW) and then validated through experimental results found in the technical literature [46]. The Figure 2.15 shows the results obtained by model calibration and validation through dynamic step experimental test (from 14kW to 140 kW).

The model provides also an evaluation of the power absorbed by the oxidizer compressor and auxiliaries. The thermal management strategy applied for the presented PEMFC system is based on the oxidizer stoichiometric excess ratio and the liquid water injected into the oxidizer. The latter is fundamental to ensure the cell membrane humidity. PEMFCs typically have a shorter operational lifetime due to various factors affecting the degradation rate. To achieve cost-effective performance, it is crucial to account for the degradation characteristics of PEMFCs during both the design and operational phases of a ship. Reasonable estimates of voltage degradation rates under different operating conditions can be derived by referencing the manufacturer's data sheet and existing literature.

In this study, a degradation estimation model is implemented. Estimating the

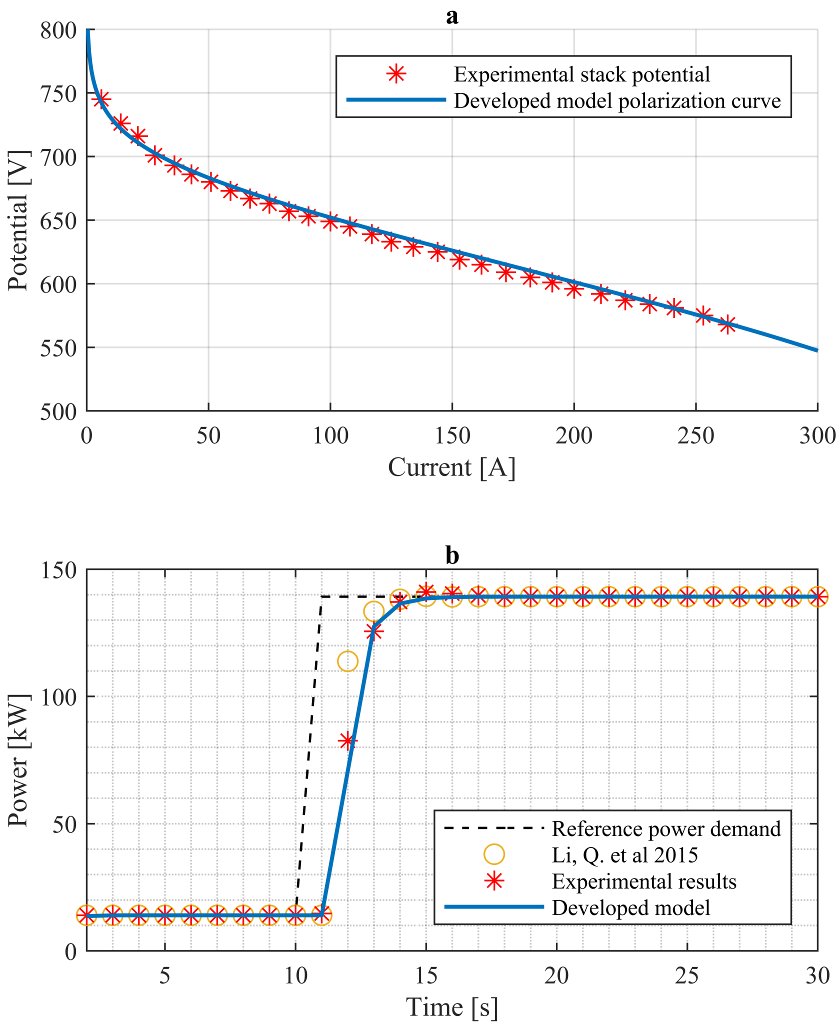

Figure 2.15: a) Results of fuel cell model calibration; b) Model validation through experimental data and technical literature [46].

degradation of individual fuel cells over a complete load cycle involves an equation that takes into account factors such as voltage degradation during low-power operation, high-power operation, power transients, and start/stop cycling. Table 2.2 provides information on the degradation rates of single PEMFC cells used in this research. It is important to note that these parameters can vary across different types of fuel cells, depending on their design and actual operating conditions.

Table 2.2: PEMFC Degradation Rates (Per Cell).

Operating Conditions	Deg. Rate
Low power ($0 - 80\%$ rated power)	$10.17[\mu V/h]$
High power ($> 80\%$ rated power)	11.74 $[\mu V/h]$
Transient loading	$4.41E - 2$ $[\mu V/\Delta kW]$
Start/stop	$23.91[\mu V/cycle]$

2.3.3 The Optimization Framework

According to [47], the concept of ”prescriptive digital twin” refers to an intelligent digital entity that enhances real-life objects by providing recommendations for corrective and preventive actions. Typically, these recommendations are derived from optimisation algorithms. The prescriptive digital twins exploit data acquired through monitoring and predictive twins as input in order to generate appropriate actions with a view to achieving favorable outcomes. Decisions regarding recommended actions are still made by humans, who trigger both remote and on-site execution of interventions. Figure 2.16 shows the model of the ”prescriptive digital twin” that is developed. The Physical Object represents the existing ferry, which is characterized by its actual power system and operational mission data, such as performance and efficiency. The Digital Asset simulates a new layout for the ferry’s power system, using PEMFC fuel cell technology and a battery, in order to meet the power requirements of the Physical Object. The optimization open variables include the number of PEMFC Ballard FCvelocity™ HD6 units N_{FC}, the number of battery packs N_b, and the low-pass filter time constant τ_{FC}. In this work, the capacity of a single battery pack is 124 kWh and the C-rate is up to 3 (C-max rate). The numerical model takes into account the efficiency of the storage related to the actual State of Charge (SOC), η_b, for a Li-ion battery [48] and the efficiency of the bi-directional DC/DC converter as function of the battery power output (charging/discharging), η_{bc}, taken from [40]. The overall power demand profile, P_d, is obtained by the sum of the hotel load L_H and the propulsion load L_P. The P_d^{filter} is the total power demand, limited to the maximum PEMFC net power $P_{FC,Net}^{max}$ passed through a low pass filter. The latter is characterized by a customized time constant τ_{FC} greater than or equal to the stack dynamic time constant. Higher τ_{FC} means lower cut-off frequency which makes the demand power signal smoother. Hence, the P_d^{filter} can be obtained as

$$P_d^{filter} = \begin{cases} \frac{P_d}{1+\tau_{FC}s} \text{ if } 0 \leq P_d \leq P_{FC,Net}^{max} \\ \frac{P_{FC,Net}^{max}}{1+\tau_{FC}s} \text{ if } P_d > P_{FC,Net}^{max} \end{cases} \tag{2.2}$$

The actual battery state of charge, SOC, and P_d^{filter} are calculated in the model and used as input for the Energy Management System (EMS). The EMS considers

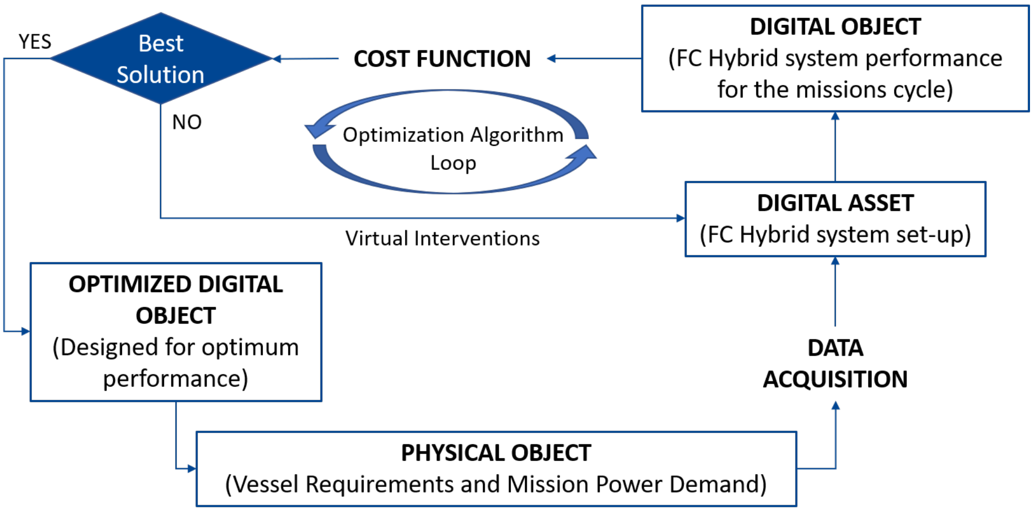

Figure 2.16: Prescriptive digital twin control framework.

the SOC of the battery, the power output for the PEMFC and its degradation, and the electrical energy taken from the harbor when the ship is docked.

The constraints implemented are shown in equation 2.3, where $P^{max}_{stack,Net}$ is the limit net power output of a stack of the PEMFC Ballard FCvelocity™ HD6, and P^{max}_{stack} is the maximum power of the single battery pack.

$$\begin{cases} N_{FC}, N_b \\ 3 \leq N_{FC} \leq 15 \\ 1 \leq N_b \leq 4 \\ 0.947 \leq \tau_{FC} \leq 50 \\ N_{FC} P^{max}_{stack,Net} + 0.8 N_b P^{max}_{stack} > P^{max}_{d} \\ N_{FC} P^{max}_{stack,Net} - N_b P^{max}_{stack} > 0 \end{cases} \tag{2.3}$$

The simulation results as power system configuration and performance determine the Digital Object. The Matlab GA optimization algorithm evaluates the best solution, referred to as the Optimized Digital Object. The output of the prescriptive digital twin provides recommendations for the size and preliminary design of the ferry's hybrid fuel system. The main objective function of this work is the reduction of PEM fuel cell degradation, a crucial aspect in all stages of design, from size analysis to operational cost assessment.

2.3.4 The Case Study

Figure 2.17 shows the general scheme of the ferry studied in this work. The vessel under investigation in this work is a ferry operating in Norway. Currently, the ship has a full-electric propulsion system, whereas two battery packs and two diesel generators, as backup, are connected to a DC switchboard as energy sources. The case study is characterized starting from the experimental data relatives to 8.5 h ferry's mission and the sample time of the data set is of 6 seconds, shown in Figure 2.18.

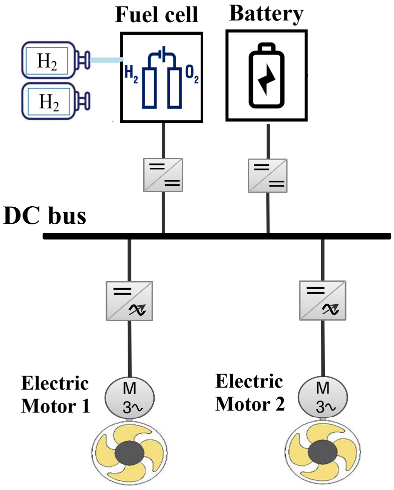

Figure 2.17: General scheme of hybrid Fuel-Cell/Battery for power generator on ferry.

The power demand profiles of the two propulsive electric motors and the ferry's hotel load are crucial for starting the analysis. The ferry's mission is interrupted for 2.5 hours after 3.5 hours of operation. During this stop, the fuel cell is switched off and only Cold Ironing mode is allowed. The presented model performs the simulation with a time step of one second. The detailed sampling rate of experimental data offers the opportunity to investigate the fuel cell system's dynamic performance and to study its coupling capabilities with energy storage such as batteries or supercapacitors. However, the objective of this work is to investigate the feasibility of the PEMFC system to power a long-haul ferry during its entire lifecycle considering the cell degradation rate. The expected average lifetime for a PEM fuel cell system for transport is around 5000 hours [40], so the effects of the degradation of the PEMFC system are studied through the model described above, by simulating a cycle of 600 missions, equivalent to 5100 working hours. At the beginning of each mission, the polarization curve is updated to take into account the potential lost during the operations. $P_{FC,Net}^{max}$ is updated according to the estimated degradation, in order to improve the robustness of the EMS strategy.

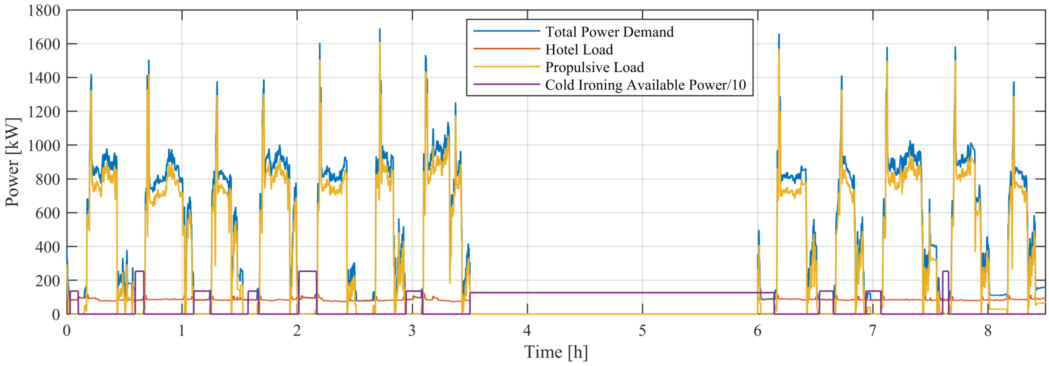

Figure 2.18: Mission hotel/propulsive load profiles and the shore power available.

2.3.5 Results

The optimization algorithm found the best energy source sizing and fuel cell time constant that minimize the stack degradation. The proposed solution consists of 8 PEMFC Ballard FCvelocity™ HD6 (150 kW), 3 Battery packs (124 kWh per pack), and set the low pass filter time constant τ_{FC} equal to the natural FC system time constant 0.947. A sensitivity analysis is performed on the effect of τ_{FC} on different feasible plant solutions. Indeed, the PEMFC system had to meet a significantly more stable load than a solution where most of the power is delivered by the fuel cell, and thus higher τ_{FC} values (20-50) can have a positive impact on reducing degradation. The first proposed results are related to the individual mission carried out over a 8.5-hour period, to provide a clear benchmark for assessing the effects of degradation on the system. Fig. 2.19 shows the power output of the hybrid system, where the negative values of battery power correspond to storage charging. Moreover, the energy that the EMS chooses to take from the shore grid. The battery ends the mission by storing energy, and the efficiency of the PEMFC system remains stable between 43.7% and 53.7%. The PEMFC degradation increases the energy storage exploitation, the reason why the time spent in default navigation mode and cold ironing mode significantly increases after the 400th mission. Finally, the degradation of the single PEMFC limit potential from the rated value of 730 V

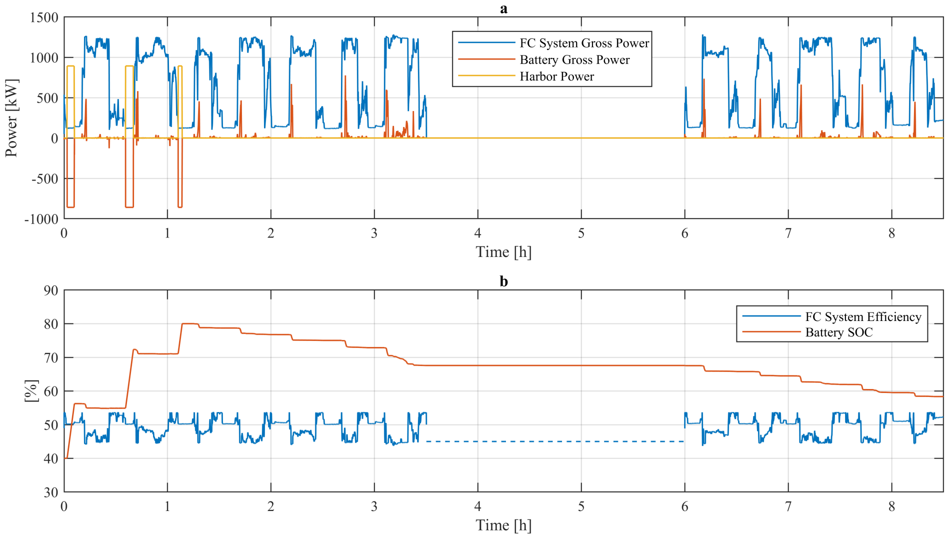

Figure 2.19: a) Mission power profiles of the FC system and battery gross power output and the amount of power taken from the harbor grid; b) Energy storage capacity and FC system efficiency along the first mission.

to 677 V. The total H_2 consumption for a single mission increases from 0.001918 kg to 0.002071 kg, as shown in Figure 2.20.

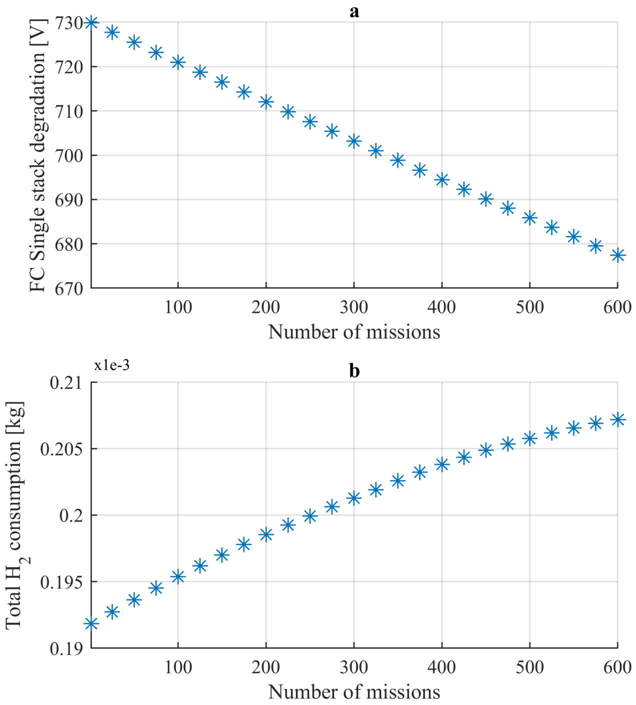

Figure 2.20: a) PEMFC Ballard FCvelocity™ HD6 limits potential degradation along the test cycle; b) Total hydrogen consumed in a single mission along the test cycle.

Finally, this work presents a prescriptive digital twin to provide a holistic design of the fuel cell system. The preliminary design optimization exploits the genetic algorithm provided by the GA Matlab function in order to find the correct number of FC stacks, batteries, and FC's management time constant value to achieve the minimum stack degradation. By sizing the components to meet the energy demand of a real mission, a feasible powertrain solution for the ferry under investigation is described. The evaluation of the fuel cell degradation, due the ferry's operations, studies 600 missions for a total of 5100 operating hours. During the test cycle, the software updates the cell polarization curve in the power system model and in the EMS, taking into account the potential lost. The results of this study could be valuable for the further implementation of fuel cell technology in the maritime industry and provide an effective tool in the sizing of the power generation system on board full electric propulsion vessels. The methodology presented in this document is relevant for the study of more complex power systems, which also take into account technologies such as internal combustion engines and different types of storage (e.g., flywheel energy storage). The minimized cost function, used in this project, is equal to the stack potential degradation, but in future work will be improved to provide more solid results in terms of operational cost and power system performance. In future work, it is planned to upgrade the proposed fuel cell model to achieve higher flexibility by simulating different types of fuel cells and auxiliary systems.

Chapter 3

Modular Multilevel Converter

The Modular Multilevel Converter (MMC) is considered as a promising candidate for many high- and medium-voltage applications due to its numerous features, including improved quality of the output waveforms, modularity, and scalability to different voltage and power levels, fault-tolerant operation, etc. [49, 50]. Today, the modular multilevel converter is widely used for electric drive applications and grid-connected especially for MVDC and HVDC applications. The MMC eliminates the requirement for an isolated DC source and the transformer for the high-voltage operation. Instead, it utilizes a cascade connection of SMs to reach the desired system voltage while producing a high-quality multilevel output voltage waveform.

This chapter first describes the structure of the Modular Multilevel Converter, considering its circuit diagram and the configurations of its submodules. It then describes the characteristics and operation of the converter from the most widely used modulation techniques found in the literature to the mathematical equations that govern the operation of the converter.

3.1 Structure and topology

The main success of the MMC can be attributed to its scalability and modularity characteristics because its structure consists of a series of building blocks also called submodules. The sub-module can be configured in various forms and consists of capacitors and semiconductor devices such as IGBT or SiC MOSFET these are used for particular applications [51, 52]. The number of sub-modules (SM) used in the MMC can vary greatly depending on several factors, including the specific application, the required operating voltage, and the power of the semiconductor devices. For electrical driver applications the required number of sub-modules can vary from 3 to a maximum of 10 sub-modules per arm [53–55].

In high-voltage direct current (HVDC) transmission systems with voltages of around 300 kV, the MMC is composed of more sub-modules, which can range from 100 to 400 sub-modules per arm [49, 56]. This configuration is necessary to efficiently handle the conversion and transmission of high-voltage energy [57, 58]. Static synchronous compensators (STACOM), used to regulate voltage in electrical networks, require a certain number of sub-modules, depending on the desired operating voltage. When an MMC is used in STACOM application it has to improve voltage stability and quality in the electrical infrastructure.

In general, the number of sub-modules used in the MMC is directly related to the power and voltage required by the specific application. The higher the voltage or power required, the greater the number of sub-modules needed to handle the energy conversion and control. This flexibility in sub-module configuration makes the MMC suitable for a wide range of energy and power electronics applications.

In terms of the SM topology, it is important to note that, in addition to the common half-bridge SM, the full-bridge (FB) SM configuration has become widespread. Indeed, the FB submodule allows both positive and negative voltage values to be generated at the output of the sub-module. This enables the MMC to operate in overmodulation and consequently make better use of the DC-link DC voltage, in other words, lower voltages on the capacitors with the same amplitude as the fundamental voltage harmonic produced at the output. This is a considerable advantage because lower DC voltages reduce switching losses and thus increase the efficiency of the converter. In addition, this configuration allows DC faults to be resolved and is therefore suitable for applications where greater reliability is required. However, it is essential to know that this advantage comes with the trade-off of requiring more IGBTs. Furthermore, researchers have explored hybrid MMC configurations that combine different submodule topologies [50, 55, 59].

In this thesis, the three-phase configuration is investigated here since it is adopted by most DC-AC applications. The generalized circuit configuration of a three-phase MMC is shown in Fig. 3.1, in which each submodule adopts the most commonly used half-bridge by commanding its complementary gate signals. In this way, the MMC can achieve high-quality voltage waveforms with $N+1$ level or $2N+1$ level phase voltage depending on the implemented modulation technique and the operational conditions of the application. The DC system of an MMC is often referred to as a DC-bus or DC-link, connected to the positive and negative bars of the converter legs. The three-phase AC system is connected to the mid-point of each leg (a, b, c). Each leg of the MMC is divided into two arms. The arms connected to the positive bar are referred to as the upper arms "u", and the arms connected to the negative bar are referred to as the lower arms "l". Each arm consists of N half-bridge submodules in series with the arm inductor L_{arm}. The arm inductor is connected in series with each group of submodules to limit the current due to the instantaneous voltage difference between the arms. In many circuit configurations of the MMC, the arm resistance R_{arm} connected in series with the arm inductance, which represents the parasitic arm resistance accounting for the converter arm losses, is also included. However, in this work, it has been omitted for the sake of simplification. The main features of MMC are as follows [28, 29]:

- It has a modular construction with the ability to scale the voltage and power rating.
- It can generate an output voltage and current waveforms with reduced dv/dt and ripple. Typically, an output voltage with a very low total harmonic distortion (THD) can be obtained.
- MMC can produce the output voltage waveform with a very large number of voltage levels. Hence, it is possible to operate the submodules with a very low switching frequency.
- It can employ redundant submodules in each arm to achieve a fault-tolerant operation.

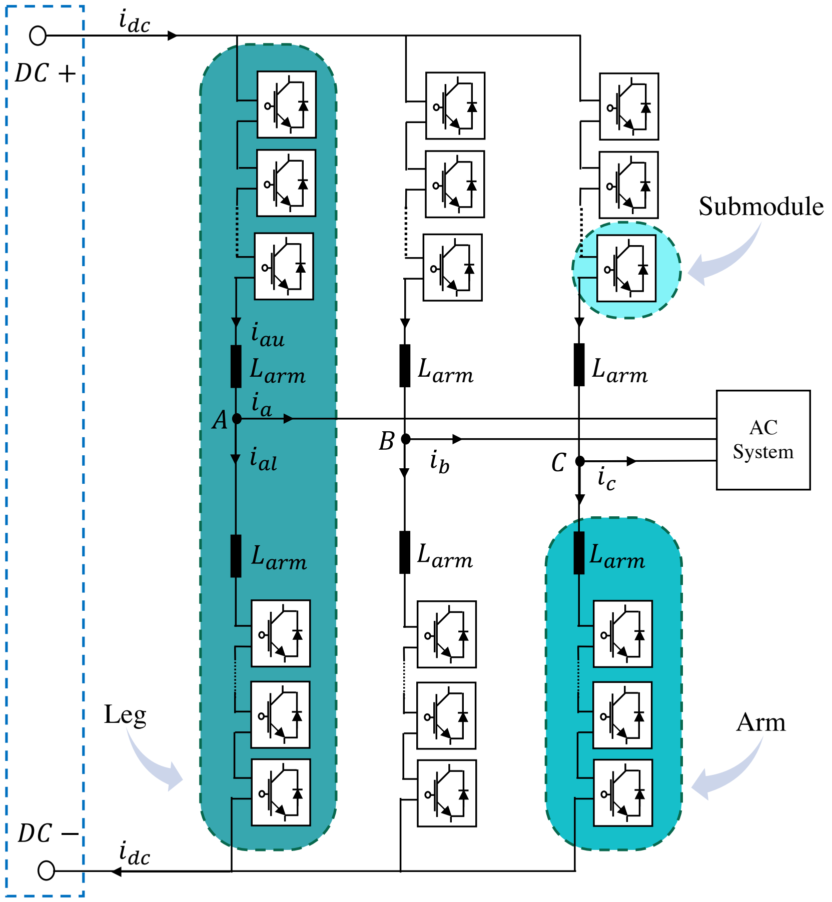

Figure 3.1: Configuration of modular multilevel converter.

3.1.1 Configuration of Submodules

As previously described, the submodule (SM) is a simple DC-AC power conversion circuit composed of low-voltage power semiconductor devices in the range of 600-1700 V and capacitors. The half-bridge (HB) can function as an AC-DC and DC-AC converter, as well as a DC-DC converter, depending on the control of its components. The power circuit remains structurally identical, but the difference lies in the use of a sinusoidal modulation signal instead of a constant one, and the different connection of the load. The circuit configuration of the half-bridge submodule is shown in Fig. 3.2. It consists of two IGBT devices with anti-parallel diodes Q_1 and Q_2 and a DC capacitor C. The two IGBT devices operate complementary to regulate the voltage across the DC capacitor to a value of v_c. The voltage across the DC capacitor is determined by the following equation:

$$v_c = \frac{1}{C}\int_0^t i_C dt \tag{3.1}$$

The DC current in terms of AC current and the switching state of top device S_1 is given by:

$$i_C = S_1 i_{xy} \tag{3.2}$$

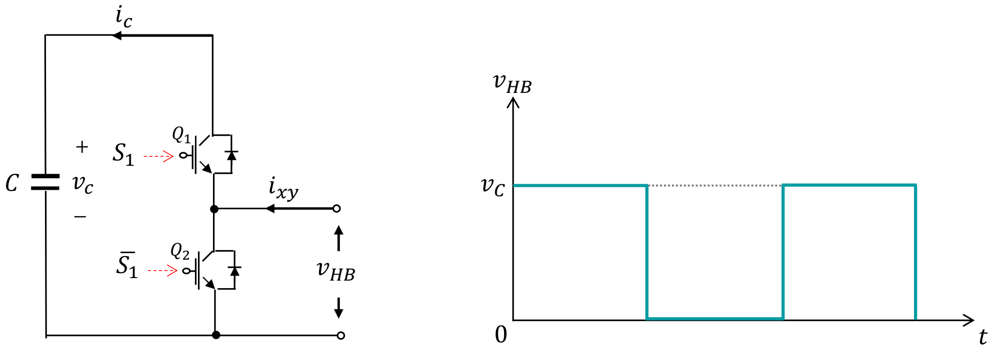

Figure 3.2: Half-bridge submodule and output voltage waveform.

Depending on the state switching S_1 of top device Q_1, the DC capacitor current is equal to either the AC current or zero. The possible states of S_1, and their effect on the DC capacitor voltage for different directions of AC current are shown in Tab. 3.1. The AC output voltage of the half-bridge submodule exhibits two voltage levels, 0 and v_C, as shown in Fig. 3.2. When the upper device, Q_1, conducts, the output voltage equals the voltage value of v_c. Conversely, when the upper device, Q_1, is turned off, the AC output voltage is 0. The AC output voltage of the half-bridge submodule can be represented in terms of the DC capacitor voltage and the switching state of the upper device, S_1, as follows:

$$v_{HB} = S_1 v_C \tag{3.3}$$

Among all the sub-modules, the half-bridge (HB) submodule stands out as the most prevalent and finds extensive application in commercial products. Its straightforward design, comprising just two semiconductor devices and a power capacitor, simplifies both control and design processes. In typical operation, only one of the devices, either Q_1 or Q_2, is turned on. Consequently, the half-bridge submodule exhibits minimal power losses and high efficiency. However, it's important to note that the output voltage of the half-bridge submodule comprises solely positive levels, making it unsuitable for bipolar operation and DC fault blocking.

The full-bridge (FB) submodule is comprised of four semiconductor devices and one DC capacitor, doubling the number of semiconductors compared to the half-bridge submodule at the same rated voltage. Nonetheless, the control and design complexity is on par with that of the half-bridge submodule. In the full-bridge

Table 3.1: Switching states of Half Bridge submodule.

State	S_1	v_{HB}	$i_{xy} > 0$	$i_{xy} \leq 0$
1	1	v_C	$v_C \Uparrow$	$v_C \Downarrow$
2	0	0	$v_C \approx$	$v_C \approx$

$\approx$ No change, $\Uparrow$ Charge, $\Downarrow$ Discharge submodule, two devices are active during standard operation, leading to increased power losses and reduced efficiency. However, the FB submodule offers fault tolerance advantages [37, 60]. In the event of a fault on the DC side, negative voltage levels within the full-bridge submodule are utilized to limit and control current. This fault-tolerant feature helps safeguard the overall system and ensures continued operation, even in the presence of DC-side faults.

3.1.2 Arm inductance project

The arm inductor L_{arm} and the submodule capacitor C are two fundamental components for the operation of the modular multilevel converter. Optimizing the size of the arm inductance and submodule capacitance is necessary for converter design. This paragraph describes the procedure for selecting the arm inductance, implemented for the experimental set-up in the laboratory. The arm inductance L_{arm} performs multiple functions necessary for the proper operation of the MMC:

- Provides power exchange between the converter and the distribution network to which it is connected.
- Reduces the circulating current but must be sized paying attention to the resonance phenomena of the circulating current (second and fourth harmonics).
- Useful to quench the fault current and its effects.

The sizing and choice of inductance should be considered to prevent resonance with the circulating current flowing in the phase of the MMC. Knowing that the equivalent capacitance C of the submodules is $500uF$, the value of the inductance was chosen considering this capacitance. The entire phase of the MMC can be represented altogether through the following equivalent circuit, that is, as an equivalent inductance and capacitance [61] as shown in Fig. 3.3.

The resonance angular frequency of this circuit is defined as:

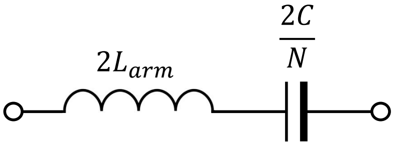

Figure 3.3: Equivalent circuit of the MMC phase.

$$\omega_{res} = \frac{1}{2}\sqrt{\frac{N}{L_{arm}C}} \tag{3.4}$$

where N is the number of submodules for each arm of the MMC. When sizing the arm inductance, an appropriate value should be chosen so that its resonance pulsation is far from the value of the second-order circulating current resonance angle frequency [61,62], and is equal to :

$$\omega_{cir} \simeq 2\omega_o \tag{3.5}$$

ω_o is the angular frequency at the fundamental frequency. Therefore, one must choose an arm inductor such that the relative resonant frequency is higher than $2\omega_o$ or lower. However, a good practice is to choose a low ω_{res} value around ω_o for both safety and economic reasons, as choosing a ω_{res} greater than $2\omega_o$ could then make the converter work with resonance values close to that of the fourth or sixth harmonic of the circulating current. For this set-up, the inductor chosen is $10mH$ as shown in Fig. 3.4.

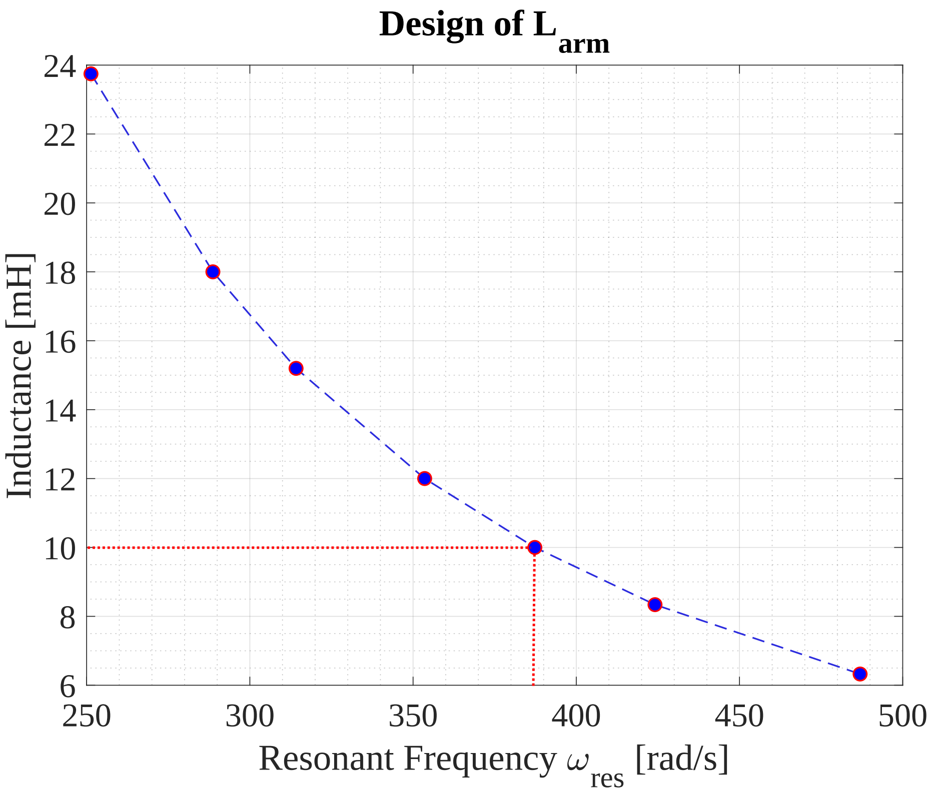

Figure 3.4: Choice of arm inductance.

3.2 Fundamental operation of the MMC

In this section, the operation of a modular multilevel converter using the popular half-bridge submodule is presented. The structure of a three-phase modular multilevel converter is shown in Fig. 3.5(a), considering DC/AC power conversion where the AC side of the MMC is connected through an RL filter to a grid system. The model is flexible because, in the case of off-grid connection, the AC system voltage v_{xg} is equal to zero and R, L denote the corresponding load parameters. As the name suggests, the Modular Multilevel Converter uses multiple identical submodules in each arm to generate the multilevel stepped waveform at the output. For easy understanding, only three half-bridge submodules per arm are considered, and their connection is shown in Fig. 3.5(b). Each submodule capacitor voltage is rated for v_c and its output terminals are connected in series to form an arm voltage.

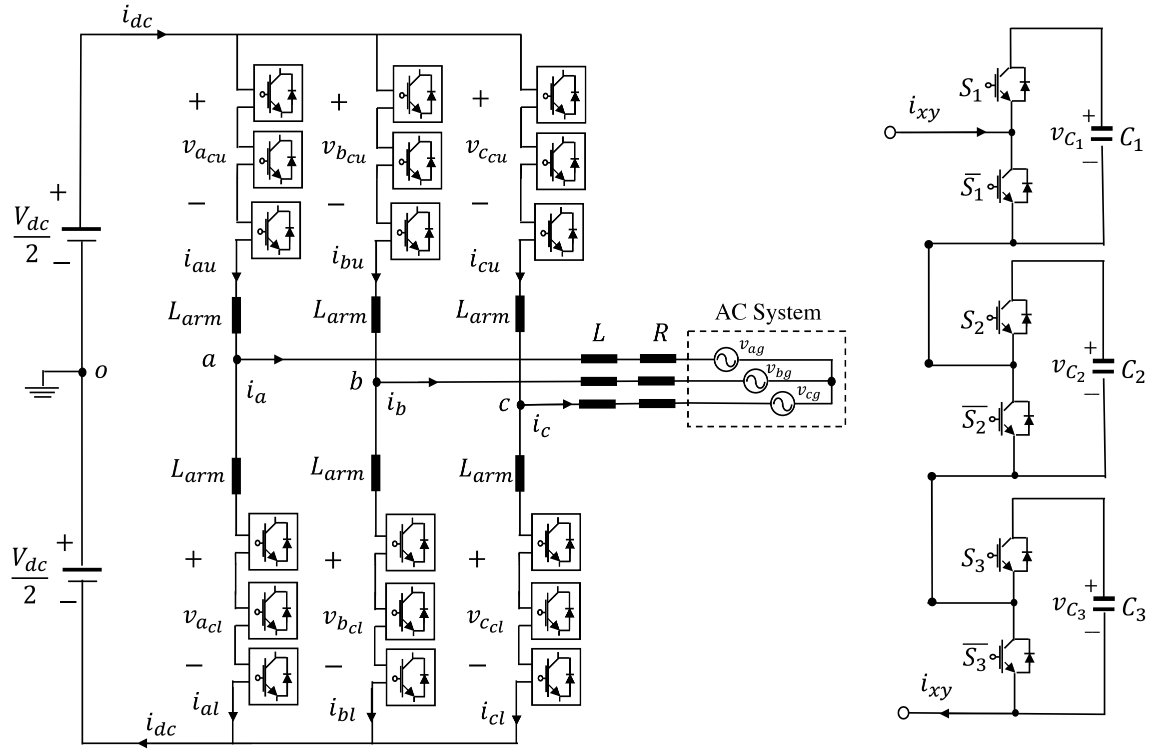

(a) (b)

Figure 3.5: Modular multilevel configuration: (a) MMC grid-connected, (b) connection diagram of HB submodule within the arm.

3.2.1 Mathematical Model

To explain the working principles of the MMC, the mathematical models of the MMC-based system need to be introduced first. Applying Kirchhoff's voltage Law (KVL) to an arbitrary phase-x shown in Fig. 3.6, the following equations can be respectively obtained for the voltage paths of the upper arm and lower arm as

$$v_{xu} = +\frac{V_{dc}}{2} - L_{arm}\frac{di_{xu}}{dt} - R_{arm}i_{xu} - v_{xg} - L\frac{di_x}{dt} - Ri_x \tag{3.6}$$

$$v_{xl} = +\frac{V_{dc}}{2} - L_{arm}\frac{di_{xl}}{dt} - R_{arm}i_{xl} + v_{xg} + L\frac{di_x}{dt} + Ri_x \tag{3.7}$$

The output and circulating currents can be expressed as a function of the upper- and lower-arm currents, namely i_{xu} and i_{xu} (with $x = a, b, c$).

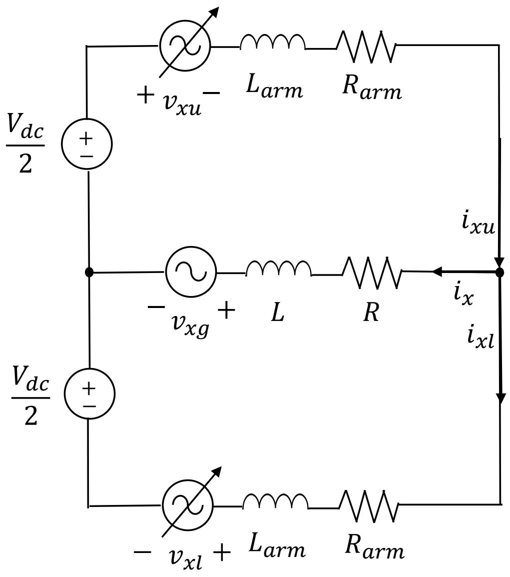

Figure 3.6: Per-phase equivalent circuit of MMC.

$$i_x = i_{xu} - i_{xl} \tag{3.8}$$

$$i_{xz} = \frac{i_{xu} + i_{xl}}{2} = i_{xz}^{DC} + i_{xz}^{AC} \tag{3.9}$$

The circulating current i_{xz} can be separated into two components. The dc part, i_{xz}^{DC}, is responsible for the active power flow through the converter and is equal to one-third of the dc-side current in a three-phase MMC during balanced operation. The ac component,i_{xz}^{AC}, on the other hand, is due to the interaction of the arm voltages and currents and does not contribute to the active power flow [15] and can be expressed in terms of its harmonic components, each with amplitude $I_{xz,n}$ and phase angle $\Phi_{xz,n}$, where n is the nth order harmonic, and ω is the angular frequency at the fundamental frequency (50 Hz) :

$$i_{xz}^{AC} = \sum_{n=1}^{\infty} I_{xz,n} \sin(n\omega t + \Phi_{xz,n}) \tag{3.10}$$

The mathematical models of the output current and circulating current can be respectively derived as

$$(L_{arm} + 2L)\frac{di_x}{dt} = (-R_{arm} - 2R)i_x - 2v_{xg} - v_{xu} + v_{xl} \tag{3.11}$$

$$L_{arm}\frac{di_{xz}}{dt} = -R_{arm}i_{xz} + \frac{V_{dc}}{2} - \frac{1}{2}(v_{xu} + v_{xl}) \tag{3.12}$$

Each arm voltage v_{xu} and v_{xl} are equivalent to a controllable voltage source, the value of which is given by the sum of all SM output voltages of that arm as

$$v_{xu} = \sum_{y=1}^{N} S_{xuy}v_{Cxuy} \tag{3.13}$$

$$v_{xl} = \sum_{y=1}^{N} S_{xly}v_{Cxly} \tag{3.14}$$

where the generic switching state S_x = 0 or 1 if the corresponding SM capacitor is bypassed or inserted into the arm voltage. Neglecting the difference between different SM capacitor voltages of the same arm (provided that an effective balancing method is used, this difference is relatively trivial compared to the reference of capacitor voltage, and thus this assumption can be made safely), 3.13 and 3.14 can be reformed to

$$v_{xu} \approx N_{xu}v_{Cxu} \tag{3.15}$$

$$v_{xl} \approx N_{xl}v_{Cxl} \tag{3.16}$$

where N_x denotes the number of switched-on SMs for each arm, or the so-called insertion index, of the corresponding arm as

$$N_x = \sum_{y=1}^{N} S_{xy} \tag{3.17}$$

v_{Cxu} and v_{Cxl} are defined as the average SM capacitor voltage of the corresponding arm as

$$v_{Cxu} = \frac{\sum_{y=1}^{N_{xu}} v_{Cxuy}}{N_{xu}} \tag{3.18}$$

$$v_{Cxl} = \frac{\sum_{y=1}^{N_{xl}} v_{Cxly}}{N_{xl}} \tag{3.19}$$

3.2.2 Modulation Techniques

The modulation techniques play a crucial role in controlling the Modular Multilevel Converter. In general, the modulation techniques are designed for different targets for example to improve the harmonic quality of the output waveforms when unequal power distribution between cells occur [63]. The modulation schemes are also designed to achieve other control objectives such as minimization of device switching frequency and reduction of power losses. The pulse width modulation (PWM) strategy is widely used for two-level power converters. It involves comparing modulation signals with a single triangular carrier signal to generate gating signals for two-level converters. This technique extends to multilevel converters, where multiple triangular carriers are compared with a phase modulation signal to generate gating signals for each submodule [64]. Multi-carrier modulation is categorized into phase-shifted (PSC-PWM) and level-shifted (LSC-PWM) carrier modulations based on carrier arrangement, these modulation schemes are widely applied to control the multilevel power converter due to their simple implementation and ease of extension to the higher number of voltage levels [65]. The phase-shifted modulation strategy requires a triangular carrier signal for every submodule. Therefore, if there are N submodules per arm, N carrier signals are generated to achieve the desired modulation. These N triangular carrier signals are arranged with a phase shift ϕ_c, as shown in Fig. 3.7. The phase shift ϕ_c between the carrier angles is determined by the following equation.

$$\phi_c = \frac{360}{N} \tag{3.20}$$

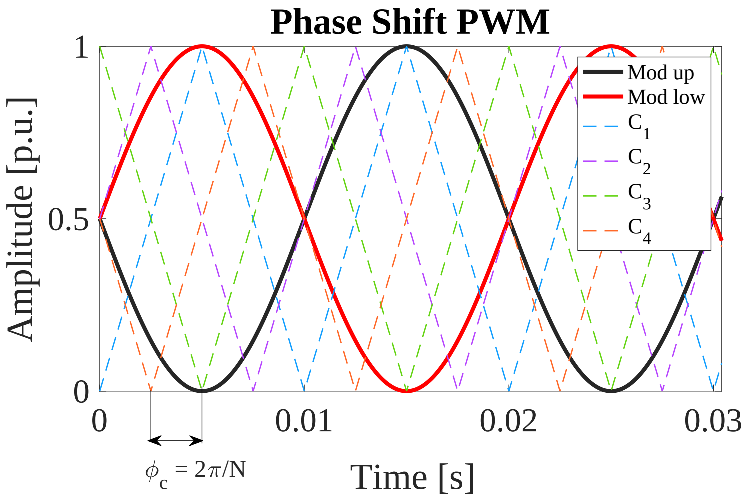

Figure 3.7: The Phase-Shift PWM strategy.

Additionally, an interleave angle ϕ_{ci} can be applied to the upper and lower arm triangular signals, as defined by:

$$\phi_{ci} = \frac{360}{2N} \tag{3.21}$$

When an interleave angle is introduced between the upper and lower arms, the modular multilevel converter generates an output voltage with 2N + 1 voltage levels, instead of N +1 levels when the interleave angle is set to 0.

In the level-shifted modulation, the triangular carrier signals with an identical peak-to-peak magnitude and frequency are vertically disposed within the linear modulation region. Depending on the phase relation between adjacent carriers, the LSC-PWM has three variations: phase-disposition (PD), phase-opposition-disposition (POD), and alternate phase-opposition-disposition (APOD). In PD-PWM modulation, the triangular carrier signals are vertically arranged in phase with each other as shown in Fig. 3.8. This modulation strategy is the most popular compared with other versions of level-shifted modulations because it generates an output voltage with a lower THD. The output waveform generated by a PS-PWM strategy using interleave angle and PD-PWM modulation are shown in Figures 3.9 and 3.10.

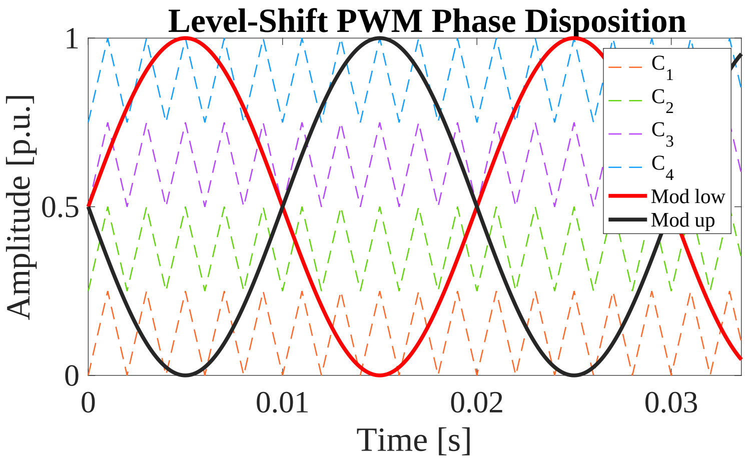

Figure 3.8: The Level-Shift PWM strategy.

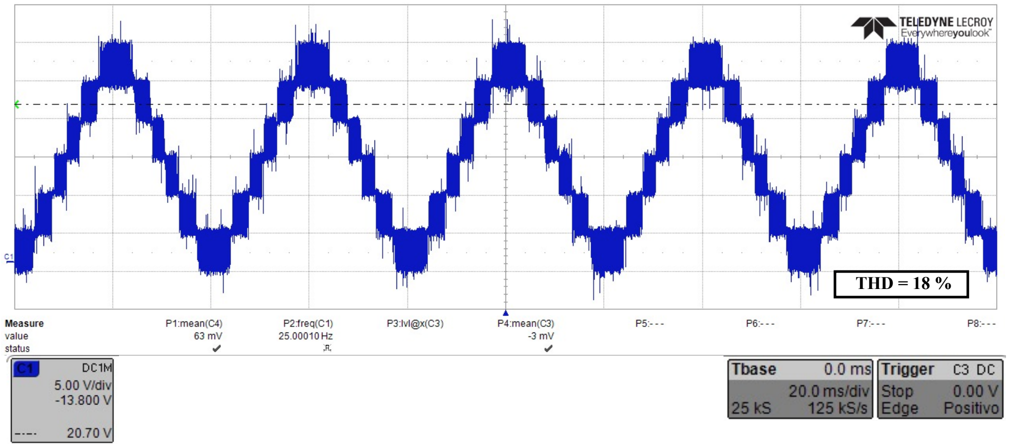

Measure	P1:mean(C4)	P2:freq(C1)	P3:lvl@x(C3)	P4:mean(C3)	P5:---	P6:---	P7:---	P8:---
value	63 mV	25.00010 Hz		-3 mV				
status	✓			✓				

C1 DC1M
5.00 V/div
-13.800 V
20.70 V

Tbase 0.0 ms
20.0 ms/div
25 kS 125 kS/s

Trigger C3 DC
Stop 0.00 V
Edge Positivo

Figure 3.9: The output voltage waveform generated by a Modular Multilevel Converter using the Phase-Shift modulation technique.

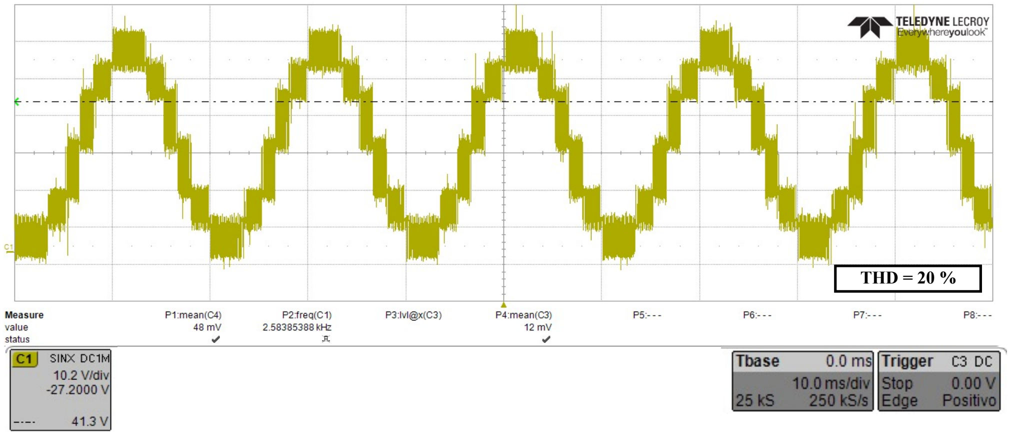

Measure	P1:mean(C4)	P2:freq(C1)	P3:lvl@x(C3)	P4:mean(C3)	P5:---	P6:---	P7:---	P8:---
value	48 mV	2.58385388 kHz		12 mV				
status	✓			✓				

C1 SINX DC1M
10.2 V/div
-27.2000 V
41.3 V

Tbase 0.0 ms
10.0 ms/div
25 kS 250 kS/s

Trigger C3 DC
Stop 0.00 V
Edge Positivo

Figure 3.10: The output voltage waveform generated by a Modular Multilevel Converter using the Level-Shift modulation technique

However, in high-power applications, the MMC typically consists of hundreds of SMs per arm, making it complex to implement one carrier for each SM. Additionally, carrier-based PWM schemes usually have a high switching frequency, resulting in elevated switching losses [66, 67]. Therefore, for HVDC transmission applications, when the number of SMs in the MMC is high, it is preferred to indirectly determine the gate signals through algorithms such as the Nearest Level Control (NLC). This modulation technique operates at a switching frequency equal to the fundamental frequency, resulting in higher distortion in the AC output voltage, especially when used for medium and low-voltage applications, due to its approximate nature derived from rounding functions. The Selective harmonic elimination (SHE) modulation offers high-quality output waveforms and precise control over output voltage harmonics while keeping device switching frequency at a minimum compared to multi-carrier modulation methods. However, implementing SHE involves offline calculations of switching angles and solving nonlinear equations, which becomes challenging with a large number of voltage levels in modular multilevel converters. Another existing modulation technique for Modular Multilevel Converters is space vector modulation (SVM), as reported in [68]. However, these methods become increasingly complex as the number of voltage levels in the MMC increases. All these techniques can be divided into categories based on several criteria, including switching frequency, implementation complexity, and applicability.

Table 3.2: Comperison of modulation strategies for MMC

Modulation	**Switching Frequency**	**Complexity**	**Applications**
Multi-Carrier Modulation	$f_{sw} > 1000$ Hz	Low	LV-MV
Space Vector Modulation (SVM)	100 Hz $< f_{sw} <$ 1000 Hz	Medium	LV-MV
Near-Level Modulation	100 Hz $< f_{sw} <$ 1000 Hz	Low	HVDC
Selective Harmonic Elimination (SHE)	fundamental	High	HVDC

3.2.3 Technical Challenges

The technical challenges associated with the operation and management of Modular Multilevel Converters are various and constitute an important research field for many scientists. These challenges include design constraints, sub-module capacitor voltage regulation, sub-module capacitor voltage ripple, circulating current management, and fault tolerance issues. [37, 60, 69, 70]

The Modular Multilevel Converter consists of several SMs for each arm, so a technical challenge is to develop a control system to regulate the capacitor voltages of the submodules. This control is crucial for generating a multilevel waveform output from the MMC. Another relevant aspect concerns the ripple of voltages in the submodule capacitors. This ripple results from the interaction between the currents and voltages within the converter and consists mainly of fundamental and second-order frequency components. Managing this ripple requires careful design and considerable capacitor capacitance, which can affect the overall cost of MMC systems. The size of the sub-module capacitor is determined by a balance between the size, cost, and voltage ripple of the capacitor, to provide an acceptable level of ripple at twice the fundamental frequency.

As described in the previous paragraphs, each phase of the MMC consists of two inductors and as many capacitors as there are submodules; these are the only passive components used in MMCs. The design of the arm inductance reduces the switching frequency harmonics in the arm current and limits the circulating current. Therefore, the sizing of the arm inductance depends on the harmonics of the arm current. The reduction of the circulating current must be taken into account when designing an arm inductor. The control of circulating currents is essential to ensure the functioning of the converter. These currents are generated by the voltage difference between the arms in each leg of the converter. They do not affect the AC output voltages and currents, but increase the peak and RMS value of the arm current, resulting in power losses and ripples in the capacitor voltage of the sub-modules.

Another major technical challenge concerns fault tolerance. MMCs are designed with redundant sub-modules to ensure that they can continue to operate in the event of a fault. Typically, during a fault, a bypass switch is used to disconnect a faulty sub-module and insert one of the redundant sub-modules into the arm. This process requires accurate fault detection and the insertion of redundant sub-modules without generating damaging pulse currents.

In order to protect the system during DC faults, DC circuit breakers are commonly used. However, these breakers are not standardized for different voltage levels. This has opened the way for the development of hybrid MMCs that include both Half-Bridge and Full-Bridge sub-modules with DC-fault blocking capabilities. These hybrid MMCs can be used effectively in MMC-HVDC systems [71,72]. Consequently, one of the most recent challenges concerns the efficient handling of short-circuit faults in the DC connection by means of advanced MMC control, especially in HVDC systems.

The DC-link short-circuit fault is another major issue in the MMC-based HVDC systems. The DC circuit breaker is commonly employed to protect the system during the DC faults. On the other hand, the submodules with DC fault-blocking capability can be employed in the MMC-HVDC system. During the fault condition, the submodules are controlled to generate the negative voltage level at the AC output terminal, which blocks the fault current flowing through the devices.

Chapter 4

Conventional Control Techniques

The modular multilevel converter presents more complex control than conventional two-level converters and involves in multiple control objectives. However, due to its structure with two arms per phase and a single dc port, the MMC operation presents some technical challenges, such as balancing the voltage of the submodule capacitors and suppressing the circulating currents, two phenomena that are closely linked [73]. Generally, the control techniques implemented for an MMC are classified into primary or secondary based on the control objective. The control techniques associated with the proper operation of the converter are defined as primary, while those that are dedicated to objectives such as reliability, efficiency, loss reduction, or size component optimization are defined as secondary. The MMC to operate properly needs therefore various controls for different objectives: the regulation of phase currents, SM capacitor voltages balancing and circulating currents. The conventional structure of the implemented control loops for an MMC is defined in Fig. 4.1, where an independent controller is implemented for each control target.

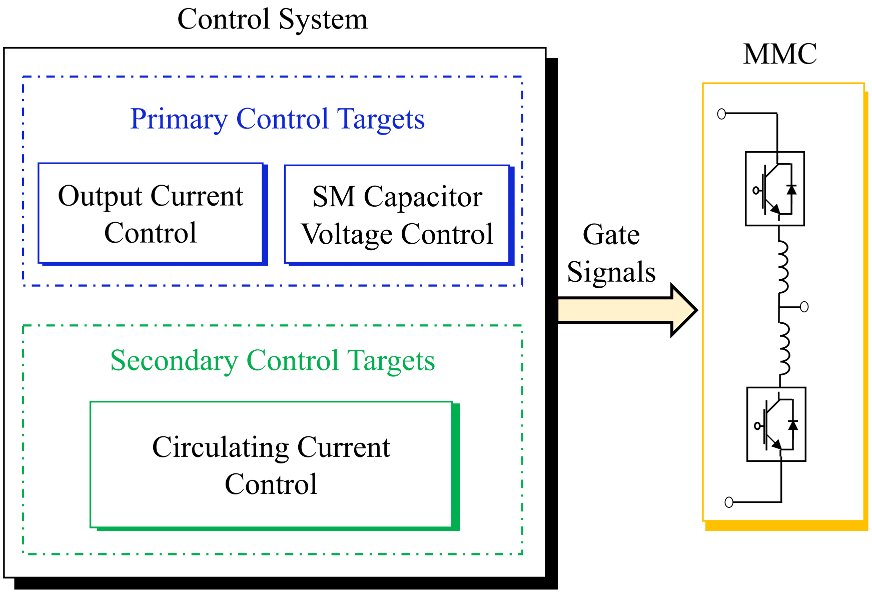

Figure 4.1: Block diagram of MMC control system.

4.1 Output Current Control

The phase current control loop is classified as a primary control objective and is essential to ensure the correct operation of the converter. This control loop provides the MMC operation during overload conditions by limiting the peak current. In addition, it improves the efficiency of the converter by accurately tracking the reference signal during transients and steady-state conditions in order to minimise the phase and amplitude error of the current. In the literature, the main control techniques can be divided into two macro groups: linear and non-linear techniques. Linear techniques are the most widespread and used in many industrial and research fields. These are based on the regulation of the PWM pulses generated by the modulation strategy and in turn can be divided into techniques based on Integral Proportional (PI) and Resonant Proportional (PR) controllers. The PI controllers are implemented using the synchronous coordinates d, q, while the PR controllers using the rotary coordinates α, β [74]. The linear techniques, although easier to implement, provide lower performance compared with nonlinear techniques, which are more appropriate for optimizing the performance of nonlinear systems, such as converters. These nonlinear techniques improve stability and dynamic response at different operating points. Nonlinear techniques are based on different control methods some of which are model predictive control, fuzzy logic, state feedback control and hysteresis controller. In general, the control techniques that already exist for two-level converters can be extended for multilevel converters. A controller for single-level phase of the MMC will be considered in this thesis, and therefore the synchronous reference frame will not be explored in this thesis. The controller implemented for phase current control is the PR controller.

4.1.1 Proportional Resonant Controller

Although PI controllers are the most widely used controllers in industry, these controllers are not suitable for controlling sinusoidal quantities especially for controlling a single-phase converter. These controllers can control sinusoidal quantities for a three-phase converter using Park's transforms in this way the three-phase current can be transformed into the d, q synchronous reference frame. In this case, the currents will appear as two constants in a balanced system, and therefore two PI controllers are required for the d-and q-component, respectively, to control the currents. In this thesis, the control of a single-phase MMC is analysed, and the choice of controller implementation turned to the PR controller so that the MMC could be controlled in both single-phase and three-phase configurations by passing in α, β coordinates.

In the literature, several solutions have been presented for the control of phase voltage and current through the resonant regulator [75,76], in which the ideal transfer function of the resonant regulator is extended to include both the crossover pulsation ω_c and the phase angle compensation δ. Thus, it is possible to define three different versions of the resonant regulator: Ideal, Real and Phase Compensation (Trigonometric).

a. Ideal PR Control

The ideal resonant controller is characterised by only one degree of freedom (1-DOF), and its tuning is based on the gain control "k_i". This type of controller ideally produces infinite gain at the project frequency, in our case for an output current control this frequency is equal to the fundamental pulsation "ω_o". This controller once implemented has a slow transient and a high sensitivity to noise even though its implementation is simple. The transfer function of this regulator is defined in 4.1. In Fig. 4.2 the Bode diagram of the PR ideal transfer function is show.

$$G_{r_{Ideal}}(s) = \frac{k_i s}{s^2 + \omega_o^2} \tag{4.1}$$

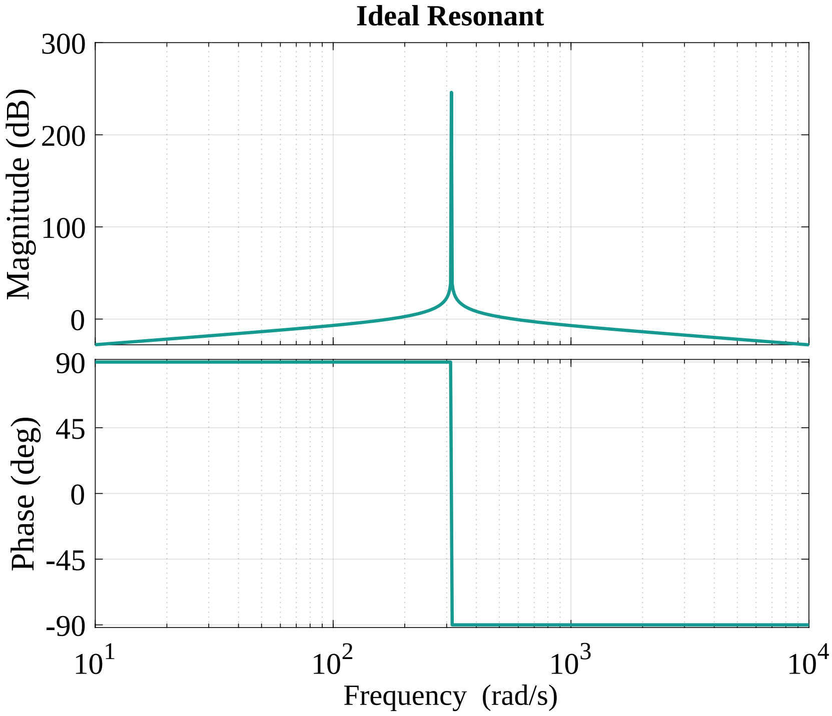

Figure 4.2: Bode diagram of Ideal PR Controller.

b. Real PR Control

In order to implement a digital PR controller, an additional parameter is generally introduced into the transfer function 4.1. This parameter is the crossing frequency "ω_c". The crossover pulsation is that pulsation for which the Bode plot of amplitudes crosses the horizontal axis (0 dB i.e. unit magnitude), providing important information on both the stability and dynamic performance of the system. The crossover frequency evaluated on the Bode diagrams of the open-loop system is related to the bandwidth (frequency at which the harmonic response modulus of the closed-loop system is 3 dB lower than the stationary value) and thus also represents a quantitative index of the system's speed. This parameter is designed to limit the infinite gain generated by the ideal resonant regulator. In this way the new transfer function will be characterised by a more attenuated and more selective frequency response, the controller will require less computing power to process the control law improving performance compared to the ideal regulator by reducing sensitivity to noise, but for some applications it may lead to a large tracking error. By adding this modification in 4.1, it is possible to obtain a true resonant controller shown in the following equation, in Fig. 4.3 the Bode diagram of the PR real transfer function is show.

$$G_{r_{Real}}(s) = 2k_i\omega_c \frac{s+\omega_c}{s^2+2\omega_c s+\omega_o^2} \tag{4.2}$$

c. Real PR Control with Phase Compensation (Trigonometric)

In recent years, the trigonomeric resonant regulator, also referred to as the phase-compensated regulator [76, 77], has become increasingly popular. This version of the resonant proportional regulator is born with the objective of providing three degrees of freedom (3-DOF) allowing the gain k_i, the pulsation ω_c and the angle δ to be adjusted separately. This version of PR, expressed in eq. 4.3, is often used for

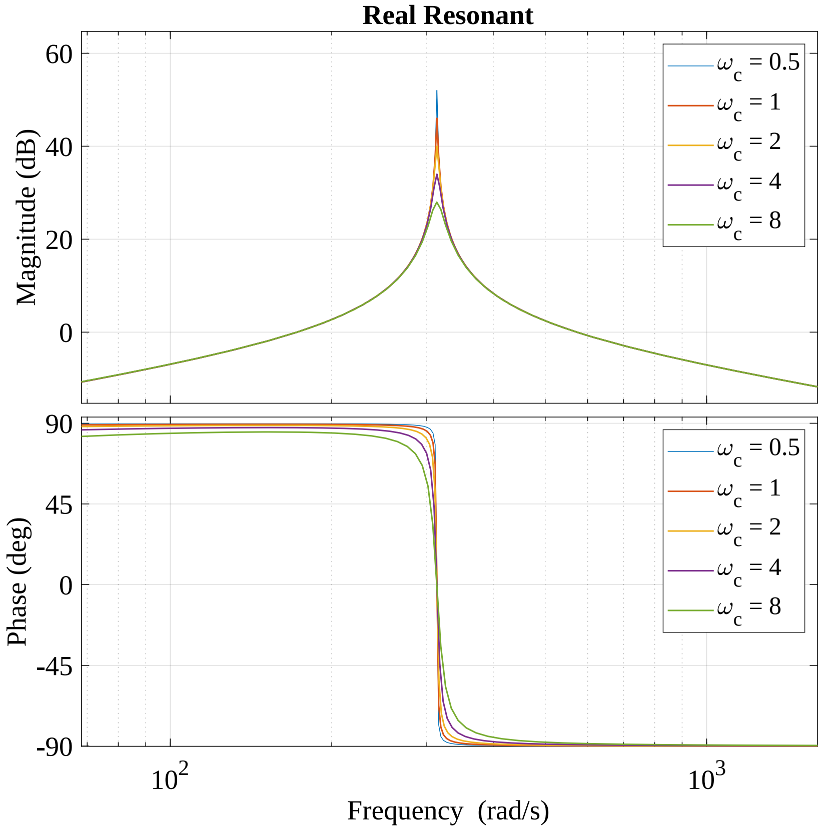

Figure 4.3: Bode diagram of Real PR Controller response by varying crossover frequency ω_c.

grid-connected applications, in the case of power supply distortion or loads that are particularly sensitive to voltage variations. In Fig. 4.4 the Bode diagram of the PR Trigonometric transfer function is show.

$$G_{r_{Trigoniometric}}(s) = 2k_i\omega_c \frac{s\cos\delta + \omega_c - \omega_o \sin\delta}{s^2 + 2\omega_c s + \omega_o^2} \tag{4.3}$$

4.1.2 Discrete PR Controller

In this thesis work, the output current control is implemented by means of a proportional resonant controller with phase compensation and by imposing the phase $\delta = 0$, it is possible to revert it to its real version with two degrees of freedom.

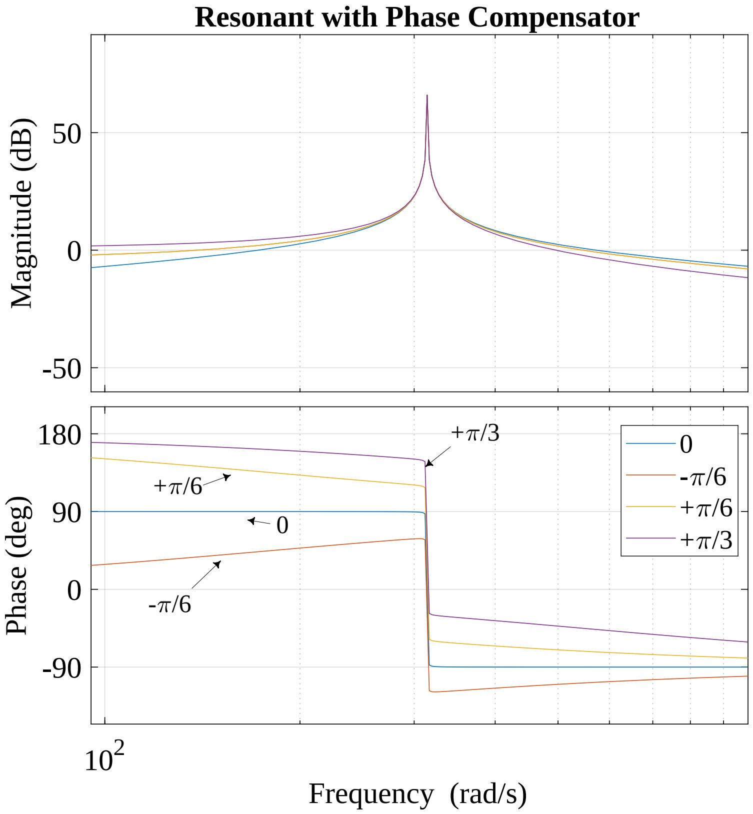

Figure 4.4: Bode diagram of PR Trigonometric Controller response by varying phase angle δ.

In order to be able to implement a controller on the microcontroller or FPGA, it is necessary to develop the transfer function 4.3 from continuous-time to discrete-time. There are several methods of discretization; in this thesis work, the Tustin discretization method [78] is used. When designing a discretized controller, it is assumed that the digital controller provides an analogue controller in continuous time that preserves the characteristics of the frequency response as much as possible, i.e. by not varying the crossing pulsation ω_c. The Tustin approximation transforms the real part of the continuous-time domain into discrete so that the continuous and discrete stability regions are mapped exactly into each other, but with the disadvantage that the continuous-time domain is compressed into the finite frequency range from 0 to 1 in discrete form. Consequently, the non-linear transformation causes the phase and frequency transformation to no longer correspond to the corresponding frequency in the continuous domain. Therefore, one can resort to the Tustin approximation with pre-warping around the desired resonance frequency.

In the following, the procedure for discretising the controller using the Bilinear Tustin approximation method pre-warping is provided.

$$s = \frac{2(z-1)}{T(z+1)} \tag{4.4}$$

where T denotes the sampling period of the implemented control system.

The pre-warping frequency is defined according to the resonant frequency ω_o, as follows:

$$\omega_{pw} = \frac{2}{T}\tan\left(\frac{\omega_o T}{2}\right) \tag{4.5}$$

Therefore, the modified Tustin transform with pre-wraping frequency becomes:

$$s = \frac{\omega_o}{\omega_{pw}}\frac{2(z-1)}{T(z+1)} = \frac{\omega_o}{\tan\left(\frac{\omega_o T}{2}\right)}\frac{(z-1)}{(z+1)} \tag{4.6}$$

Once you have defined the discrete method you want to use, you need to define the generic discrete-time transfer function as:

$$G_r(z) = \frac{k_1 + k_2 z^{-1} + k_3 z^{-2}}{1 + y_1 z^{-1} + y_2 z^{-2}} \tag{4.7}$$

The derivation of the parameters k_1, k_2, k_3, y_1, y_2 is essential to obtain the discrete controller and to understand the dynamics of the parameters.

The discretization of 4.3 is performed using the pre-warped Tustin approximation, as shown in 4.6. To ease of calculation, the parameter $k_T = \frac{\omega_o}{\tan\left(\frac{\omega_o T}{2}\right)}$ is defined, the discrete transfer function of the resonant proportional controller becomes:

$$G_r(z) = \frac{2k_i\omega_c(k_T\frac{(z-1)}{(z+1)}\cos\delta + \omega_c - \omega_o\sin\delta)}{(k_T\frac{(z-1)}{(z+1)})^2 + 2\omega_c(k_T\frac{(z-1)}{(z+1)}) + (\omega_o^2)} \tag{4.8}$$

The eq. 4.8 is simplified to performing the calculations first for the numerator $Num(z)$ and then for the denominator $Den(z)$

$$\begin{aligned} Num(z) =& z^2 \overbrace{\left(2k_i\omega_c k_T \cos\delta + 2k_i\omega_c^2 - 2k_i\omega_c\omega_o \sin\delta\right)}^{a_1} + \\ & z\overbrace{\left(4k_i\omega_c^2 - 4k_i\omega_c\omega_o \sin\delta\right)}^{a_2} + \\ & \overbrace{\left(+2k_i\omega_c^2 - 2k_i\omega_c\omega_o \sin\delta - 2k_i\omega_c k_T \cos\delta\right)}^{a_3} \end{aligned} \tag{4.9}$$

$$\begin{aligned} Den(z) =& z^2 \overbrace{\left(k_T^2 + 2\omega_c k_T + \omega_c^2 + \omega_o^2\right)}^{b_1} + \\ & z\overbrace{\left(+2\omega_c^2 - 2k_T^2 + 2\omega_o^2\right)}^{b_2} + \\ & \overbrace{\left(k_T^2 - 2\omega_c k_T + \omega_c^2 + \omega_o^2\right)}^{b_3} \end{aligned} \tag{4.10}$$

Now that the numerator and denominator expressions have been expressed, it is possible to calculate the parameters k_1, k_2, k_3, y_1, y_2 as

$$\begin{aligned} k_1 &= \frac{a_1}{b_1} \\ k_2 &= \frac{a_2}{b_1} \\ k_3 &= \frac{a_3}{b_1} \\ y_1 &= \frac{b_2}{b_1} \\ y_2 &= \frac{b_3}{b_1} \end{aligned} \tag{4.11}$$

The extended expressions of the five prameters of the controller are shown in the equation 4.12. The values shown in this section return the exact numerical values used for the non-ideal PR controller.

$$
\begin{aligned}
k_1 &= \frac{(2k_i\omega_c k_T\cos\delta + 2k_i\omega_c^2 - 2k_i\omega_c\omega_o\sin\delta)}{(k_T^2 - 2\omega_c k_T + \omega_c^2 + \omega_o^2)} \\
k_2 &= \frac{(4k_i\omega_c^2 - 4k_i\omega_c\omega_o\sin\delta)}{(k_T^2 - 2\omega_c k_T + \omega_c^2 + \omega_o^2)} \\
k_3 &= \frac{(+2k_i\omega_c^2 - 2k_i\omega_c\omega_o\sin\delta - 2k_i\omega_c k_T\cos\delta)}{(k_T^2 - 2\omega_c k_T + \omega_c^2 + \omega_o^2)} \qquad (4.12) \\
y_1 &= \frac{(+2\omega_c^2 - 2k_T^2 + 2\omega_o^2)}{(k_T^2 - 2\omega_c k_T + \omega_c^2 + \omega_o^2)} \\
y_2 &= \frac{(k_T^2 + 2\omega_c k_T + \omega_c^2 + \omega_o^2)}{(k_T^2 - 2\omega_c k_T + \omega_c^2 + \omega_o^2)}
\end{aligned}
$$

4.2 Voltage Balancing Strategy

The control of voltage balancing submodules of the MMC is of fundamental relevance to the operation of the entire converter. During the operation of the MMC, the capacitors of the SMs are constantly charged and discharged. This phenomenon in an MMC is closely linked to the direction of the arm current and the modulation technique used, which selects the sub-modules to be inserted or bypassed through the generation of the PWM drive signals to the semiconductor devices. However, in the absence of any balancing strategy, the capacitor voltage across some submodules accumulates a greater amount of charge than others, generating a progressive increase in voltage at their terminals. At the same time, other sub-modules will discharge and there will be a progressive reduction in their voltage. Mainly as a result of the different conduction times of each sub-module and the direction of the arm current. During the entire operation of the MMC, this phenomenon generates a progressive increase in the voltage of some SMs and a reduction in voltage for others, generating an overall unbalance in the voltages of the SMs. The unbalanced voltages affect the voltage ripple of the submodule capacitors and the harmonic distortion of the MMC's voltages and currents [79]. Therefore, voltage balance strategy techniques are implemented to maintain the submodule capacitors voltage at an identical value within the arm.

The voltage balancing can be realised either in the control phase through the implementation of a closed-loop controller, or in the modulation phase through the use of logic functions or sorting algorithm [80, 81]. The chosen balancing strategy involves the selection of a specific number of sub-modules from a total of N sub-modules within an arm, in order to achieve the desired voltage level. Consequently, this balancing strategy is often referred to as the sub-module selection method. Thereby, it operates by managing the currents flowing in the various capacitors of the sub-modules in order to reach the voltage balance, which is achieved by adjusting the timing and duration of insertion of each sub-module. However, these voltage-balancing techniques can have an undesired effect on the switching frequency [79, 82, 83]. This phenomenon will be discussed in more detail in Chapter 7. Voltage balancing techniques can be divided into two families: sensor-based and sensorless or few-sensor.

4.2.1 Voltage Balancing Sensor Techniques

The sorting-based algorithms are considered to be among the simplest and most effective for MMCs, as they balance the voltages between the sub-modules with good performance, minimising voltage variations between sub-modules. This way, all the voltages in the arm will be at the same value, resulting in equal to each other in every sampling period [79]. However, their operating principle based on the selection of the sub-modules to be inserted generates a large number of unnecessary switching [84], contributing to an increase in switching losses and transistor stress [85].

In [86], a modified sorting method is implemented with a reduced switching frequency, intending to make SM insertions only at the instants when a variation of the insertion index occurs, i.e. at the instants when the PWM modulation technique requires submodules to be inserted or deactivated. In this way, the switching frequency is reduced compared to the conventional sorting technique. However, implementing the sorting algorithm in the modulator requires a high computational load, especially when this technique is implemented for MMCs with a high number of SMs. For this reason, a balancing technique has been proposed in [80, 81] that performs the sorting of the submodule voltages through logical comparators, which certainly makes the compilation of the technique on the FPGA faster. These techniques described are applied within the modulator and have the advantage of very fast dynamics and excellent performance, however, they have the major disadvantage of changing the switching frequency, as shown in Fig. 4.5. In the figure, the performance of a conventional technique of balancing the upper arm voltages of the MMC implemented on the laboratory experimental setup is shown. In particular, the figure shows how the experimental upper arm voltages of the MMC, initially unbalanced are balanced once the technique proposed in [65] is applied. In [64] a voltage balancing technique is implemented outside the modulator through the use of a decentralized PI controller loop for each SM to control the discharge and charge dynamics of the capacitors separately. To achieve an equal power distribution for each SM, one of the possible disadvantages is that the number of sensors required for this technique is huge which makes it feasible for low power set-ups with a relatively low number of SMs.

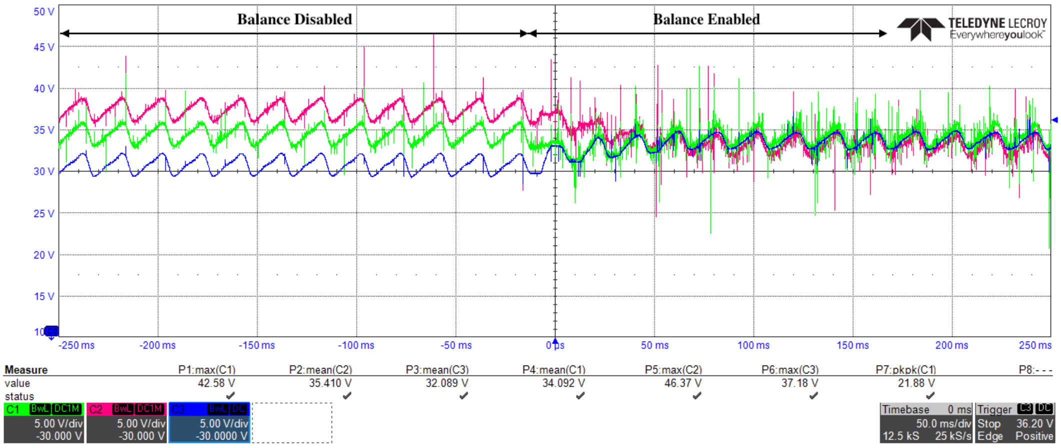

Measure	P1:max(C1)	P2:mean(C2)	P3:mean(C3)	P4:mean(C1)	P5:max(C2)	P6:max(C3)	P7:pkpk(C1)	P8:- - -
value	42.58 V	35.410 V	32.089 V	34.092 V	46.37 V	37.18 V	21.88 V	
status	✓	✓	✓	✓	✓	✓	✓	

Figure 4.5: The figure shows the capacitor voltage of SMs with and without the voltage balancing strategy activation.

4.2.2 Sensorless or Few-Sensor Techniques

A major disadvantage of conventional voltage balancing techniques is the high number of sensors required to measure the sub-module voltages. This contributes to an increase in cost and complexity of the control system. Therefore, in order to overcome this problem, strategies for estimating the voltages of the SMs have been developed that allow the voltage balancing to be realised by drastically reducing the number of sensors implemented. Sensorless techniques for voltage balancing are less popular than sensor-based techniques and are usually based on estimating capacitor voltages using information from electrical quantities that are easily accessible or already available to other control systems such as phase voltages and currents. A number of these techniques are associated with a conventional balancing technique, typically sorting [86], once the capacitor voltage estimation method has been applied.

The calculation of the energy stored in the two arms of the phase of the MMC is used in [87] to obtain the estimated instantaneous capacitor voltages of the SMs with a reduced number of sensors. The authors use only two sensors per phase, one to measure the phase current and the other to measure the voltage of the entire arm. Recently, the extended Kalman filter design is proposed in [88] to predict the voltages of the SMs. The extended kalman filter is a suitable state observer for the estimation of non-linear systems due to its characteristic of linearising the differntial queues [89]. The technique is based on the design of a discrete average model in which process and measurement noises are taken into account; the estimation is carried out by measuring the voltages and currents of the MMC arms. This method is particularly effective for estimating voltages and has the advantage that it can be used with any type of modulation strategy. However, it is very sensitive to the accuracy of the initial estimation and involves a considerable computational load.

4.3 Circulating Current Control

The circulating current originates from the instantaneous voltage difference between the arms of each leg of the MMC. This current mainly contains negative sequence components of even harmonic order, as seen in 2. Although the circulating current is part of the internal dynamics of the converter and has no effect on the output voltages and currents, it causes increased capacitor voltage ripple in the submodules and additional power losses in both power devices and arm inductances [49]. The circulating current control is defined as a secondary control designed to mitigate the AC part of the circulating current, i_{xz}^{AC}, to reduce losses and/or reduce voltage ripple in capacitors.

In recent years, several works have been carried out on the elimination of circulating currents in the MMC, which can be broadly categorized into direct and indirect methods according to the selected approach. As shown in Fig. 4.6.

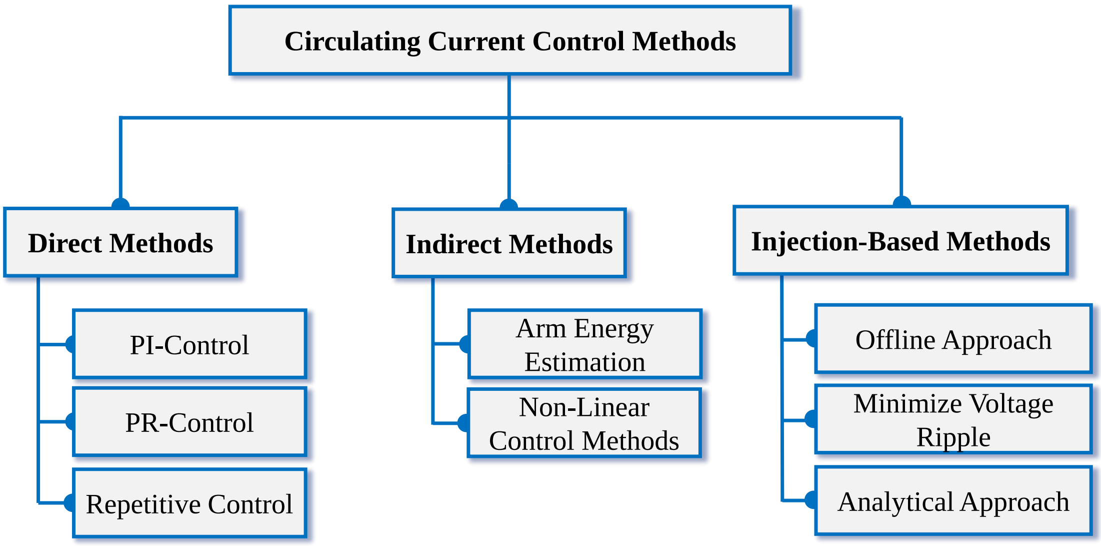

Figure 4.6: Classification of circulating current control techniques for an MMC

4.3.1 Direct Methods

Direct methods aim at reducing the circulating current through a dedicated feedback loop developed either in the $\alpha\beta$ stationary reference frame employing proportional-resonant (PR) regulators [90] or in the synchronous reference frame with proportional-integral (PI) controllers [86]. Several papers implement non-ideal proportional resonant controllers to reduce the circulating current that performs well for both unbalanced grid applications [91] and Modular Multilevel Converters under sub-module fault conditions [92]. A repetitive control (RC) algorithm has also been proposed in [93] to suppress the circulating current and its harmonic components. Although these control techniques have been proven to be very effective in reducing the circulating currents, they present the major drawback of only ensuring good tracking and disturbance rejection capabilities at the design frequency [94]. A dedicated controller is required for each harmonic component of the circulating current being compensated and an additional control loop must be included for capacitor voltage balancing purposes. Furthermore, the use of coordinate transformations increases control complexity, especially in the case of unbalanced operation [95]. Indeed, such rotating references are difficult to obtain for single-phase systems and require modifications for the unbalanced conditions of three-phase systems. In Fig. 4.7 is reported the block diagram of the non-ideal PR controller proposed in [91, 92].

The performance of the non-ideal PR control of circulating current for the MMC is shown in Fig.4.8; the circulating current is reduced when the PR control is active, however, a second harmonic component is still present and generates a power imbalance between the arms of the MMC as noted of the shape from the arm currents. All the PR circulating current controller parameters are summarized in the following table 4.1:

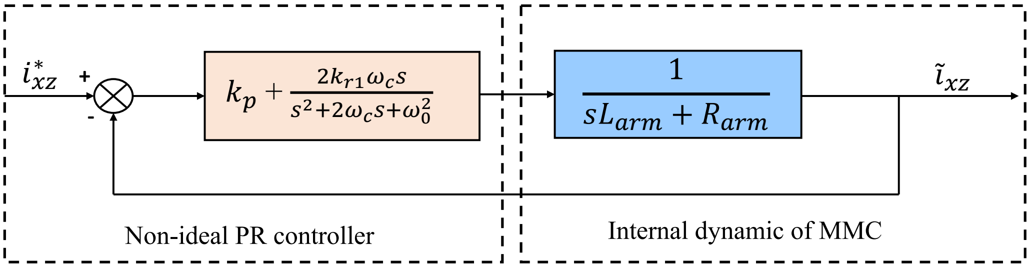

Figure 4.7: The block diagrams of the convetional non-ideal PR controller.

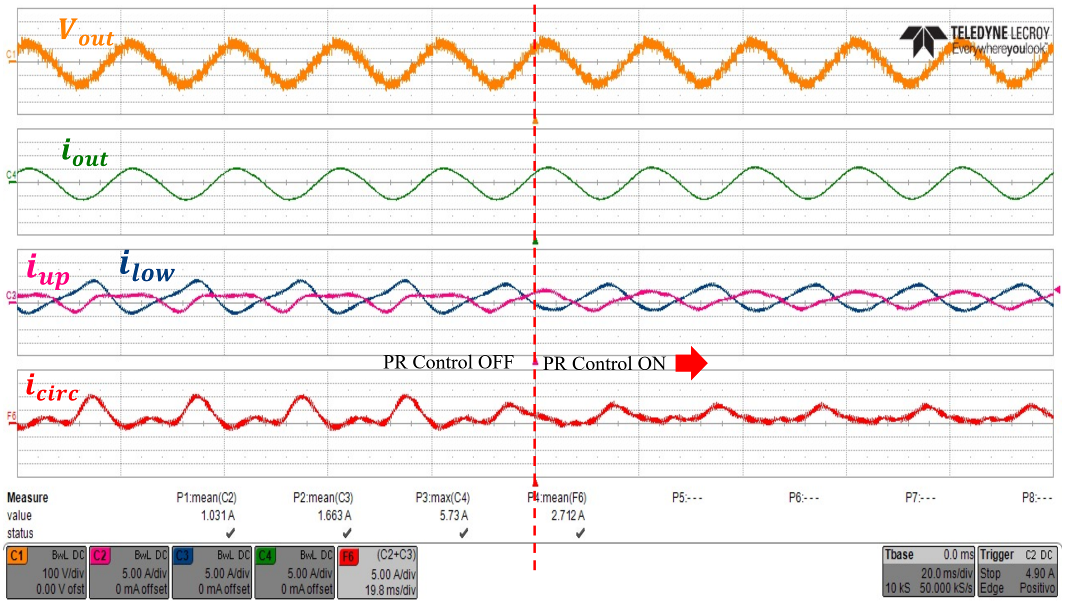

Figure 4.8: Performance of direct control for reducing circulating current through a PR controller, where V_{out} is the output voltage, i_{out} is the output current, i_{up}, i_{low} are the upper and lower arm currents and $i_{circ}$is the circulating current.

Table 4.1: Parameters of the PR Circulating Current Control

Symbol	Description	Value
k_i	Resonant controller gain	250
k_p	Proportional controller gain	8
ω_c	Resonant controller width	0.001
ω_0	Resonant controller frequency	628
f_s	Sampling frequency	100 kHz

4.3.2 Indirect Methods

Indirect techniques, on the other hand, act on the energy of the two converter arms as the main control channel to ensure the balancing of capacitor voltages, while the circulating current is reduced accordingly as a secondary effect [87]. Among the indirect control methods, non-linear techniques like model predictive control can also be classified, where through accurate dynamic modeling of the converter, different control targets can be pursued at the same time [96]. However, indirect methods are not as effective as direct techniques in reducing the circulating current [97]. These methods rely heavily on model accuracy and are sensitive to system disturbances and parametric variations. Additionally, the presence of many control targets in an MMC makes it difficult to develop efficient predictive algorithms since cost function normalization and weighting coefficients may be complex to define and tune.

4.3.3 Injection-Based Methods

Circulating current control techniques based on signal injection have been recently proposed and investigated in the literature. This family of techniques makes use of a purposefully built circulating current waveform to reduce either the circulating current itself or the capacitor voltage ripple of the submodules [98–102]. Authors in [98] proposed an offline algorithm to calculate two different optimized circulating current signals; one composed of second harmonic component only and the other also including the fourth one. The optimal circulating currents are injected into the phase- leg current control reference voltages to target specific harmonic components of the submodule capacitor voltage ripple. However, an extensive look-up table including the amplitude and phase of the current as a function of the modulation index is required to generate the injection signal calculated with an offline genetic algorithm optimization. The algorithm considers all possible operating conditions of the converter and requires long time to complete the minimization A second drawback is that solutions found for high modulation index values tend to bring the submodules to work in the overmodulation region. While the achieved capacitor voltage ripple minimization can be beneficial, overmodulation introduces new considerations for both implementation and stability.

In [99], the minimization of the submodule capacitor voltage ripple is also chosen as the primary objective for the control of the second-harmonic component of the circulating current. However, the circulating current is not suppressed and the increased thermal stress that the injection of the optimized circulating current can cause in the converter is not evaluated. Another closed-loop control technique based on the injection of second order circulating current is presented in [100] that is based on the real-time information of the MMC to generate circulating current injection references to pursue different targets. The authors introduce a mathematical model to understand the impact of the injection on capacitor voltage ripple and effective arm current, aiding in determining the injection ratio. The optimal circulating current reference is calculated with analytical equations based on the measure of the three phase currents, the phase angle of the output voltage, and the instantaneous values of the modulating signals. In this way, the authors avoid using extensive look-up tables and the circulating current closed-loop control is implemented using a PR controller. A detailed investigation on the effects of the injection of second-order harmonic component of the circulating current in the modulating signals has been carried out in [101]. The authors provide guidelines on how the control of the circulating current can influence the performance of the MMC, deriving analytical expressions that are useful for identifying the optimal amplitude of the injected signal for different control targets. To reduce the second-order harmonic component of the circulating current, in [102] a feed-forward technique is implemented to inject second harmonic voltage into the reference signals using the instantaneous measurement of output and dc currents. The method is based on an analytical model relying on the harmonic functions initially proposed in [62]. However, the proposed analytical approach has not been implemented neither in simulation nor experimentally. The authors only simulate an approximate analytical model considering only the second harmonic, assuming that the circulating current is composed solely of it.

Chapter 5

Sigle-Cell-Based Injection Method

In this thesis, a circulating current control is proposed using an injection method applied to a single cell per arm of the MMC. Indeed, the proposed method, called ”Single-Cell-Based-Injection-Methods (SCBI)”, employs only one submodule per arm as an active compensator for reducing the harmonic components of the circulating current. The objective of the proposed technique is to achieve precise mitigation of the circulating current and reduction of the submodule voltage ripple with a simple but effective feedforward control action. Compared to other methods proposed in the literature [98–102], the novel contribution of this injection technique is the leveraging the direct measurement of the circulating current to inject all low-frequency harmonics of the circulating current, being only limited by the bandwidth of the current sensors, avoiding inaccuracies due to the estimation process, frequency fluctuations, and with minimal impact on the operation of the converter in terms of power losses. The injection technique proposed in this thesis is a simple approach that works in real-time, avoiding the use of lookup tables and coordinate transformations. This chapter is dedicated to a detailed description of the proposed Single-Cell-Based Injection method. It will begin with a description of the block diagram of the control scheme and the fundamental equations for generating the injection signal. Then, to determine guidelines for the tuning of the injection signal, the analytical treatment of the circular interactions that govern the operation of the MMC is described, in such a way that the internal dynamics of the converter can be represented and the analytical expression of the circulating current as a function of the injected signal can be identified through the proposed method. The results of simulations and experimental tests will be shown in Chapter 6 and demonstrate that the proposed injection approach can significantly reduce both the circulating current and the voltage ripple of the sub-module capacitor.

5.1 Proposed Injection Method

The proposed injection technique aims at suppressing the ac component of the circulating current, i_{xz}^{AC}, calculated in 3.10. To this purpose, an ac signal directly proportional to the ac component of the circulating current is injected into the reference voltage of a single submodule per arm that acts as a compensator for the total circulating current. All the other submodules in the arm continue to operate normally, generating the voltage levels required for the converter operation. The main idea is to implement a simple and computationally inexpensive method for suppressing the circulating current, considering all low-frequency harmonics of the circulating current in the injected signal. The SCBI method not only mitigates the circulating current but also reduces the voltage ripple across all submodule capacitors of the MMC and the RMS of the arm currents. As a result, it leads to improved performance compared to the conventional PR circulating current control. Moreover, the SCBI approach minimizes losses and improves overall converter performance without oversizing the compensating submodule or derating of the converter's operation. The block diagram of the proposed SCBI technique is depicted in Fig. 5.1. The injection signal is implemented in the form of a feedforward control action and is added to the modulating signal of one submodule per arm, which in turn is calculated by the output current control loop. The circulating current signal is derived from the measured instantaneous values of the arm currents using 3.9. The dc component of the circulating current is related to the active power flow through the converter; therefore i_{xz}^{DC}, can be estimated as one-third of the dc-bus current i_{dc}, which in turn is calculated through the instantaneous power balance between the ac and dc side of the converter, assuming that the converter losses are small and can be neglected [103].

$$i_{dc} = \frac{\sum p_x}{V_{dc}} = \frac{\sum v_{xi}^* i_{xi}}{V_{dc}} \tag{5.1}$$

where V_{dc} is the DC-Link voltage, p_x is the instantaneous power,i_{xi} is the output current of the generic phase x and v_{xi}^* is the reference of phase x. A voltage signal proportional to i_{xz}^{AC} is then added to the modulating signal of the compensation submodule, which drives its power devices to generate a voltage that can reduce the ac component of the circulating current. A proportional gain K is introduced to adjust the amplitude of the injected signal.

The proposed solution avoids the need for a dedicated controller for each frequency component of i_{xz} to be canceled, as in conventional PR approaches, therefore reducing system complexity and improving suppression accuracy. Furthermore, the number of compensated harmonic components is only limited by the bandwidth of the current sensors and the sampling time of the digital control system.

5.1.1 Definition of gain K

The definition of the proportional gain K is derived from the analysis of the mathematical model of the circulating current derived by applying the KVL on the MMC phase leg shown in Fig. 3.6, neglecting the voltage drop across the armature resistance R_{arm}.

$$\frac{di_{xz}}{dt} = \frac{1}{2L_{arm}}(V_{dc} - v_{xu} - v_{xl}) \tag{5.2}$$

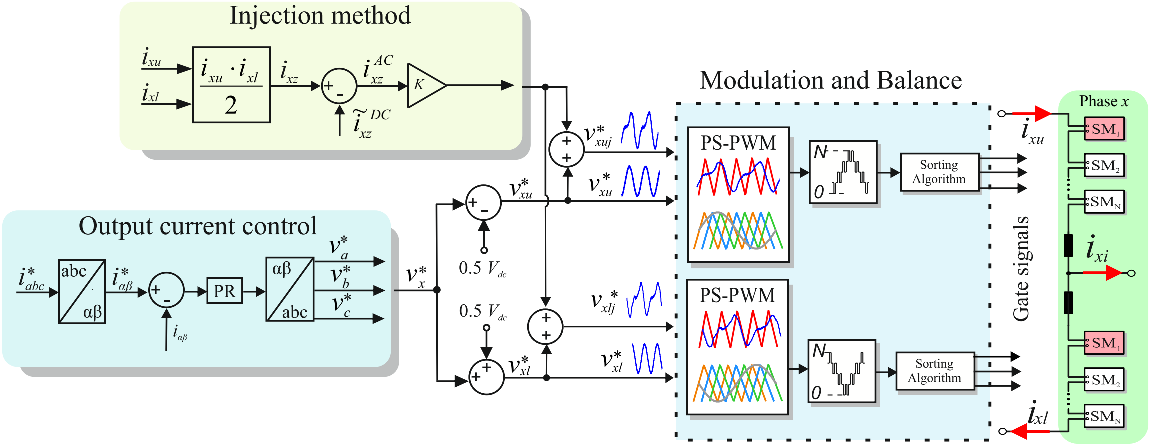

Figure 5.1: Simplified block diagram of the proposed circulating current suppression injection scheme.

In eq. 5.2, v_{xu} and v_{xl} are the upper- and lower-arm voltages, respectively. By substituting i_{xz} in eq. 3.9, it is possible to rewrite the eq. 5.2 as

$$2L_{arm}(\frac{di_{xz}^{DC}}{dt} + \frac{di_{xz}^{AC}}{dt}) = V_{dc} - (v_{xu} + v_{xl}) \tag{5.3}$$

i_{xz}^{DC} is constant in the steady state and its derivative is zero, therefore eq.5.3 can be simplified as follows:

$$2L_{arm}\frac{di_{xz}^{AC}}{dt} = V_{dc} - (v_{xu} + v_{xl}) = v_{xz} \tag{5.4}$$

where v_{xz} represents the voltage that is responsible of the ac part of the circulating current and consists of several harmonic components [62]. Each of these harmonics can be expressed as the product of the respective current harmonic of order n by the arm reactance at the corresponding frequency. The injected voltage v^*_{xz} can thus be expressed as

$$v^*_{xz} = K \cdot i_{xz}^{AC} = \sum_{n=1}^{\inf}[n\omega L_{arm} I_{xz,n} \sin(n\omega t + \Phi_{xz,n})] \tag{5.5}$$

Based on eq 5.5, it is possible to define the gain K as related to the overall harmonic impedance of the arm. However, this equation cannot be solved for K explicitly. To select the gain K, therefore, some assumption must be made. For example, if the second-order harmonic component of i_{xz}^{AC} is assumed to be dominant and that the other harmonics are negligible, the value of K can be calculated as the module of the arm impedance at 2ω.

$$K = \sqrt{(2\omega \cdot 2L_{arm})^2 + R_{arm}^2} \tag{5.6}$$

the value of K can be selected using an analytical model of the steady state of the MMC so that the circular interactions governing the operation of the MMC can be expressed. Using this approach, it is possible to determine the analytical expression of the circulating current and to determine the gain K of the injection signal to be used to obtain a given reduction of the circulating current itself, evaluating the effects of the proposed SCBI on the overall performance of the converter. In the next section, the analytical model used to determine the gain K to be applied to the injection signal will be analysed.

5.2 Steady State Analysis

The analytical models describing the steady state of the electrical quantities of multilevel converters are useful tools for understanding the internal and external dynamics of this converter. There are several mathematical models in the literature analysing the performance and dynamics of the MMC [61, 62, 73, 87, 98, 99, 101, 104–108]. Some of these models are designed to guide the choice of components needed for the converter design [61, 104]. Others focus on control to ensure proper operation of MMC [87, 105], while some are geared towards optimising the injection signals within the converter, generally third harmonic signals [106, 107] and second harmonic signals [99–101]. A general model of the MMC has recently been proposed for the comprehensive study of steady-state performance optimisation for various optimisation objectives [108]. This analytical model is based on an equilibrium equation between the internal quantities and the external quantities of the MMC. To understand the nature of the internal quantities governing the operation of the converter, analytical procedures were proposed to describe its dynamics [62,73]. The choice of inductors and submodule capacitances of the MMC is one of the relevant aspects addressed in the analytical analyses. For example, an analytical analysis of the stationary converter model is proposed in [61] to study and design the arm inductor to avoid resonance phenomena in the MMC. Other studies, such as [104], analyse the energy storage requirements, providing guidelines to determine the size and capacitance of the capacitors of the sub-modules of the MMC.

Third-harmonic signal injection is a commonly used approach to solve the overmodulation problem and make better use of the DC-Link DC voltage [109]. In [106], third-order harmonic voltage injection is used to change the peak value of the capacitor reference voltage towards higher voltage values in order to increase the operating region of the capacitors. The authors then determine the amplitude and phase of the third harmonic signal to be injected for different operating conditions.

In addition, many studies try to optimise the reduction of voltage fluctuations in the capacitors of the MMC submodules to design smaller capacitances and reduce the size and cost of the converter [99, 107].

The analytical expressions of the electrical quantities within the converter are presented in [62], the authors provide a steady-state model of the MMC to understand and approximate how the interactions between the harmonic components flowing in the arm and the phase quantities interact with each other, to determine the detailed analytical expression of the arm current.

In order to understand the circular interactions during the operation of the MMC, an analytical model is developed, as proposed in [73]. This model aims to determine the expression of the circulating current within the MMC, starting from the circular interactions at the level of the individual submodule and analysing the voltage fluctuations in the entire MMC phase. Furthermore, in [101], an analytical treatment is conducted to understand how the control of the circulating current affects the performance of the MMC. This is achieved through a steady-state analysis method, which takes into account the control of the circulating current, providing a theoretical basis for the accurate design of the parameters of the MMC.

In this thesis, an analytical model is developed to analyse the performance of the circulating current control based on the signal injection developed in a single cell of the MMC. The procedure followed in the model is similar to that proposed in [73], but differs in developing a different analytical treatment for submodules that are affected by signal injection and those that are not. This approach makes it possible to determine the phase voltage ripple and to obtain the expression of the circulating current concerning the variation of the signal injected into the submodule, so that the injection signal, proportional to the circulating current, can be determined and implemented in the control to reduce the circulating current itself. The proposed analytical model has been generalised to analyse the effects of signal injection, both when it is applied to all submodules and when it is implemented on only one. This generalization makes it possible to examine and understand the differences between the two approaches and to validate the proposed SCBI method in detail.

5.2.1 Circular Interactions

This section describes the analytical procedure that is performed in this thesis work to determine the circular interactions of the electrical quantities of the MMC. Through the circular interactions, an equation can be established to determine the circulating current flowing in the phase of the MMC, whose second-order harmonic component has a significant amplitude compared to the others. Through the determination of the current ripple, the voltage ripple of the individual submodule, and the subsequent determination of the voltage ripple of the MMC phase, the mathematical relationship for calculating the circulating current can be determined. Indeed, the circulating current is induced by the voltage difference stored in the SM capacitors, in particular, the phase voltage ripple generates the second harmonic of circulating current. The proposed analytical method aims to determine a mathematical relationship that expresses the variation of the circulating current as the signal injected into the individual sub-module varies in order to determine the signal to be injected into the reference of one individual cell to reduce the circulating current. Fig. 5.2 describes the circular interactions for a submodule and the phase leg of the MMC. In particular, this figure describes the steps used in the proposed analytical treatment to describe the interaction of the voltage and current quantities of the MMC, assuming that the generic arm current i_{xy} and the switching function S_1 are known.

Step 1 ***Capacitor Current*** The arm current multiplied by the switching function generates the current flowing in the SM capacitor i_{cSM}.

Step 2 ***Ripple Capacitor Voltage*** The capacitor current generates a corresponding voltage ripple on the submodule capacitor Δv_{cSM} and the capacitor voltage v_{cSM} can be obtained by adding the dc component to the voltage ripple.

Step 3 ***Ripple Voltage of the Submodule Terminal*** the ripple of the capacitor voltage is reflected at the submodule terminal through the switching actions generating the submodule output voltage ripple Δv_{oSM}.

Step 4 ***Ripple Voltage of the Phase*** The sum of the ripple voltages of all submodules within a phase generates a ripple voltage on this phase Δv_x

Step 5 ***Circulating Current*** The ripple voltage across this phase generates the circulating current, which in turn influences the arm current.

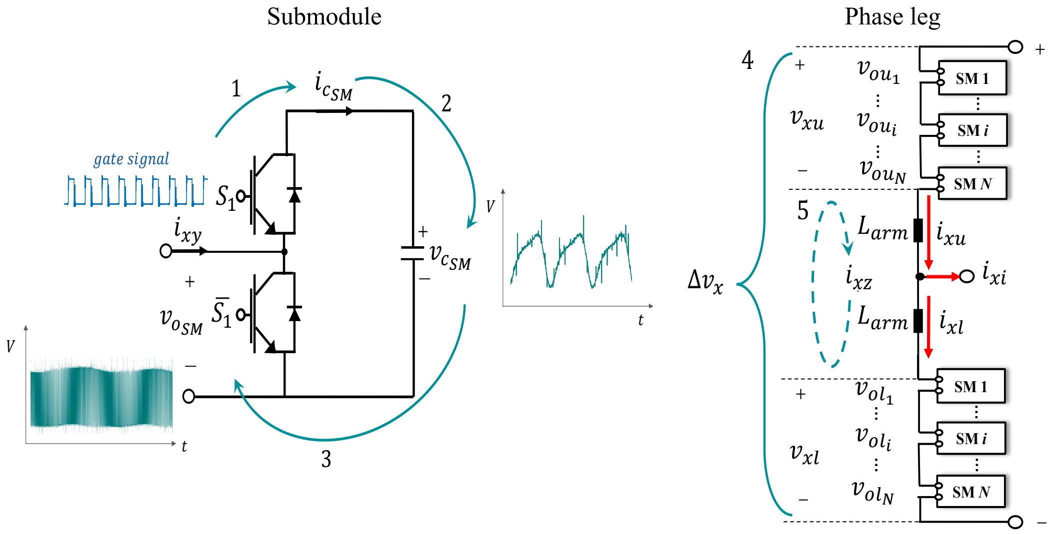

Figure 5.2: Interaction among the voltage and current quantities of a submodule divided into five steps: capacitor current, ripple capacitor voltage, ripple voltage of the submodule terminal, ripple voltage of the phase, and circulating current.

In order to better express the methodology on which the analysis is based, the analytical treatment will be described for the submodule in which the injection signal is applied and for the submodule operating in the absence of the injection signal. The analysis should be started with the arm current. Using phase A as an example, the arm currents are assumed to be expressed as

$$i_{xu} = I_{xz}^{dc} + \frac{I}{2}\sin(\omega t + \phi) + \frac{I_{xz,2}}{2}\sin(2\omega t + \Phi_{xz,2}) \tag{5.7}$$

$$i_{xl} = I_{xz}^{dc} - \frac{I}{2}\sin(\omega t + \phi) + \frac{I_{xz,2}}{2}\sin(2\omega t + \Phi_{xz,2}) \tag{5.8}$$

where I is the peak-to-peak value of the output current and ϕ is the relative phase angle. I_{xz}^{dc} is the dc part of the circulating current of the corresponding phase. The values $I_{xz,2}$ and $\Phi_{xz,2}$ are the peak-to-peak value of the second harmonic component of the ac part and the phase angle of the circulating current respectively.

In this model, $I_{xz,2}$ and $\Phi_{xz,2}$ are unknown and can be determined through the circuit relations derived from this analytical model. The analysis differentiates between the submodule with injection and the submodule without injection through the expression of the switching function. It is important to point out that because each arm of the MMC consists of a large number of submodules, it is common practice to evaluate the average voltage and current quantities of all the submodules in one arm. In this analytical treatment, m denotes the modulation index, and $S_{xu,l}$ are the switching functions related to the N-1 submodules that which the injection signal is not applied. S_{xuj} and S_{xlj} represent the switching functions of the submodule where the injection signal is applied for the upper and lower arms, respectively.

The average switching function for the arms is thus defined as

$$S_{xu} = \frac{1}{2} - \frac{1}{2}m\sin(\omega t) \tag{5.9}$$

$$S_{xl} = \frac{1}{2} + \frac{1}{2}m\sin(\omega t) \tag{5.10}$$

$$S_{xu_J} = \frac{1}{2} - \frac{1}{2}m\sin(\omega t) + \underbrace{\frac{1}{2}K\sin(2\omega t + \beta)}_{InjectionSignal} \tag{5.11}$$

$$S_{xl_J} = \frac{1}{2} + \frac{1}{2}m\sin(\omega t) + \underbrace{\frac{1}{2}K\sin(2\omega t + \beta)}_{InjectionSignal} \tag{5.12}$$

In this way it is possible to distinguish the two phenomena and the contributions of the submodules in terms of voltage ripple both when affected by injection and when operating without injection, considering N-1 submodules without injection and only one submodule when the injection is applied.

The average current flowing through the capacitor can be calculated by multiplying the switching function by the arm current flowing through the considered phase. For both cases, the following expressions can be defined:

$$i_{Cxu} = S_{xu} i_{xu} \tag{5.13}$$

$$i_{Cxl} = S_{xl} i_{xl} \tag{5.14}$$

$$i_{Cxu_J} = S_{xu_J} i_{xu} \tag{5.15}$$

$$i_{Cxl_J} = S_{xl_J} i_{xl} \tag{5.16}$$

The expressions of the average capacitor currents of the upper and lower arm submodules for both cases are expressed in Appendix A through the equations A.1, A.2, A.3 and A.4, respectively. The continuous components dc in the current ripple expressions in the capacitor are zero during the steady state. These components represent the balance between the AC-side active power and the DC-link active power [73].

Furthermore, it is important to note that the components at the fundamental frequency, the second-order and third-order harmonics in the capacitor current are all dependent on the components of the circulating current, such as $I_{xz,2}$ and $\Phi_{xz,2}$. Therefore, taking into account the impact of the circulating current at the beginning of the analysis is crucial to obtaining more accurate analytical expressions. In other words, the expressions for the voltage and current quantities are not explicit until $I_{xz,2}$ and $\Phi_{xz,2}$ are solved.

Therefore, considering the effect of the circulating current from the very beginning of the analysis is crucial to obtain more precise analytical expressions of capacitor voltage, capacitor currents, arm currents, and voltages.

After determining the relations of the current ripple in the submodules, it is possible to integrate the relations 5.13,5.14,5.15, 5.16 and divide by the capacitance of the submodules C to obtain the voltage ripple of the capacitors of the submodules. The voltage ripples of the capacitors are expressed by the following relations:

$$\Delta v_{c_{xu}} = \frac{1}{C} \int i_{Cxu} dt \tag{5.17}$$

$$\Delta v_{c_{xl}} = \frac{1}{C}\int i_{Cxl}dt \tag{5.18}$$

$$\Delta v_{c_{xuJ}} = \frac{1}{C}\int i_{Cxu_J}dt \tag{5.19}$$

$$\Delta v_{c_{xlJ}} = \frac{1}{C}\int i_{Cxl_J}dt \tag{5.20}$$

The complete expressions of the voltage ripple of the capacitors of the submodules for both cases are expressed in Appendix A through the equations A.5,A.6,A.7 and A.8, respectively.

It should be noted that, at a steady state, the sum of the continuous components appearing in the expressions of the capacitor current ripple must be zero, otherwise the capacitor voltage would increase or decrease infinitely. The expression below is derived from the equations A.1, A.2, A.3 and A.4,

$$\frac{I_{xz}^{DC}}{2} + \frac{KI_{xz,2}}{4}\cos(\beta + \Phi_{xz,2}) - \frac{mI}{8}\cos(\phi) = 0 \tag{5.21}$$

The voltage ripple on the DC side of the submodule is reflected on the AC side through the switching of the transistors, resulting in a voltage ripple that can be expressed as follows:

$$\Delta v_{o_{xu}} = S_{xu}\Delta v_{c_{xu}} \tag{5.22}$$

$$\Delta v_{o_{xl}} = S_{xl}\Delta v_{c_{xl}} \tag{5.23}$$

$$\Delta v_{o_{xuJ}} = S_{xu_J}\Delta v_{c_{xuJ}} \tag{5.24}$$

$$\Delta v_{o_{xlJ}} = S_{xl_J}\Delta v_{c_{xlJ}} \tag{5.25}$$

The complete expressions of the voltage ripple $\Delta v_{o_{xlJ}}$ are expressed below for both cases in Appendix A in A.9,A.10,A.11 and A.12, respectively.

5.2.2 Total Ripple Voltage Across the Phase

Considering the application of Kirchhoff's law to the internal circuit of the MMC, from which the continuous-time model of the circulating current has been derived, as indicated in Equation 3.12, provided below for convenience, and neglecting the voltage drop across the armature resistance R_{arm}, it can be expressed as follows:

$$\frac{di_{xz}}{dt} = \frac{1}{2L_{arm}}(V_{dc} - v_{xu} - v_{xl}) = \frac{1}{2L_{arm}}(V_{dc} - v_{xph}) \tag{5.26}$$

where v_{xph} represents the voltage of phase x of the MMC, which corresponds to the sum of the voltages across all submodules in the upper and lower armature.

Therefore, for each arm, considering the first submodule with injection and the remaining N-1 submodules without injection, the phase voltage can be calculated as follows:

$$\begin{aligned} v_{xph} = {} & (\frac{V_{dc}}{N} + \Delta v_{cxu_J})S_{xu_J} + \sum_{n=2}^{N}(\frac{V_{dc}}{N} + \Delta v_{ncxu})S_{nxu} \\ & + (\frac{V_{dc}}{N} + \Delta v_{cxl_J})S_{xl_J} + \sum_{n=2}^{N}(\frac{V_{dc}}{N} + \Delta v_{ncxl})S_{nxl} \end{aligned} \tag{5.27}$$

The eq. 5.27 can be generalised by considering for each arm, h submodules with injection and $N - h$ submodules without injection, the phase voltage can be calculated as follows:

$$\begin{aligned} v_{xph} = {} & \sum_{n=1}^{h}[(\frac{V_{dc}}{N} + \Delta v_{ncxu_J})S_{nxu_J}] + \sum_{n=h+1}^{N}[(\frac{V_{dc}}{N} + \Delta v_{ncxu})S_{nxu}] \\ & + \sum_{n=1}^{h}[(\frac{V_{dc}}{N} + \Delta v_{ncxl_J})S_{nxl_J}] + \sum_{n=h+1}^{N}[(\frac{V_{dc}}{N} + \Delta v_{ncxl})S_{nxl}] \end{aligned} \tag{5.28}$$

from which we can derive the following relationship:

$$\begin{aligned} v_{xph} &= V_{dc} + \frac{1}{2} hK \frac{V_{dc}}{N} sin(2\omega t + \beta) + h(\Delta v_{o_{xuJ}} + \Delta v_{o_{xlJ}}) + \\ &+ (N - h)(\Delta v_{o_{xu}} + \Delta v_{o_{xu}}) = V_{dc} + \Delta v_{xph} \end{aligned} \tag{5.29}$$

where v_{xph}, Δv_{xph} are the voltage and the ripple across the generic phase x, V_{dc} is the DC-Link voltage, N is the number of submodules, K is the gain of the injection signal, $\Delta v_{o_{xuJ}}$ $\Delta v_{o_{xlJ}}$ are the voltage ripple of submodule terminals affect by the injection signal for upper and lower arms. $\Delta v_{o_{xu}}$ $\Delta v_{o_{xl}}$ are the voltage ripple of the submodule for both arms in the case no injection is applied.

5.2.3 Circulating Current Expression

The phase voltage v_{xph} expressed in 5.29 has both second- and fourth-order harmonic components that generate the current circulating in the converter phase at the corresponding frequency [62, 73]. For this analytical model, only the second harmonic of the MMC phase voltage ripple is considered by summing all second-order components that appear in the phase voltage expression.

Therefore, the second harmonic of the phase voltage ripple is expressed as:

$$\begin{aligned} \Delta v_{xph_2} = &-\frac{1}{96\omega C}[24NI_{xz,2}\cos(2\omega t + \Phi_{xz,2}) + 24hKI_{xz}^{DC}\cos(2\omega t + \beta) \\ &+ 24Nm^2 I_{xz}^{DC}\sin(2\omega t) - 18NmI\sin(2\omega t + \phi) + 3hM_2^2 I_{xz,2}\cos(2\omega t + \Phi_{xz,2}) \\ &+ 16Nm^2 I_{xz,2}\cos(2\omega t + \Phi_{xz,2}) - 6hmKI\cos(2\omega t + \beta - \phi) \\ &- 2hmKI\cos(2\omega t + \beta + \phi) - 96hK\frac{V_D C}{N}\omega C\sin(2\omega t + \beta)] \end{aligned} \tag{5.30}$$

Substituting the equation 5.30 into the equation 5.26, one obtains the following equation which allows one to calculate the amplitude and phase of the second harmonic of the circulating current as parameters K and β vary.

$$\begin{aligned}
&I_{xz,2}\sin(2\omega t+\Phi_{xz,2}) = -\frac{1}{2L_{arm}}\int \Delta v_{xph_2}dt = \\
&= \frac{1}{384\omega^2 L_{arm}C}[24NI_{xz,2}\sin(2\omega t+\Phi_{xz,2}) + 24hKI_{xz}^{DC}\sin(2\omega t+\beta) \\
&- 24Nm^2 I_{xz}^{DC}\cos(2\omega t) + 18NmI\cos(2\omega t+\phi) + 3hK_2 I_{xz,2}\sin(2\omega t+\Phi_{xz,2}) \\
&+ 16Nm^2 I_{xz,2}\sin(2\omega t+\Phi_{xz,2}) - 6hmKI\sin(2\omega t+\beta-\phi) \\
&- 2hmKI\sin(2\omega t+\beta+\phi) + 96hK\frac{V_D C}{N}\omega C\sin(2\omega t+\beta)]
\end{aligned} \tag{5.31}$$

The previous equation is solved using the auxiliary angle method, as shown below:

$$\begin{aligned}
&I_{xz,2}[1-\frac{(3hK^2+16Nm^2+24N)}{(384\omega^2 L_S C)}]\sin(2\omega t+\Phi_{xz,2}) = \\
&A\sin(2\omega t) + B\cos(2\omega t) = \sqrt{A^2+B^2}\sin(2\omega t+\theta)
\end{aligned} \tag{5.32}$$

$$\begin{aligned}
&A = \frac{1}{384\omega^2 L_{arm}C}[24hKI_{xz}^{DC}\cos(\beta) - 18NmI\sin(\phi) - 2hKmI\cos(\beta+\phi) \\
&- 6hMKmIcos(\beta-\phi) - 96hK\frac{V_{DC}}{N}\omega C\sin(\beta)] \\
&B = \frac{1}{384\omega^2 L_{arm}C}[-24Nm^2 I_{xz}^{DC} + 24hKI_{xz}^{DC}\sin(\beta) + 18NmI\cos(\phi) \\
&- 2hmIsin(\beta+\phi) - 6hKmI\sin(\beta-\phi) + 96hK\frac{V_{DC}}{N}\omega C\cos(\beta)]
\end{aligned} \tag{5.33}$$

Note that, the peak-to-peak value of the output current I and its relative phase angle ϕ and the dc part of the circulating current of the corresponding phase I_{xz}^{dc} are known or can be calculated from the operating conditions of the MMC. Parameters such as m, V_{dc},C and L_{arm} are the converter's data. The variables belonging to the injection signal such as amplitude K and phase β can be considered known as they are derived from the proposed control. Therefore, the only unknown variables are the amplitude of the circulating current I_{xz} and its phase Φ_{xz} can be calculated as follows:

$$I_{xz,2} = \frac{\sqrt{A^2+B^2}}{1-\left(\frac{3hK^2+16Nm^2+24N}{384\omega^2 L_{arm}C}\right)} \tag{5.34}$$

$$\begin{cases} \Phi_{xz,2} = \theta = \arctan\left(\frac{B}{A}\right) if A > 0 \\ \Phi_{xz,2} = \theta = \pi + \arctan\left(\frac{B}{A}\right) if A < 0 \end{cases} \tag{5.35}$$

The present analytical approach can be extended to the generic three-phase case by also considering the other two phases b and c, introducing the angle θ_x into the equations of the switching functions 5.11 5.12 and in the expression of arm currents 5.7 and 5.8, so that the second harmonics of the circulating current in the three phases and the injected second harmonics constitute terns of inverse sequence.

$$S_{xju,l} = \frac{1}{2} \mp \frac{1}{2} m \sin(\omega t + \theta x) + \frac{1}{2} K \sin(2\omega t + 2\theta x + \beta) \tag{5.36}$$

$$i_{xu,l} = I_{xz}^{dc} \pm \frac{I}{2} \sin(\omega t + \theta x + \phi) + \frac{I_{xz,2}}{2} \sin(2\omega t + 2\theta x + \Phi_{xz,2}) \tag{5.37}$$

where $\theta_x \in 0, \frac{-2\pi}{3}, \frac{-4\pi}{3}$.

The analytical explicit expressions for the different voltage and current quantities can be obtained after substituting the resolved variables of I_{xz} and Φ_{xz} into the equations in Appendix A. On the basis of these analytical expressions, it is possible to theoretically analyse the effect of the voltage signal proportional to the circulating current on the performance of the MMC.

5.3 SCBI Techniques Effects on MMC Performance

Once the expressions by which the amplitude and phase of the second harmonic of the circulating current can be calculated are determined, in this paragraph, the effects that the proposed injection technique has on the performance of the MMC are shown. The proposed steady-state analytical model and analytical equations were implemented on MATLAB/Simulink. The used parameters of the MMC are summarized in the following table 5.1:

Table 5.1: Modular Multilevel Converter Parameters.

Parameter	**Value**
Number of SM N	3
DC-Link Voltage V_{DC}	600 V
Arm Inductance L_{arm}	10 mH
SM Capacitor C	500 μF
Load Resistance R	50 Ω
Load Inductance L	6.5 mH
Output Current I	4.796 A
Modulation index m	0.8
Fundamental frequency f	50 Hz

In the following paragraphs, graphs are presented on the amplitude of the second harmonic of the circulating current and the voltage ripple of the capacitors of the submodules, as the β and K parameters vary. The corresponding 2-D curves for different values of K are shown in the following paragraphs. The characteristics of these indices when varying the injected second harmonic reference voltages are analysed in detail as follows.

5.3.1 Second-Harmonic Circulating Current Amplitude

As shown in Fig. 5.3, for a certain value of K, the variation of β significantly affects the amplitude of the circulating current. In particular, a reduction in the second harmonic of the circulating current is evident as the phase β increases, until it reaches a minimum when $\beta = 180$. For angles greater than 180 the current increases progressively. At $\beta = 180$, the second harmonic of the circulating current decreases as the value of K increases from $0 - 0.06$. Indeed, at $\beta = 180$ and $K = 0.06$, we obtain the largest reduction in circulating current of $0.24A$ in our case. However, by further increasing the amplitude of the injected signal $K > 0.06$ we obtain an increase in the circulating current until we reach, at $K = 0.108$, a current with the same amplitude but opposite phase to that obtained initially without injecting any signal $K = O$, thus reaching the Reverse Circulating Current condition.

The reverse condition is harmful to the converter as it generates an increase in losses and distortion on the capacitor strains, making the converter control unstable.

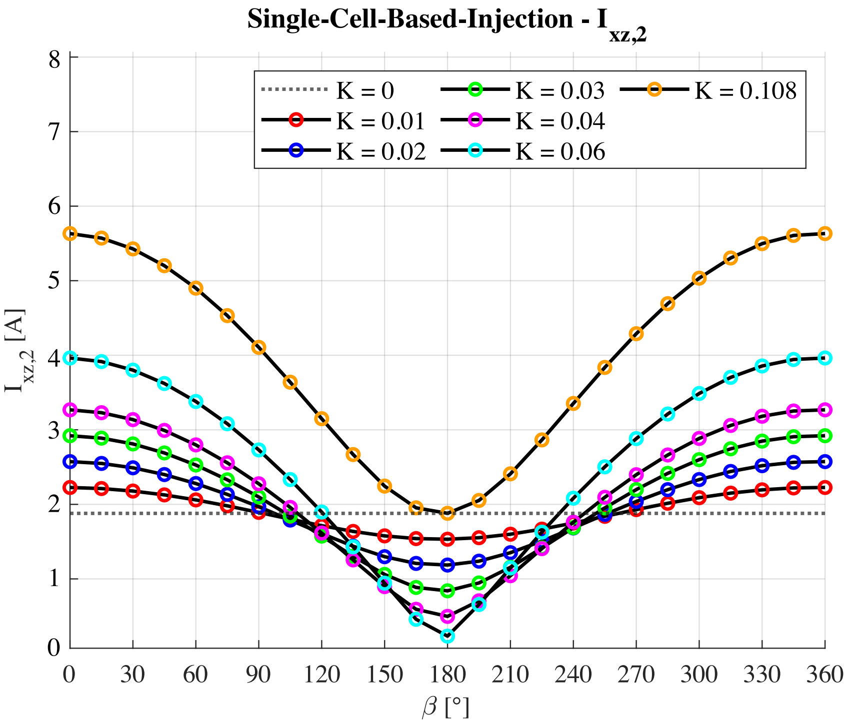

Figure 5.3: Amplitude of the second harmonic of the circulating current $I_{xz,2}$ as K and β change when the single cell based method is applied.

In Fig. 5.4, a comparison is shown between the technique implemented in this thesis work, based on the injection of a voltage signal proportional to the circulating current in only one submodule per arm, and the same technique implementing instead the injection for all submodules. What emerges is that compensation of the

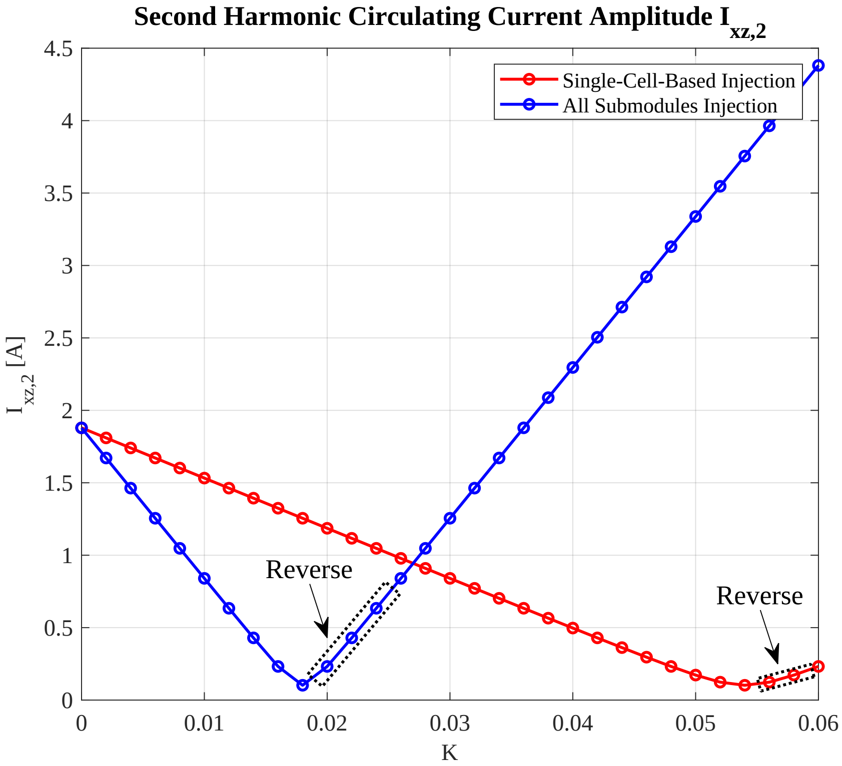

Figure 5.4: Variation of the amplitude of the second harmonic of the circulating current varying by K with the phase of the injected signal equal to $\beta = 180$ for the case in which injection is made only for one submodule per arm (SCBI) and for the case in which injection is applied to all submodules.

circulating current is more easily achieved by injecting the same signal into all the submodules, but a reverse condition is reached more quickly, which can worsen the functionality of the converter. By implementing the SCBI technique appropriately, the condition of reduced circulating current can be reached and the slope of the curve leading to the reverse condition is smoother. The SCBI technique has a wider control range, which allows for greater flexibility in terms of tuning of the control techniques.

5.3.2 Capacitor Voltage Ripple Ratio

The injection also affects the voltage ripple V_{rpl}, as shown in Fig. 5.5, the reduction of the voltage ripple is similar to that obtained by the circulating current $I_{xz,2}$.

V_{rpl} reaches the minimum values for an angle β of 180. Furthermore, the minimum ripple is reached at $K = 0.108$, i.e. in the reverse circulating current condition. However, in this condition the second harmonic voltage injected increases the circulating current, the rms value of the arm current, and the peak value of the phase current. increasing the losses in the converter.

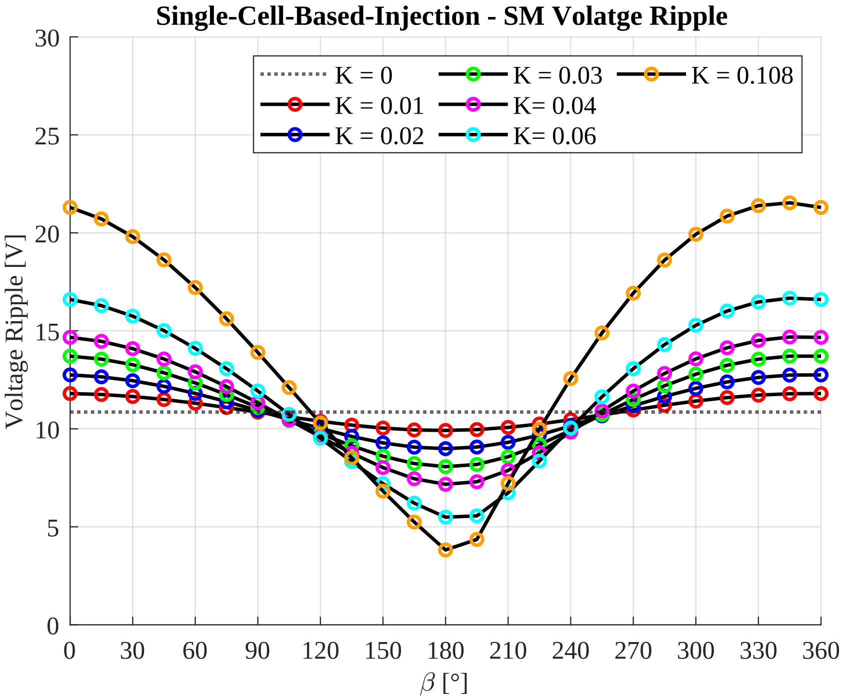

Figure 5.5: Submodules voltage ripple V_{rpl} as K and β change when the single cell based method is applied.

5.3.3 Simulation and Analytical waveforms

To validate the steady-state model, the analytical waveforms derived from the expressions of the circular interactions are compared with those obtained by a detailed model of an MMC implemented in the MATLAB/Simulink environment. The converter model is implemented with the same parameters and data of the experimental set-up listed in Table 5.1. The modulation strategy employed is Phase-Shift PWM, with a switching frequency of 5 kHz for each IGBT of the converter.

The Figures 5.6, 5.7, 5.8 and 5.9 show the output voltage of the MMC the arm currents, the voltage of the submodule capacitance and the circulating current as the injection signal injected into the single submodule per arm varies.

The analytical and simulation results concur well, which validates the accuracy of the proposed steady-state analysis method. The effect of the injection signal is validated and agrees with the reduction of the circulating current for the angle value $\beta = 180$ and amplitude $K = 0.06$ as derived analytically. Furthermore, with the amplitude value of the induced voltage signal equal to $K = 0.108$, the reverse condition of the circulating current is reached with the same amplitude, but with the opposite phase as shown in figure 5.9.

From Figures 5.6 and 5.8, a decrease in the voltage ripple on the submodule capacitors from 11.5% to 6% is observed when switching from no injection, with $K = 0$, to the use of injection to minimize the circulating current with a value of $K = 0.06$. In the reverse circulating current condition, with $K = 0.108$, the maximum reduction in voltage ripple (about 4%) is obtained.

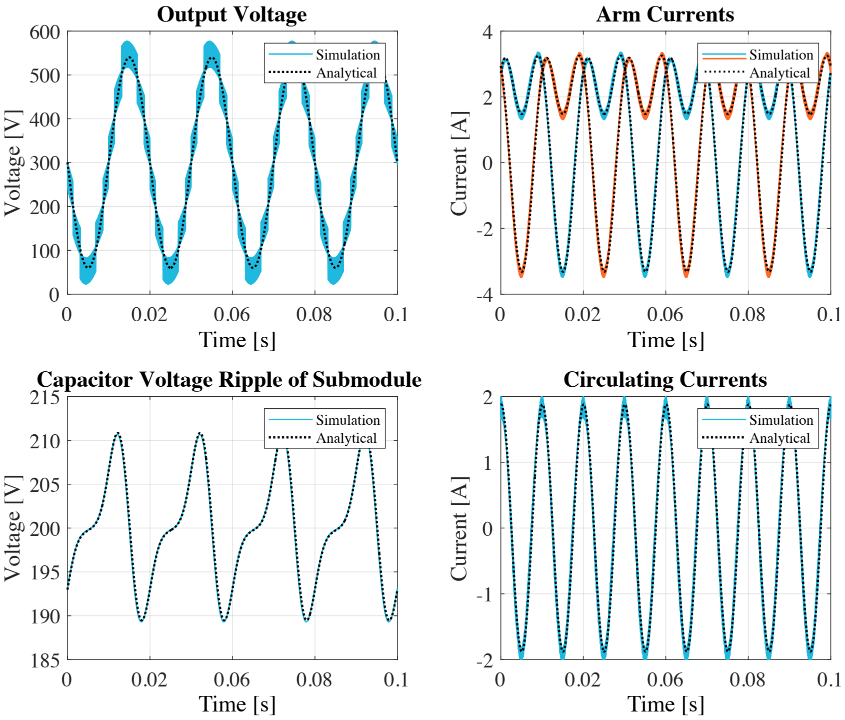

Figure 5.6: Comparison of analytical and simulations result for different waveform with $K = 0$ and $\beta = 0$.

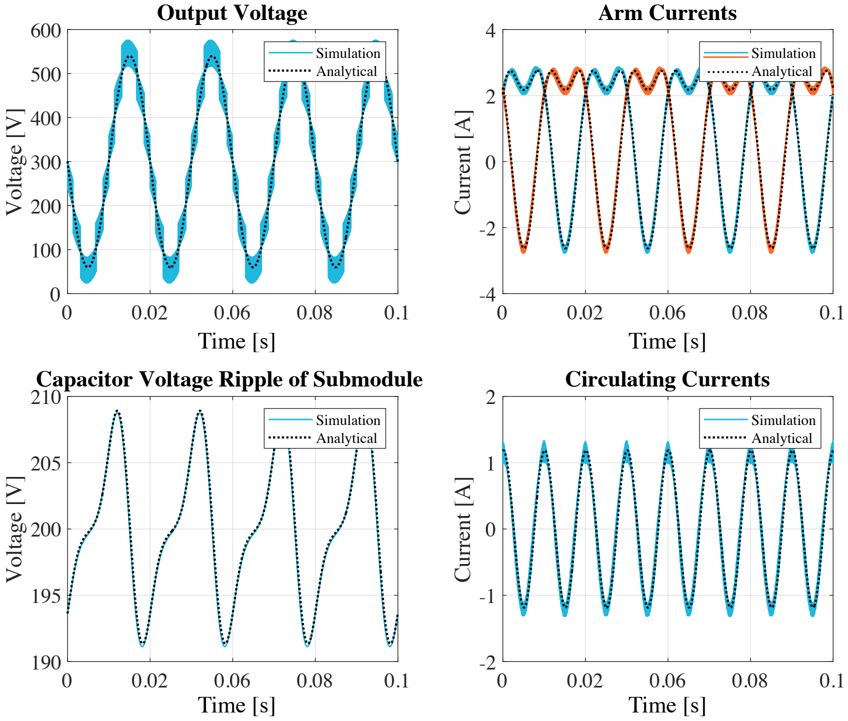

Figure 5.7: Comparison of analytical and simulations result for different waveform with $K = 0.02$ and $\beta = 180$.

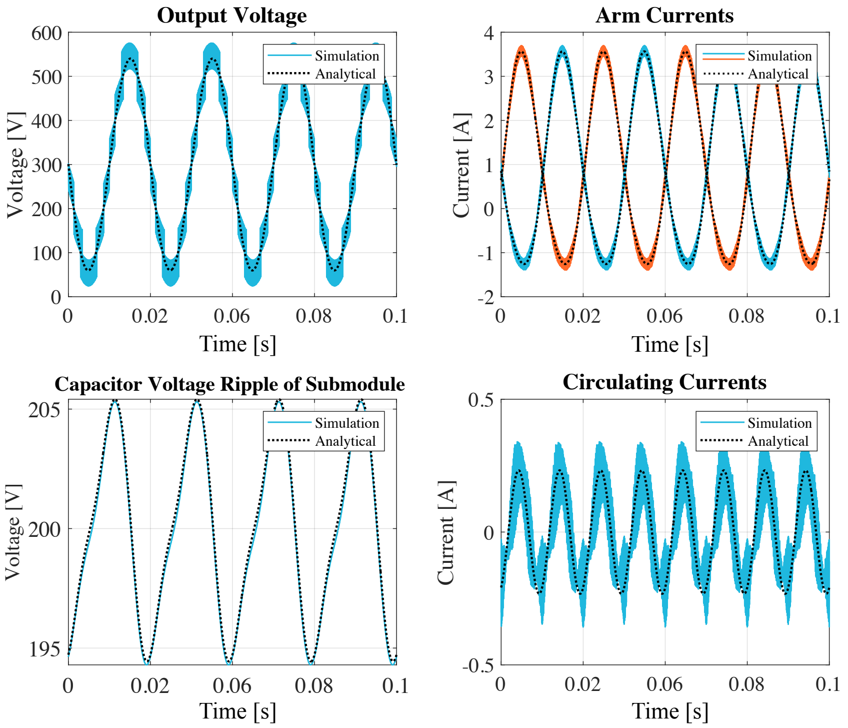

Figure 5.8: Comparison of analytical and simulations result for different waveform with $K = 0.06$ and $\beta = 180$. Minimize Circulating Current.

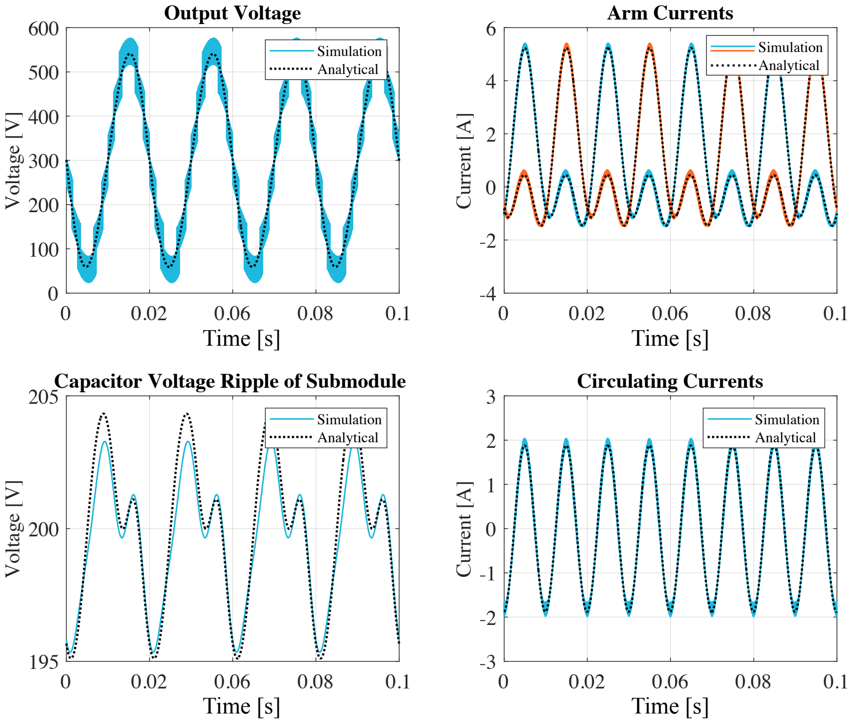

Figure 5.9: Comparison of analytical and simulations result for different waveform setting $K = 0.108$ and $\beta = 180$. Reverse Circulating Current condition.

The table 5.2 shows the value of the amplitude of the second harmonic of the circulating current, rms, and peak value of the arm current and voltage ripple of the capacitors obtained from the analytical expressions and those obtained from the simulations. The variation of I_{rms} follows the same trend as $I_{xz,2}$, which is natural since the rms value of the arm current essentially represents the rms value of the DC, fundamental and harmonic components.

Table 5.2: Comparison of analytical results and simulations: circulating current, peak value, and rms value of arm current and voltage ripple.

K	$I_{xz,2}[A]$	$I_{rms}[A]$	$I_{pk}[A]$	$V_{rpl}[V]$
0	1.879 - 1.894	2.358 - 2.362	3.254 - 3.316	10.855-10.801
0.02	1.186 - 1.204	2.121 - 2.129	2.753- 2.852	8.986-8.886
0.06	0.232 - 0.248	1.955 - 1.964	3.564 - 3.715	5.492-5.281
0.108	1.880 - 1.892	2.358 - 2.367	5.232- 5.363	3.819-3.965

Analytical = blue, Simulations = orange

For a given value of K, it is observed that I_{rms} reaches the minimum when the $I_{xz,2}$ reaches its minimum value. Consequently, the control objective of the technique proposed in this thesis work is to suppress the circulating current and consequently reduce the rms value of the arm current and power losses in the MMC.

5.3.4 Tuning of Injection Signal

The Single-Cell-Based-Injection technique is based on the injection of a voltage signal proportional to the circulating current into an arm submodule to compensate for the circulating current by reducing it, thereby reducing the voltage ripple, the rms value of the arm current and the overall losses of the MMC. The tuning of the implemented injection signal follows the analytical considerations developed in the previous paragraphs. However, it is important to remember that the technique is based on the injection of a voltage signal proportional to the circulating current by including all its harmonics, while the analytical treatment is followed for simplification by considering the circulating current to consist of only the second-order harmonic i.e. the most prominent. The guidelines and considerations developed following the analytical model are still valid and it is therefore possible to derive the gain tuning through the following relationship:

$$\frac{1}{2}K_{analytical} = KI_{xz,2} \tag{5.38}$$

where $K_{analytical}$ is the amplitude of the injection signal calculated analytically, and K is the value of the gain implemented for the circulating current control. From the relationship expressed in 5.38, the expression of gain K can be derived.

$$K = \frac{K_{analytical}}{2I_{xz,2}} \tag{5.39}$$

Therefore, through the relation expressed in 5.39, dividing the value of the gain of the injection signal analytically for which the reduction of the circulating current is obtained and the peak-to-peak value of the circulating current, it is possible to derive the value of the gain K to be used in the control. The following is the table 5.3 in which the respective values of gain K are given.

Table 5.3: Comparison of SCBI with measured circulating current injection and SCBI with second harmonic injection.

K	$I_{xz}[A]$	$K_{analytical}$	$I_{xz,2}[A]$
0.01	1.541	0.031	1.537
0.02	1.096	0.046	1.132
0.03	0.812	0.050	0.822
0.04	0.636	0.051	0.639
0.05	0.519	0.052	0.514
0.06	0.438	0.053	0.451
0.07	0.378	0.054	0.389
0.08	0.333	0.055	0.328
0.09	0.297	0.056	0.304

The effects of the proposed SCBI method and of the proportional gain K on the MMC performance are analysed through simulation in terms of circulating current reduction, submodule voltage ripple, THD of the output voltage, RMS, and Peak value of the arm currents for different power levels ranging from 0.25 to 1.5 per unit. Model parameters are listed in Table 5.1. Fig. 5.10 compares the peak-to-peak amplitude of the ac part of the circulating current, the capacitor voltage ripple, the RMS value, and the peak of the upper-arm current as a function of K at different power levels with the SCBI technique. As shown in Fig. 5.10, the circulating current decreases as K increases up to 0.09, where it reaches a minimum. However, for larger values of K a reverse circulating current is injected into the arm, so that suppression is not achieved anymore. Capacitor voltage ripple, RMS arm current, and its peak value present a similar trend to the circulating current as the gain K changes. The arm currents contain all the harmonic components of the circulating current so that an increase in K will also lead to a reduction in the current rms, thus decreasing the conduction of the MMC. To validate the procedure for adjusting the injection signal gain in Figure 5.11, the waveforms of the arm currents obtained experimentally are compared with those calculated through the analytical formula by setting gain $K = 0.09$ in both cases. The proposed circulating current mitigation centers on K, influenced by arm inductance and resistance. Through a direct measurement and subsequent signal injection, the technique inherently accommodates parameter variations. Notably, the dependence on K is primarily associated with stable parameters, including the number of submodules, switching frequency, arm inductance, and submodule capacitance, which typically remain constant during normal converter operation. A sensitivity analysis addresses uncertainties, revealing that converter resistances minimally impact compared to other variables. Future plans involve detailed analysis, incorporating submodule variations and converter failure simulations, ensuring a robust evaluation of the mitigation system against unexpected changes. This underscores our commitment to resilient solutions, as every parameter variation is inherently accounted for through circulating current measurement and injection.

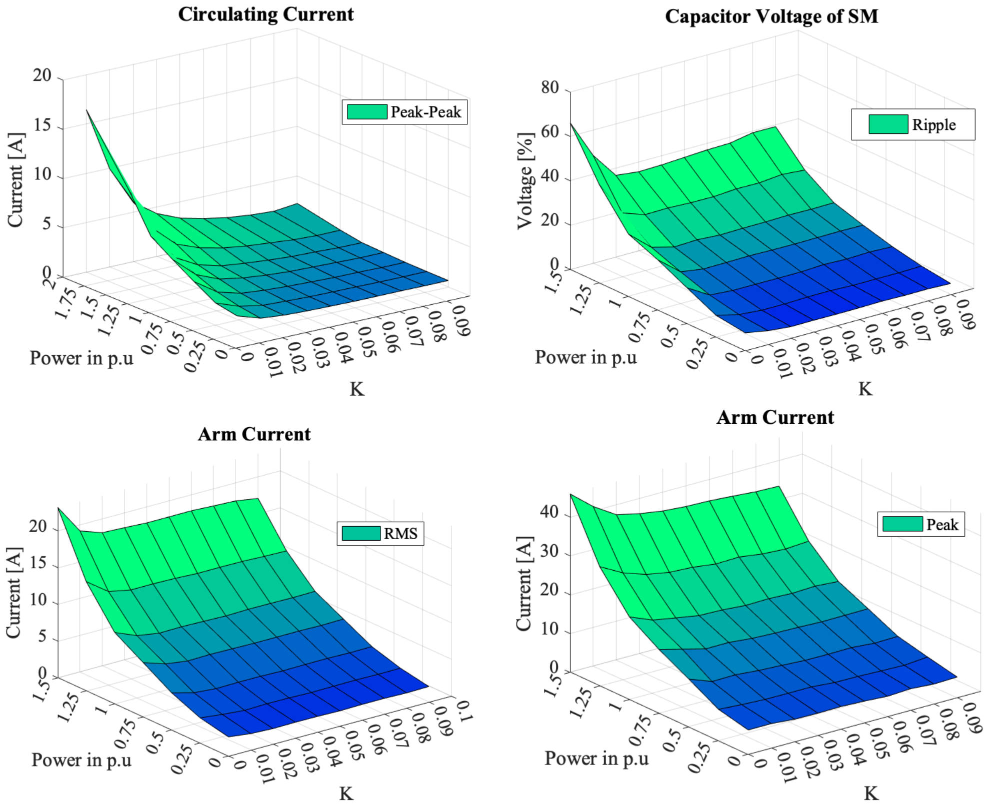

Figure 5.10: Relationship among the circulating current, the capacitor voltage ripple ratio, the rms, and peak of arm current.

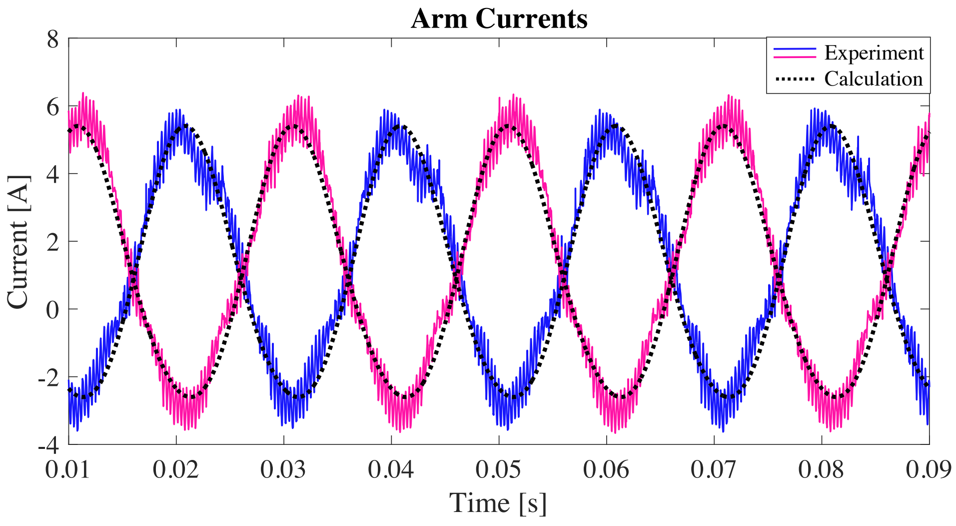

Figure 5.11: Comparisons between the experimental waveform and the calculated result, using gain $K = 0.09$

Chapter 6

Experimental Results

This chapter, begins with a description of the experimental set-up of the Modular Multilevel Converter implemented, designed and tested entirely during the research activity. It consists of several components, and the main features for each are explained. Then, the experimental results obtained during the research activity are presented. The experimental tests are performed on the MMC laboratory prototype shown in the previous chapter in Fig. 6.1, whose characteristics are the same as those used for the models implemented in simulation listed in the table 6.2. The experimental tests were performed with different DC bus voltage levels starting from 200 V up to 600 V with voltage steps of 50 V on a passive ohmic-inductive load, the modulation index was set to the value $m = 0.8$. The modulation strategy used is phase-shifted carrier pulse width modulation (PSC-PWM). The switching frequency for each device is set at 1 kHz. The voltages of the sub-module capacitors are measured on each arm and balanced using the technique described in [65], which identifies the sub-modules to be inserted or deactivated by logic comparators instead of using a sorting algorithm. These tests are necessary to better characterise the proposed technique and its performance in terms of dynamic response, circulating current mitigation, voltage ripple reduction and efficiency. To validate the proposed SCBI technique, the same tests are carried out by implementing conventional circulating current control based on the proportional resonant controller, these tests served as a benchmark, to create a performance comparison between the two techniques.

6.1 Modular Multilevel Converter Prototype

This section describes the experimental set-up designed, built and tested entirely during the PhD activity and on which the tests for the research activity were carried out. The set-up is located at the Power Electronics Laboratory of the Polytechnic University of Bari. It is important to highlight that the set-up is a prototype in scale, the tests are carried out by applying a maximum voltage of 600 V on the DC-link of the converter. Figure 6.1 shows the entire test bench consisting of a three-phase Modular Multilevel Converter inverter, an FPGA control board, a Dead-Time generation board, voltage and current sensors. The design, implementation

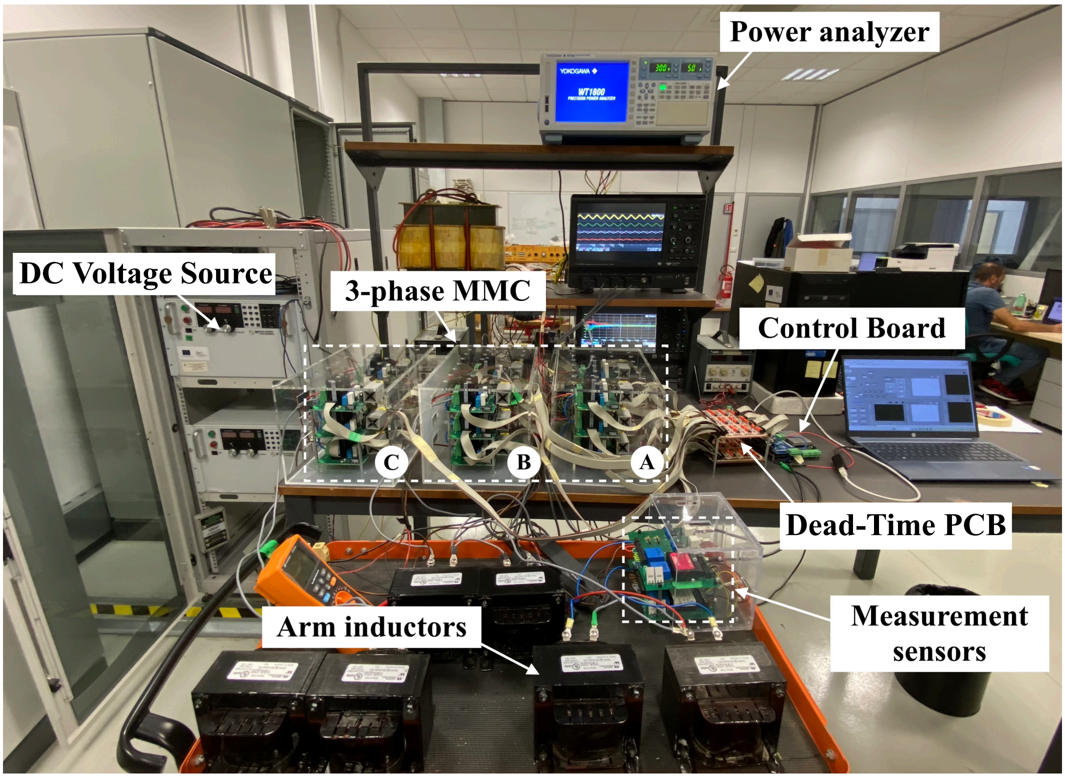

Figure 6.1: Picture of the experimental setup of the MMC.

and control of the entire modular multilevel converter is the focus of the laboratory activity carried out during the three years of the Ph.D. program. The converter consists of three arm submodules and arm inductors designed specifically for this MMC. The submodules are Half-bridges that connected in cascade with each other constitute an arm of the MMC, as show in Figure 6.2. The capacitance of the submodule is 500μF. Arm inductors are sized by following the procedure described in 3.1.2. Table 6.2 shows the parameters of the MMC used during the experimental tests.

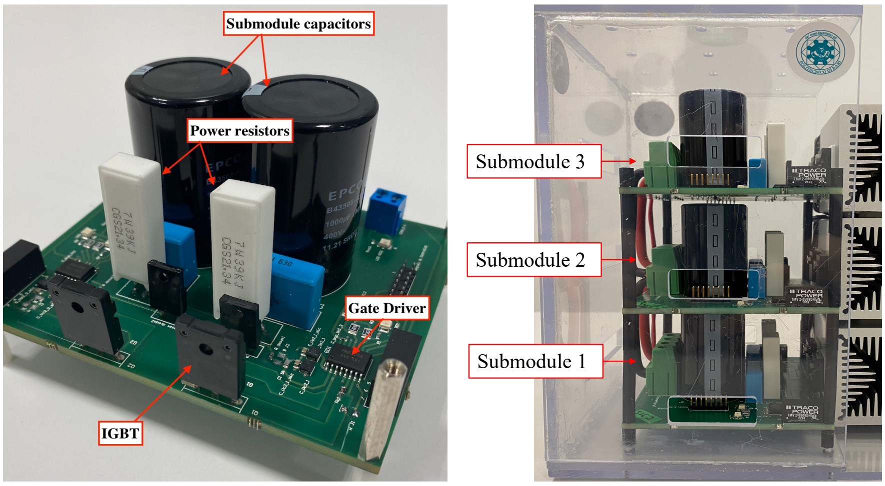

(a)

(b)

Figure 6.2: Pictures of the Half-bridge board (a) and the MMC arm implemented in the lab (b).

Table 6.1: Modular Multilevel Converter Prototype Parameters.

Parameter	Value
Number of SM (HB) N	3
DC-Link Voltage V_{DC}	600 V
Arm Inductance L_{arm}	10 mH
SM Capacitor C	500 μF
Load Resistance R	20 Ω
Load Inductance L	6.5 mH
Output Current I	8 A
Modulation index m	0.8
Fundamental frequency f	50 Hz
Switching frequency f_c	1 kHz

6.2 Control Board

The PWM modulation and control techniques are implemented by programming the Field Programmable Gate Array (FPGA) present on the control board called PED-Board. The programming of the control board is carried out through National Instrument's LabVIEW FPGA software, thus using a simple and easy-to-use block diagram language, compared with conventional VHDL language programming. In addition, to be able to drive all the submodules of the modular multilevel converter, a dead time generation board of 1μs is developed in the laboratory of Power Electronics of the Politecnico di Bari shown in Figure 6.3. The choice to use this board is dictated by the fact that the actual control board used does not have enough PWM outputs to drive all the SMs of the MMC. Therefore, this board can acquire the control signals to be sent to the upper devices of each submodule, negate them, and introduce the designed deadtime through a circuit consisting of integrals. With this solution, the control board will produce only the signals to the upper half-bridge of the submodule, halving overall the gate signals to be generated.

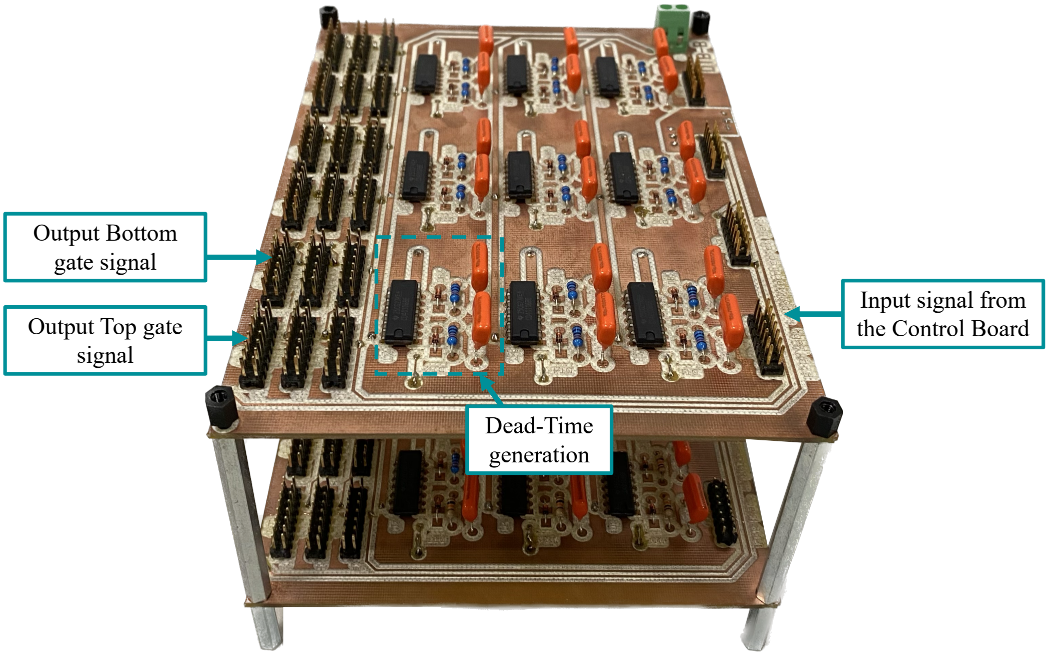

Figure 6.3: The deadtime generation board developed at the Power Electronics laboratory of the Politecnico di Bari.

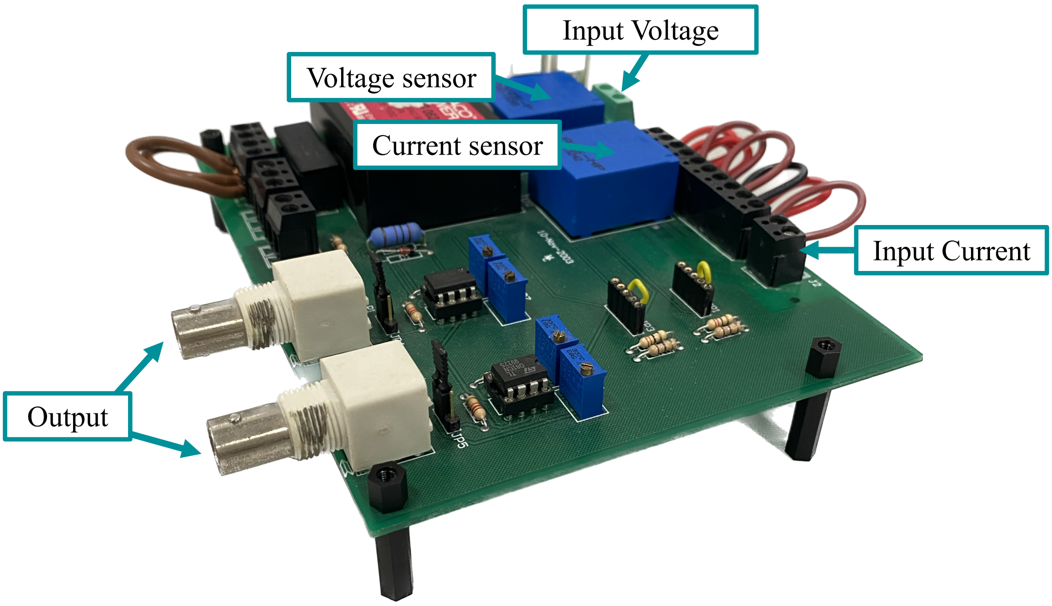

Figure 6.4: Voltage and current measurement board developed at the Power Electronics laboratory of the Politecnico di Bari.

In Figure 6.4 the measurement board used for the acquisition of current and voltage waveforms is depicted. These boards have the primary task of managing the acquisition of voltage and current signals, ensuring they are compatible with the allowable input ranges of various ADC, which cover ranges such as (-5V;+5V) and (0V;+5V). In these acquisition boards, we have chosen to use LEM transducers instead of optocouplers, commonly employed in similar situations. This choice is primarily based on the excellent linearity demonstrated by LEM transducers, both in the presence of alternating current (AC) and direct current (DC). Two specific models of LEM transducers have been identified and selected for this application LV 25-P SP5, ideal for high-voltage measurements and LA 25-NP, optimal for current measurements. These targeted selections have been made to ensure precise signal acquisition and proper adaptation to the voltage and current requirements in three-phase conversion circuits.

6.3 PR circulating current control

The majority of circulating current controls used for the modular multilevel converter are based on proportional resonant regulators, which is why the PR control described in 4.3.1 was chosen as the benchmark for the proposed technique. Fig. 6.5 shows the waveforms of the MMC obtained by setting a dc-link voltage of $600V$ and an output current of $8A$. The second harmonic component is reduced and the arm voltages are more sinusoidal. The rms of the arm currents assume values close to $5.11A$, a peak value of $9.96A$ for the lower arm current, and about $6.71A$ for the upper arm current.

Fig. 6.6 shows the waveforms of the upper and lower arm currents and the circulating current before and after the action of the PR control. The red waveform represents the circulating current obtained by summing the currents of the two arms with the mathematical functions of the oscilloscope. The peak-to-peak value of the circulating current through the control action is reduced by 38.98% and the rms value is 1.4 A.

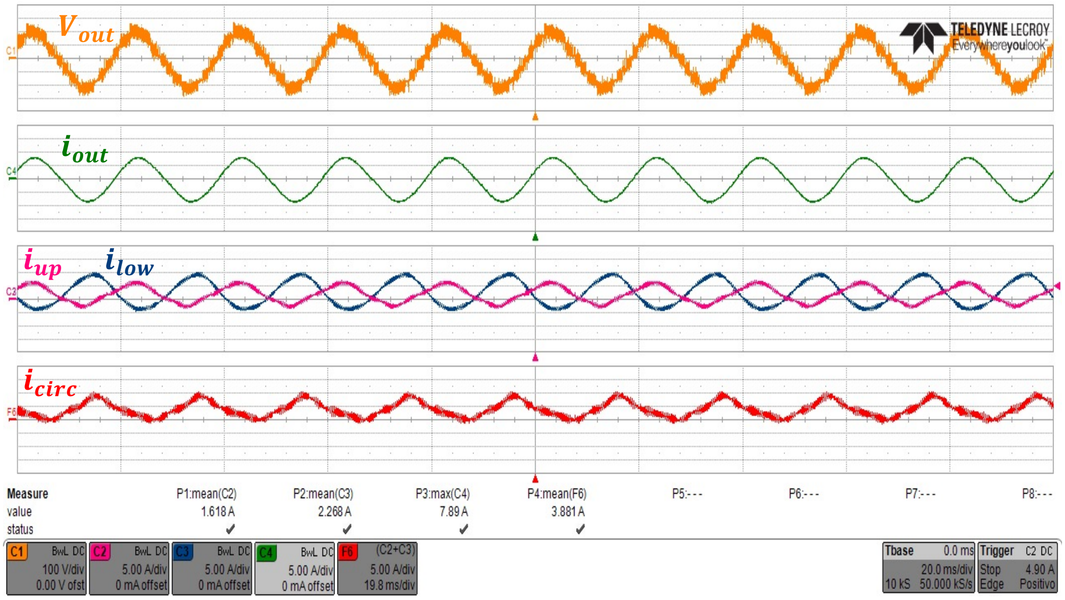

Figure 6.5: Experimental waveform of the output voltage, output current, the arm currents, and the circulating current with the PR control active.

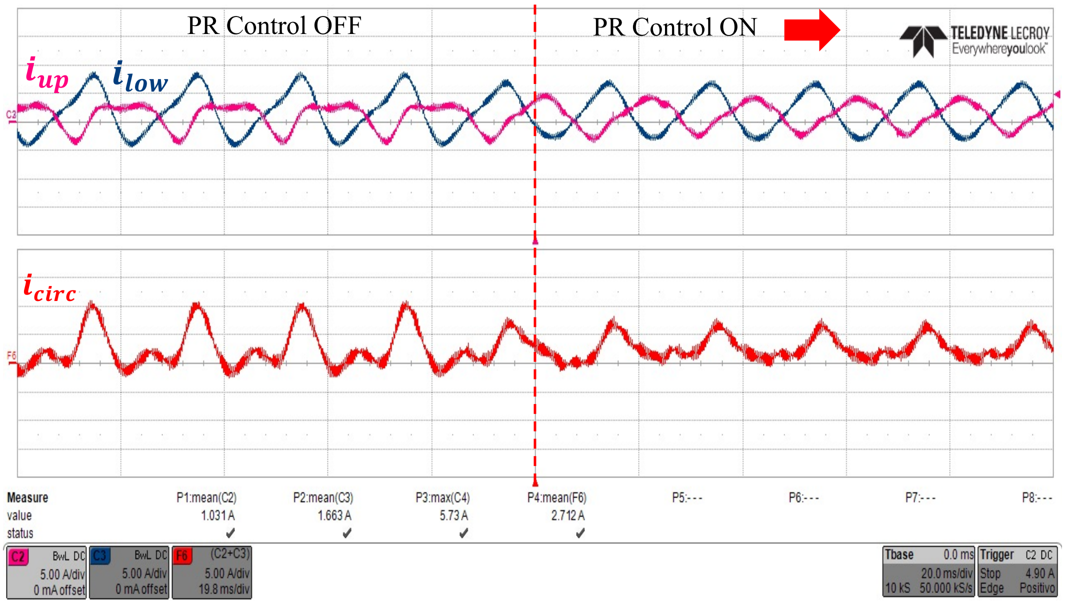

Figure 6.6: Experimental waveform of upper- and lower-arm currents and the circulating current before and after the application of the conventional PR control technique.

Fig. 6.7 shows the harmonic spectra of the upper-arm current obtained with the conventional PR control and without the control action, it can be observed that the second harmonic component is reduced by 71.5%.

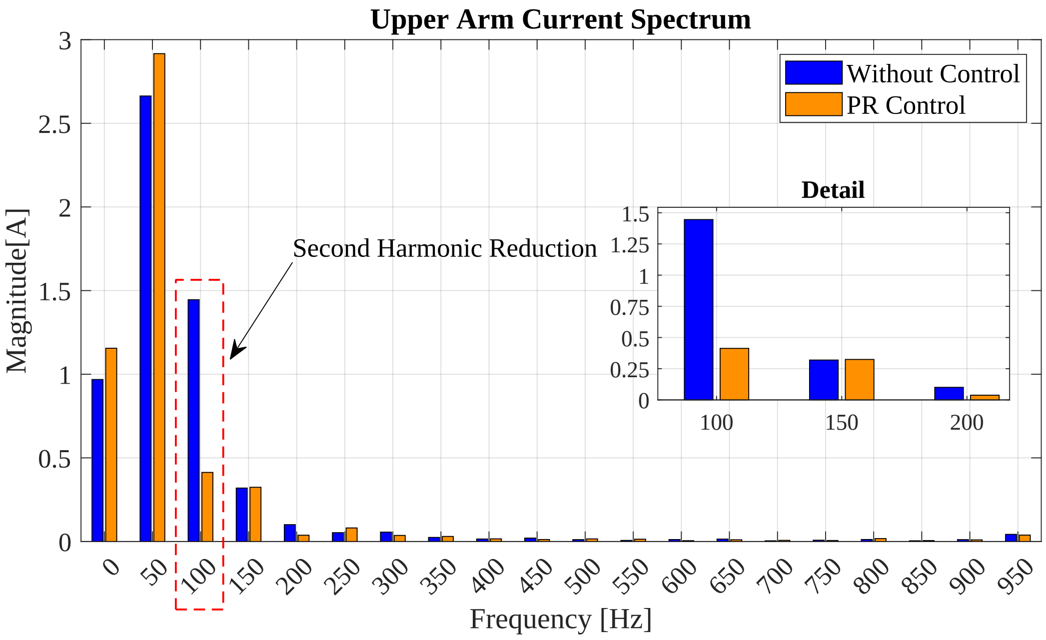

Figure 6.7: Spectrum of the upper arm current with and without the conventional PR circulating current control.

6.4 SCBI-Circulating Current Reduction

The proposed injection technique is implemented with the same test conditions carried out during the PR control tests. The injection signal gain K is tuned and configured following the treatment described in 5.3.4, thus with $K = 0.09$ to obtain the minimum circulating current. The trends of the waveforms of the output voltage, the phase current, the two arm currents, and the circulating current are shown respectively in Fig.6.8. The circulating current is reduced and the arm currents consist mainly of the fundamental harmonic component at 50Hz. By reducing the circulating current, the rms of the arm currents assume a value of approximately 4.09 A, a peak value of 7.85 A for the lower arm current, and approximately 7.24 A for the upper arm current. In Figure 6.9, the response of the SCBI technique can be analysed, which almost instantaneously reduces the circulating current. Indeed, the proposed technique provides a control action that is proportional only and therefore almost instantaneous. The only delays are caused by the digital implementation at the time of control T_c. The peak-to-peak value of the circulating current is reduced

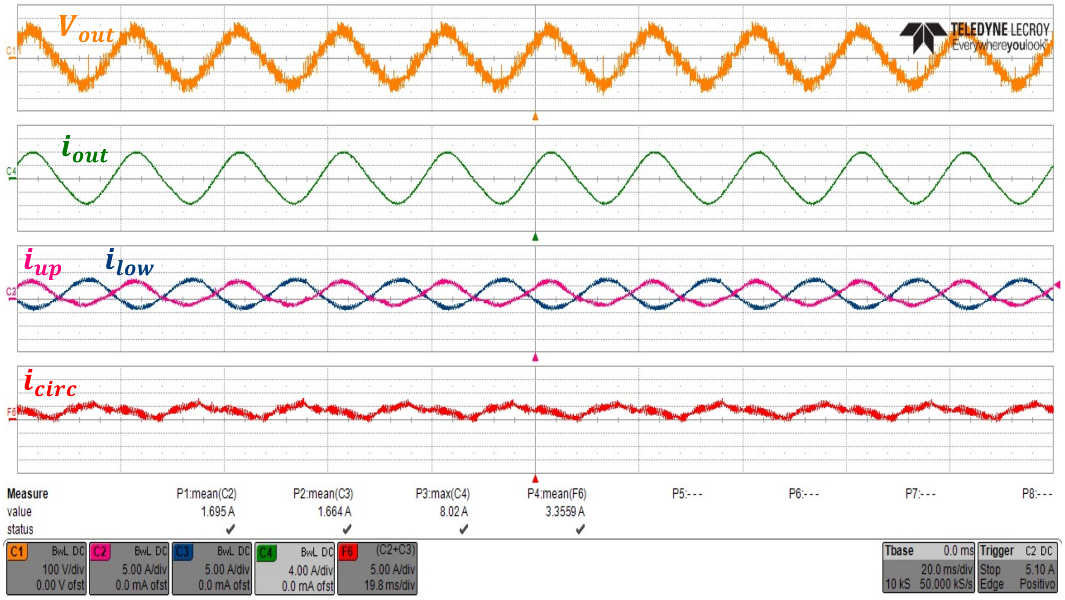

Measure	P1:mean(C2)	P2:mean(C3)	P3:max(C4)	P4:mean(F6)	P5:---	P6:---	P7:---	P8:---
value	1.695 A	1.664 A	8.02 A	3.3559 A				
status	✓	✓	✓	✓				

C1 BwL DC 100 V/div 0.00 V ofst
C2 BwL DC 5.00 A/div 0.0 mA ofst
C3 BwL DC 5.00 A/div 0.0 mA ofst
C4 BwL DC 4.00 A/div 0.0 mA ofst
F6 (C2+C3) 5.00 A/div 19.8 ms/div
Tbase 0.0 ms 20.0 ms/div 10 kS 50.000 kS/s
Trigger C2 DC Stop 5.10 A Edge Positivo

Figure 6.8: Experimental waveform of the output voltage, output current, the arm currents, and the circulating current with the SCBI active.

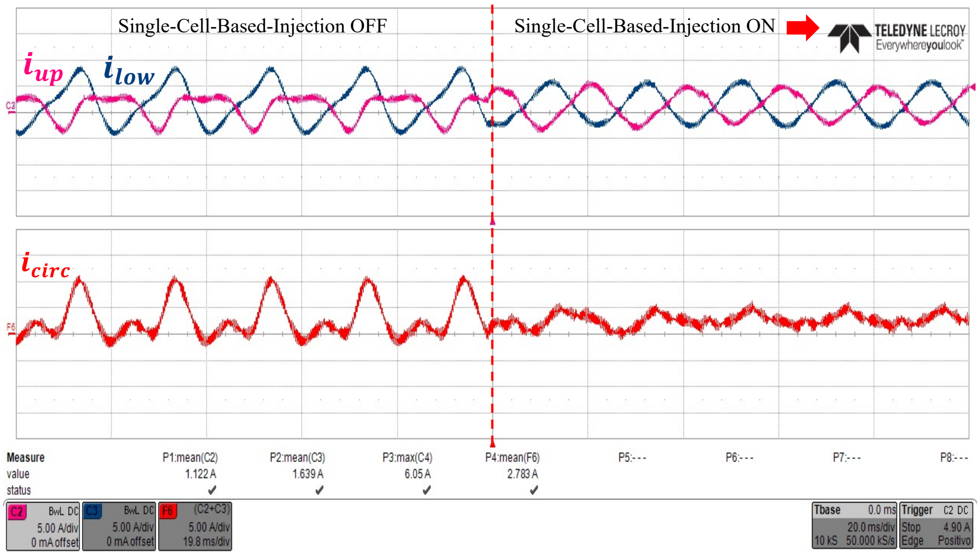

Figure 6.9: Experimental waveform of upper- and lower-arm currents and the circulating current before and after the application of the Single-Cell-Based-Injection.

by 55.41% and the rms value is 0.8 A. The two arm currents are sinusoidal and affected by a very small second harmonic component. The harmonic spectrum of the upper arm current is shown in Fig. 6.10. In particular, it is evident that the second-order harmonic component of the arm current is reduced by 88.19% and the circulating current consists mainly of its mean value, which corresponds to approximately 1.38 A.

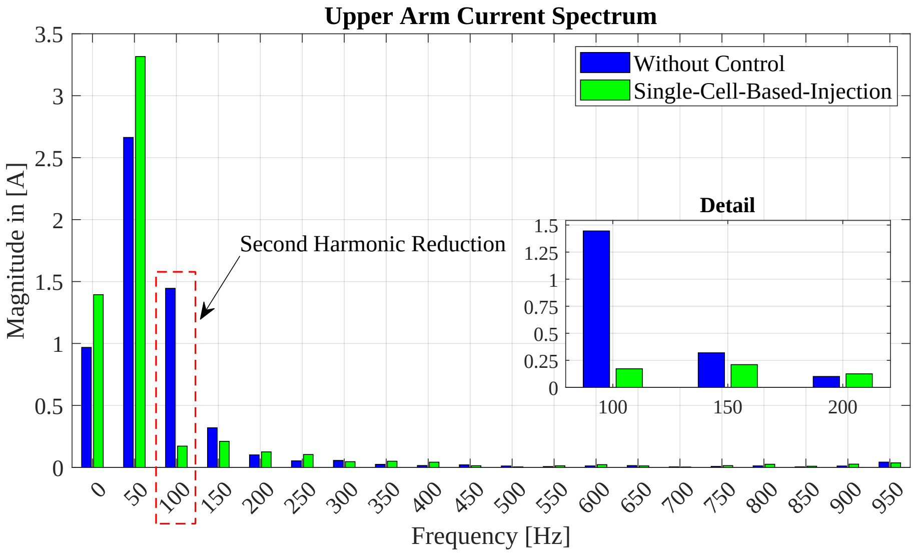

Figure 6.10: Harmonic spectrum of the upper arm current with and without the Single-Cell-Based-Injection technique.

6.5 Comparison among circulating current control

A comparison of performance between the control strategies can be defined from the waveforms obtained during the experimental tests for the conventional PR control and the proposed injection-based technique, shown in 6.5 and 6.8 respectively. The circulating current assumes a peak-to-peak value of 6 A for PR control, while it becomes 3.95 A when SCBI is active. The rms of the circulating current assumes a value of 1.4 A using PR control while when SCBI is applied the rms becomes 0.8 A. Fig. 6.11 shows the harmonic spectrum of the arm current under the three conditions: without circulating current control, with PR control, and with the proposed injection technique. The proposed technique generates a greater reduction in the second harmonic component than the conventional technique, thus increasing the efficiency of the converter. The SCBI provides better mitigation of the second harmonic current reducing the second harmonic component from $1.44A$ to $0.17A$. Indeed, it is verified that the rms value of the arm current is $5.11A$ for the case in which the PR control is implemented while it takes on a value of $4.09A$ when the SCBI is used. Between the two cases, it can be seen how, on the whole, implementing the SCBI produces arm current waveforms with reduced peak values compared to those obtained using the PR control. In particular, considering the lower arm current, a peak value of $7.85A$ is obtained, while with the PR control, a value close to $10A$ is obtained. Therefore, a greater reduction of the circulating current reduces the rms and peak value of the arm currents reducing the overall losses of the MMC.

The voltage and current output waveforms and the circulating current of the phase a of the MMC obtained for the two techniques are shown in Fig. 6.12. The calculated THD for the voltage output results are very similar in both cases of about 20%. The Weighted Total Harmonic Distortion for the output voltage is around 2.35% for both techniques.

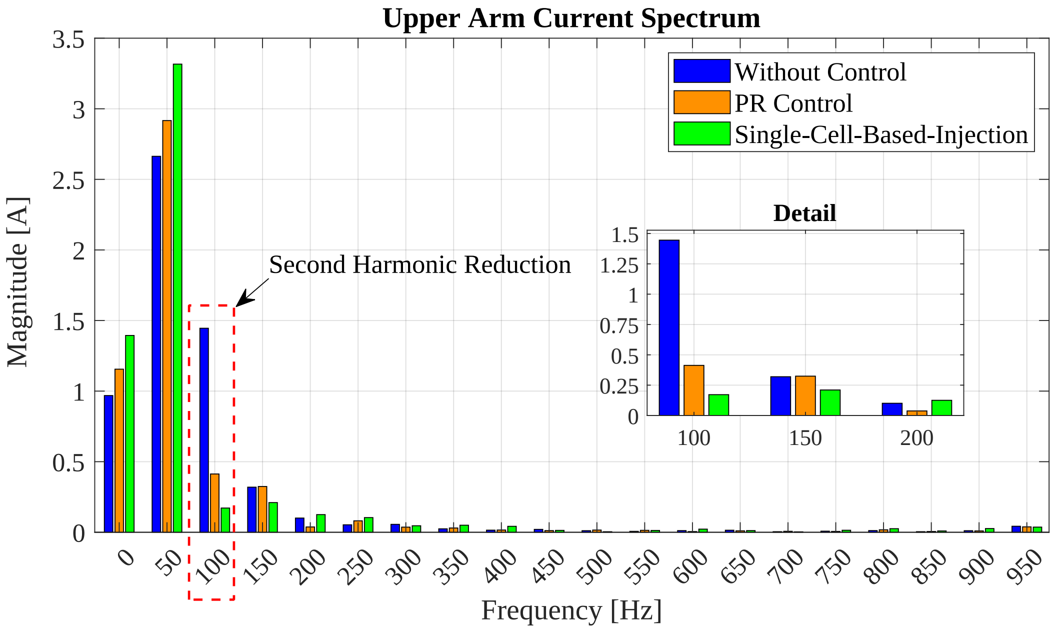

Figure 6.11: Harmonic spectrum of the upper arm current in three different cases: without any control, with PR Control, and SCBI method.

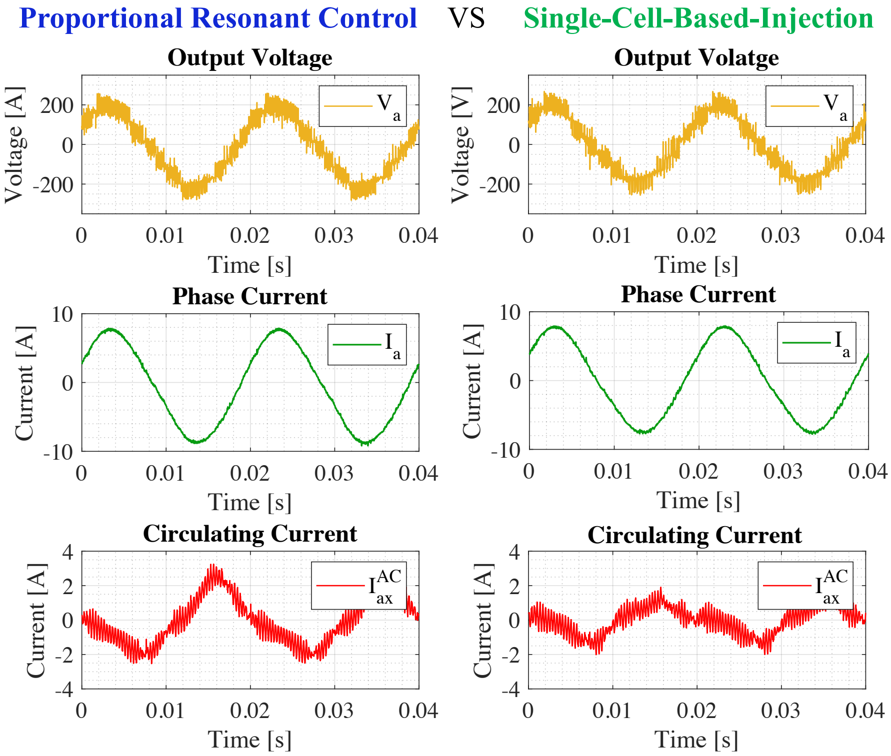

Figure 6.12: Voltage, current, and circulating current in comparison between the PR circulating control and Single-Cell-Based-Injection method.

From the analysis of the circular interactions proposed in Chapter 5, it can be seen that there is a close relationship between the circulating current and the voltage ripple. A reduction in the circulating current also causes a reduction in the voltage ripple across the capacitors of the sub-modules of the MMC. Figures 6.13 and 6.14 show the trends of the voltage ripple of the SMs' capacitors before and after the effects of the reduction of the circulating current. In this case, the difference in

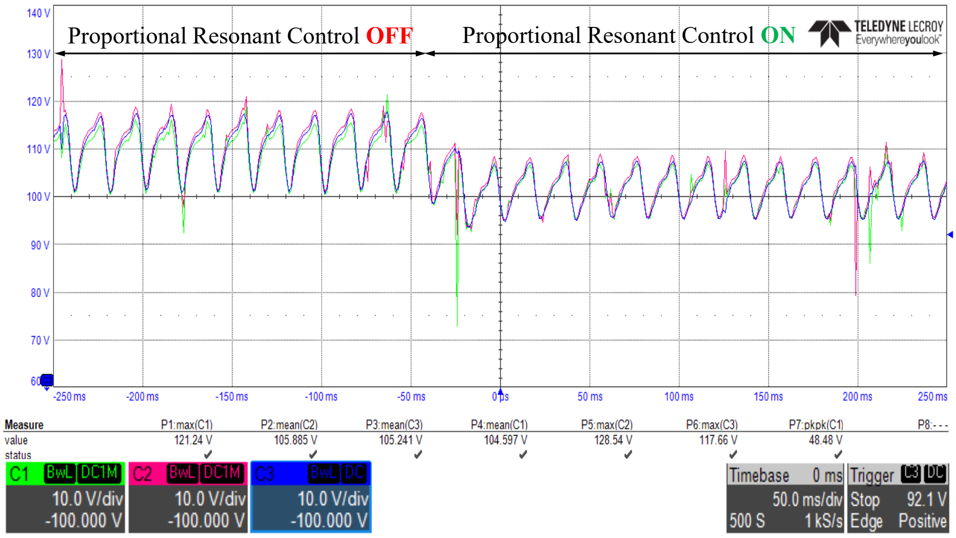

Measure	P1:max(C1)	P2:mean(C2)	P3:mean(C3)	P4:mean(C1)	P5:max(C2)	P6:max(C3)	P7:pkpk(C1)	P8:- - -
value	121.24 V	105.885 V	105.241 V	104.597 V	128.54 V	117.66 V	48.48 V	
status	✓	✓	✓	✓	✓	✓	✓	

C1 BwL DC1M 10.0 V/div -100.000 V
C2 BwL DC1M 10.0 V/div -100.000 V
C3 BwL DC 10.0 V/div -100.000 V
Timebase 0 ms 50.0 ms/div 500 S 1 kS/s
Trigger C3 DC Stop 92.1 V Edge Positive

Figure 6.13: Experimental waveform of the capacitor voltages of the upper arm before and after the action of PR circulating current control.

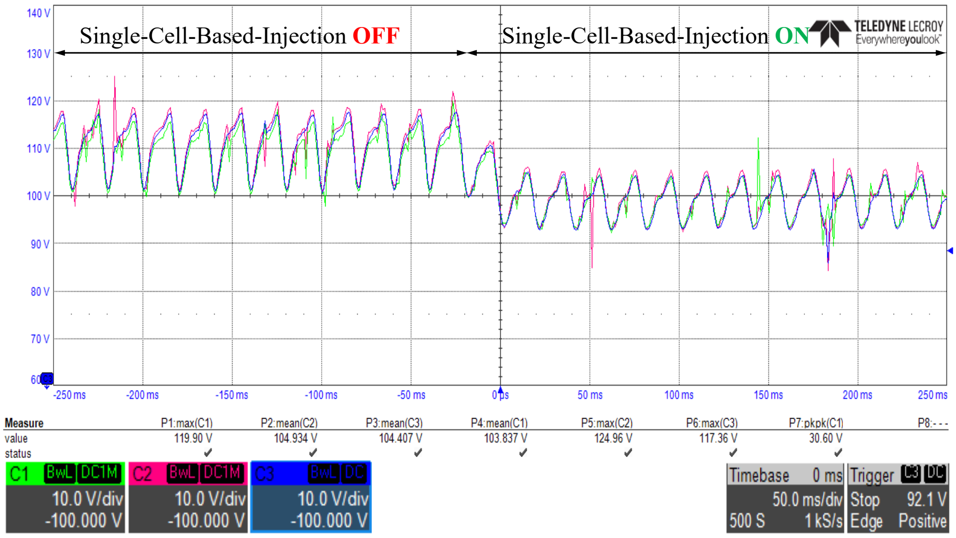

Measure	P1:max(C1)	P2:mean(C2)	P3:mean(C3)	P4:mean(C1)	P5:max(C2)	P6:max(C3)	P7:pkpk(C1)	P8:- - -
value	119.90 V	104.934 V	104.407 V	103.837 V	124.96 V	117.36 V	30.60 V	
status	✓	✓	✓	✓	✓	✓	✓	

C1 BwL DC1M 10.0 V/div -100.000 V
C2 BwL DC1M 10.0 V/div -100.000 V
C3 BwL DC 10.0 V/div -100.000 V
Timebase 0 ms 50.0 ms/div 500 S 1 kS/s
Trigger C3 DC Stop 92.1 V Edge Positive

Figure 6.14: Experimental waveform of the capacitor voltages of the upper arm before and after the action of SCBI method whit gain $K = 0.09$.

terms of voltage ripple between the two techniques, PR control, and SCBI, is not very evident, but there is nevertheless a slightly greater reduction in the voltage ripple for the SCBI method in which the circulating current is more reduced. Once the PR control is applied, the voltage ripple becomes about 6.2% while when the SCBI technique is active the ripple becomes 5.7% as shown by the detail proposed in the Fig 6.15. Fig. 6.16 shows a comparison of conduction and switching losses in the MMC submodules in three different cases: without any circulating current control, with conventional PR control, and with the proposed SCBI technique. The bar graph provides a detailed breakdown of the losses for each submodule of the upper arm of phase a. In the case of SCBI, injection is performed on SM1. Both control techniques achieve a notable reduction of the submodule losses, approximately 50% concerning the uncontrolled case. It is worth noticing that, despite the injection being performed only on a single submodule, no difference is found in terms of increased losses between the submodule where the injection is applied and those without injection, indicating that oversizing of the submodule is not necessary when the proposed SCBI method is used. Conduction losses only depend on the RMS value of the arm current, which is the same for all the submodules. Furthermore, switching losses are made even across submodules when a control strategy

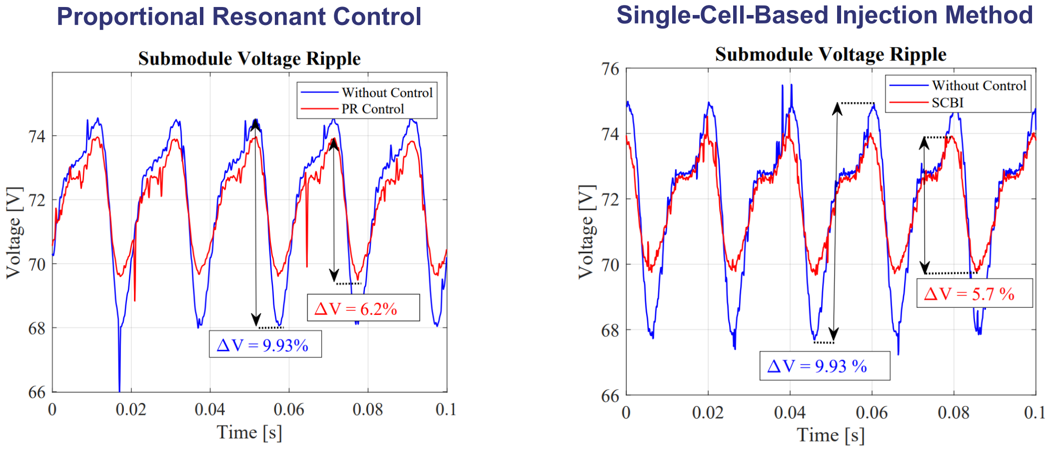

Figure 6.15: Comparison of the submodule voltage ripple between conventional PR control and SCBI method.

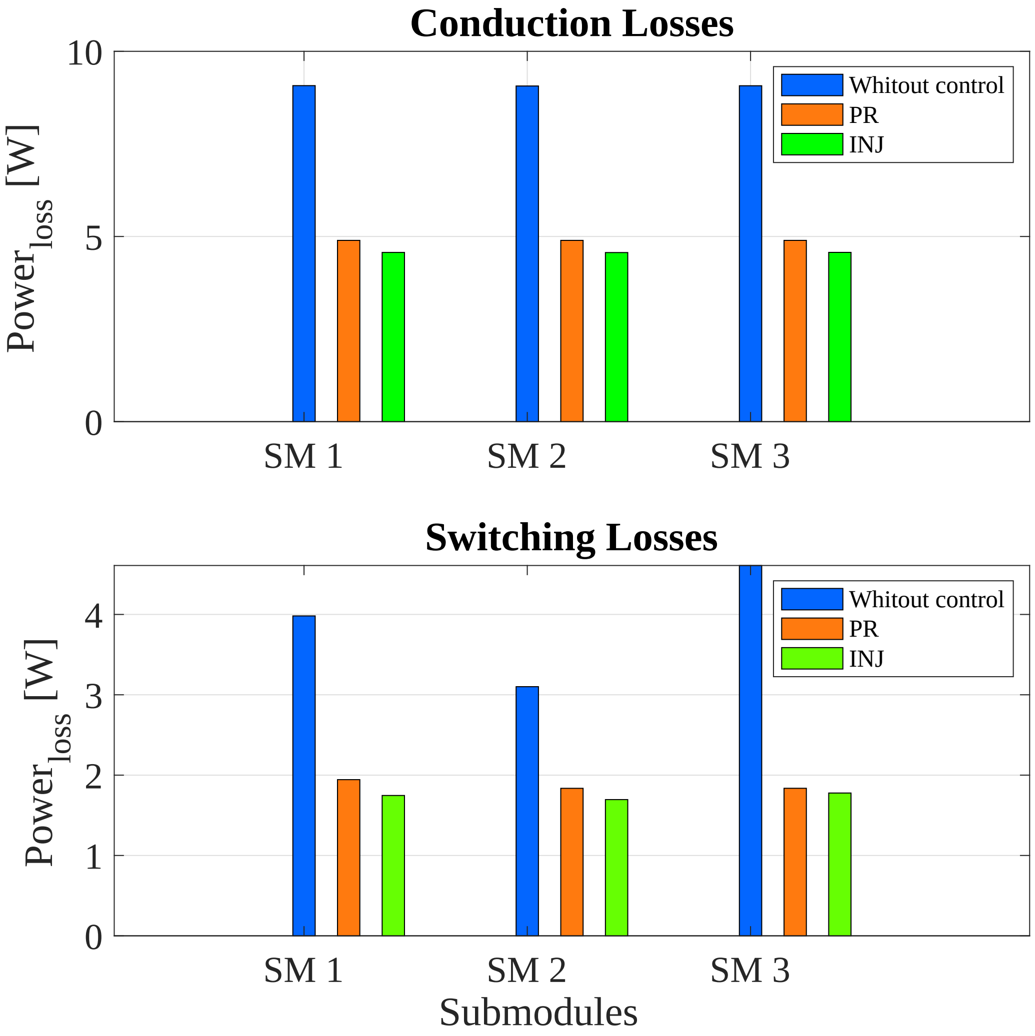

Figure 6.16: Histogram of conduction and switching losses for each submodlues of the upper arm in three different cases.

is employed. In Fig. 6.17 are presented the efficiencies calculated by the YOKOGAWA waveform analyzer for the two techniques with P_{in} and P_{out} being the input and output powers, respectively. The efficiency obtained from the conventional PR control is $94,147\%$, while that obtained by applying the proposed SCBI technique is $94,315\%$. The higher efficiency obtained, the good performance, and the simplicity of implementation validate the technique proposed in this thesis work. The table 6.2 shows the summary of all results obtained during the experimental test.

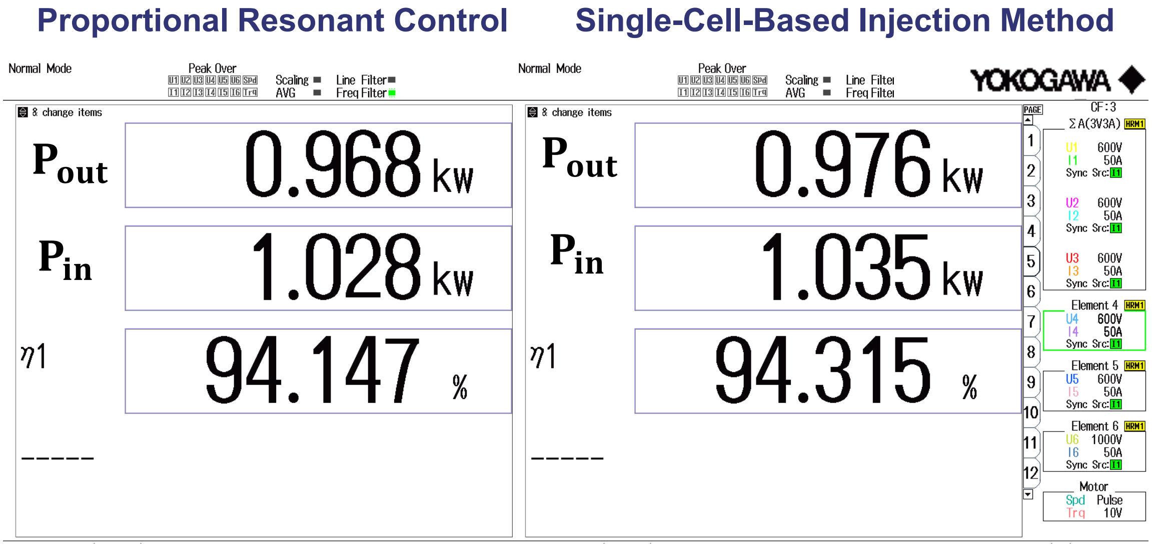
Proportional Resonant Control

Single-Cell-Based Injection Method

P_{out} 0.968 kW

P_{in} 1.028 kW

$\eta1$ 94.147 %

P_{out} 0.976 kW

P_{in} 1.035 kW

$\eta1$ 94.315 %

Figure 6.17: Efficiencies of the two techniques in comparison: On the left is shown the efficiency related to the conventional PR control; on the right is shown the efficiency related to the SCBI technique proposed in this thesis work.

Table 6.2: Comparison between PR Control and Proposed Single Cell Based Method.

Indicator	PR Control	SCBI Method
Circ. Current (Peak-Peak Value)	5.74 A	3.95 A
Circ. Current (Peak Value)	3.28 A	1.86 A
Circ. Current (Root-Mean-Square)	1.4 A	0.8 A
Voltage Ripple	6.2 %	5.7 %
Efficiency	94.14 %	94.31%

Chapter 7

Single-Cell-Based-Injection Method for Voltage Balancing

The technique implemented in this thesis work is initially designed to pursue as the first objective the elimination of circulating current and as the indirect effect the reduction of the voltage ripple of the capacitors of the SMs by reducing the overall power losses of the converter. However, in this chapter the Single-Cell-Based-Injection technique has been extended to be able to carry out another control objective i.e., balancing the voltages of the capacitors of the submodules. The proposed technique is implemented to simultaneously achieve three control objectives, such as circulating current reduction, capacitor voltage ripple minimization, and voltage balancing. A selection mechanism of the SMs on which to perform the signal injection is added to the technique proposed in the previous chapters.

The injection signal is applied to one submodule at a time in an alternating manner for each control period, performing a rotation of injection among the various submodules belonging to the same arm, to realize, as an additional goal, the balancing of capacitor voltages. The selected submodule is then driven by a modulating signal containing the injection that is properly implemented will be able not only to reduce the circulating current, and the voltage ripple, but it will also vary the amount of charge in the capacitor of the SM that will charge/discharge differently from the remaining SMs and thus applying a ”rotation ” of the injection signal among the various SMs, one at a time, will achieve voltage balancing.

This technique is part of the category of voltage balancing techniques with sensors, described in 4.2.1, with the difference that this technique is implemented outside the modulator, indeed the injection of a signal proportional to the circulating current for a submodule per arm of the MMC is implemented before the comparison between the modulating signal and the carrier. In this way, the proposed voltage balancing technique maintains the switching frequency of the devices constant at the design value. This provides greater control over losses and device stress, unlike balancing techniques based on sorting algorithms or those implemented at the modulator level, which vary the frequency of the devices during their operation. This chapter will describe, the proposed technique and the mechanism for selecting the SMs on which to apply injection to generate the MMC voltage balancing. The modulation strategy used is phase-shifted carrier pulse width modulation (PSC-PWM).

7.1 Selection Mechanism for SMs

The injection signal rotation criterion to be applied to the submodules of each arm in an alternating manner is identified based on the equation related to the change in capacitor voltage shown below.

$$v_{c_{SM}} = \frac{V_{dc}}{N} + \frac{1}{C}\int_{t_0}^{t_0+\Delta t} S_{xy} i_{xy} dt = \frac{V_{dc}}{N} + \Delta v_{c_{SM}} \tag{7.1}$$

where $v_{c_{SM}}$ is the instantaneous voltage across the capacitors of the submodule and is denoted by S_{xy} and i_{xy} the generic switching function and arm current of phase x and arm y, respectively. $\Delta v_{c_{SM}}$ is the voltage variation of the capacitance of the individual submodule. It can be seen from the equation 7.1 that by appropriately changing the switching function, the voltage variation of the submodule of the MMC can be changed. Recall that in the presence of the injection signal, the switching function becomes:

$$S_{xju,l} = \frac{1}{2} \mp \frac{1}{2} m \sin(\omega t + \theta x) + K i_{xz} \tag{7.2}$$

Substituting the expression 7.2 into the equation gives the following expression:

$$v_{c_{SM}} = \frac{V_{dc}}{N} + \frac{1}{C} \int_{t_0}^{t_0+\Delta t} \{[\frac{1}{2} \mp \frac{1}{2} m \sin(\omega t + \theta x)] i_{xy} + K i_{xz} i_{xy}\} dt \tag{7.3}$$

from which the following terms can be identified:

$$v_{c_{SM}} = \frac{V_{dc}}{N} + \Delta v_{c_{SM}} + \Delta v_{c_{SMJ}} \tag{7.4}$$

the term $\Delta v_{c_{SMJ}}$ is the amount of charge generated by the injection signal implemented in that submodule. The expression of which is as follows:

$$\Delta v_{c_{SMJ}} = \int_{t_0}^{t_0+\Delta t} K i_{xz} i_{xy} dt \tag{7.5}$$

The effect of the injection is the appearance of an additional term in the expression of the voltage change of the submodule capacitor that results in an increase or decrease in voltage depending on the sign of the product of the arm current by the circulating current. If both the arm and circulating currents have concordant signs then $\Delta v_{c_{SMJ}}$ results in a positive contribution to the voltage variation; conversely, if the two electrical quantities have a discordant sign, $\Delta v_{c_{SMJ}}$ results in a negative contribution to the voltage variation. The table 7.1 shows the four possible cases that change the charge of the capacitor.

Table 7.1: Capacitor charge/discharge mechanism.

Arm current i_{xy}	Circulating Current i_{xz}	$\Delta v_{c_{SMJ}}$
+	+	+
+	-	-
-	+	-
-	-	+

7.2 Proposed Voltage Balance Injection Method

The implementation of the Single-Cell-Based-Injection technique is very simple as described in Chapter 5 and its extension to contribute to balancing is easy to implement since it consists essentially in determining in which submodule per arm to inject the signal. Therefore, considering the contributions that the injected signal gives to the variation of the capacitor voltages, the technique is implemented by following the following steps:

Step 1 For each control period, capacitor voltages, currents of both arms are measured and their sign is identified.

Step 2 The estimate of the dc current flowing in the phases of the MMC is derived by the equation 5.1 and then subtracted from the circulating current so as to obtain the only part of the alternating circulating current i_{xz}^{AC}.

Step 3 Once the following quantities have been obtained, the selection mechanism can be applied. When the generic arm current i_{xy} and the circulating current i_{xz}^{AC} have concordant sign the injection into the reference of the submodule with the lower voltage is applied. This signal will be applied for the submodule to have the desired voltage level.

Step 4 If i_{xy} and i_{xz}^{AC} have discordant sign, injection is made into the reference of the submodule with higher voltage in order to ease its discharging.

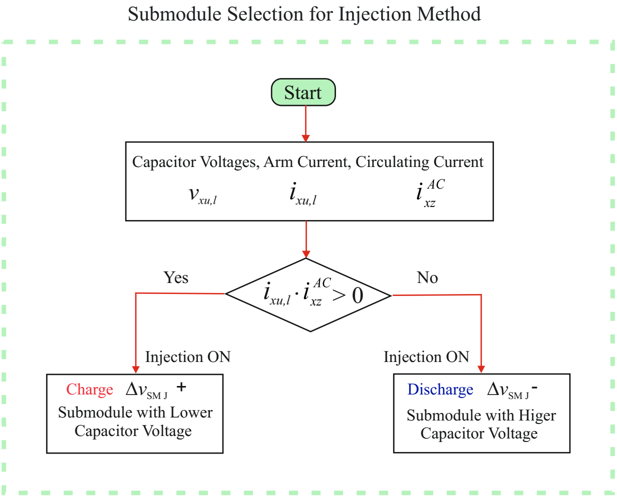

Figure 7.1: Simplified flow chart of submodule selection for injection method.

A simplified flow chart of the previous steps for the submodule selection for the injection method is show in Fig. 7.1, and the block diagram of the proposed Single-Cell-Based-Injection voltage balance method is show in Fig. 7.2. However, it is important to point out that the value and tuning of injection gain K will depend on the desired performance objectives, including reducing both circulating current and capacitor voltage ripple and balancing submodule capacitors. Indeed, the gain

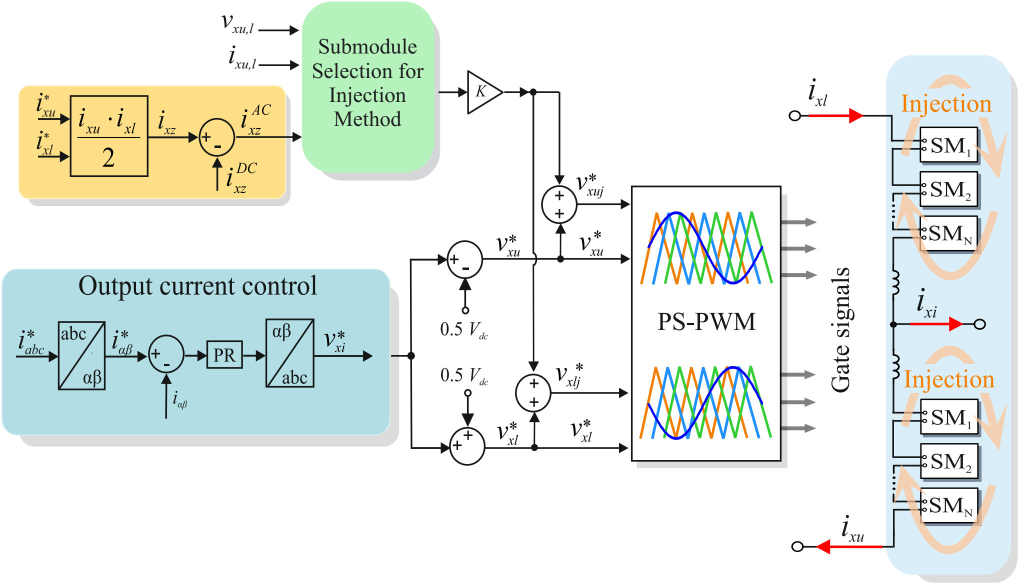

Figure 7.2: Simplified block diagram of the proposed voltage balance injection scheme.

K multiplied by the measured circulating current constitutes the injection signal as described previously. An additional important aspect concerns the influence of gain K and the effect that injection has on the balancing speed of capacitor voltages, as shown in Fig. 7.3. In this graph, the time required to balance the submodule voltages decreases as the K-gain increases until the value $K = 0.09$, at where we get the reverse circulating current condition, which generates a distortion on the submodule capacitance voltages, delaying balancing as in the case where $K = 0.1$. Actually, as K increases, there will be an injection action whereby the circulating current and voltage ripple decrease, and consequently the time required to achieve balancing decreases. From the expressions derived in chapter 5, the capacitor current is defined as the product of the average switching function and the arm current, the extended formula for which is shown in A.1 for the upper-arm submodules and the equation A.2 for the submodules belonging to the lower arm. It is possible to define the power of the submodule from the voltage of the submodule capacitor and the current flowing in the capacitance. Multiplying the voltage across the submodule capacitor by the current flowing through the capacitor, the power generated by the submodule can be determined. This calculation allows the energy stored in the

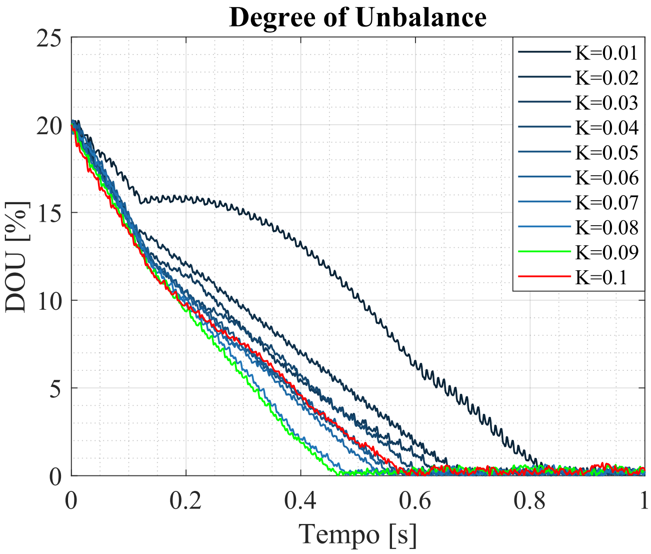

Figure 7.3: Variation of balancing time as gain changes K when the DOU is 20 %.

capacitance E_{SM} to be defined by the following equations.

$$E_{SM} = \int_{t_0}^{t_0+\Delta t} \underbrace{(\frac{V_{dc}}{N} + \Delta v_{c_{SM}})i_{c_{SM}}}_{Power} dt \tag{7.6}$$

$$E_{SM_{inj}} = \int_{t_0}^{t_0+\Delta t} \underbrace{(\frac{V_{dc}}{N} + \Delta v_{c_{SM}} + \Delta v_{c_{SMJ}})i_{c_{SM}}}_{Power} dt \tag{7.7}$$

The equation 7.7 describes the energy stored in the submodule when the injection signal is applied. The Fig. 7.4 shows the difference in energy stored in the submodule capacitor both when the injection signal is applied and when it is not applied.

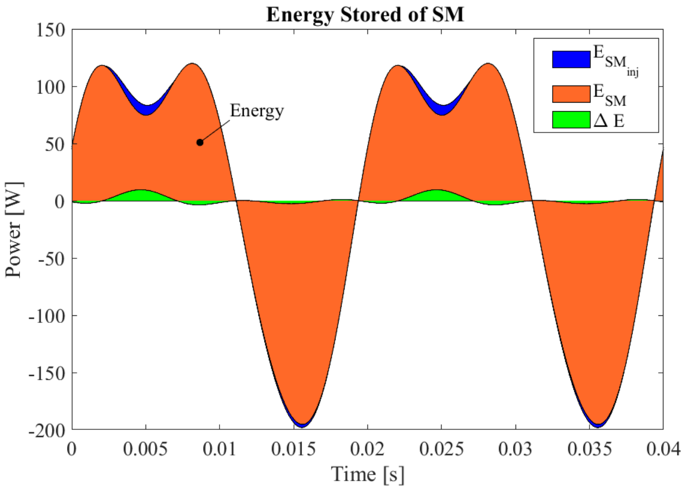

Figure 7.4: Comparison of the power and energy stored by the submodule capacitor both when the injection signal is applied and without.

7.3 Experimental results

In this section, results are presented regarding the power tests performed on the experimental setup to validate the proposed technique and to compare the performance of the Single-Cell-Based-Injection technique with the conventional capacitor voltage balancing technique proposed in [65]. In order to be able to evaluate the performance of the technique in terms of capacitor voltage balancing, an index is introduced that quantifies the level of unbalance of the voltages of the submodules belonging to the same arm, referred to in this thesis work as Degree Of Unbalance (DOU), calculated as follows:

$$DOU_{xy} = \frac{max(v_{cxy_{SM})} - min(v_{cxy_{SM}})}{V_c} * 100 \tag{7.8}$$

where DOU_{xy} is the degree of unbalance (DOU) of the generic phase x and arm y, while $v_{cxy_{SM}}$ is the voltage value of the generic submodule belonging to phase x and arm y. V_c is reference value for the capacitor voltage of the submodules equal to $\frac{V_{dc}}{N}$ with V_{dc} the dc-bus voltage and N the number of SMs of the MMC arm. Various tests were performed as the DOU varied so that the performance of the proposed technique in terms of voltage balancing could be analyzed.

7.3.1 Conventional Voltage Balance Algorithm

Initial tests are conducted by implementing the voltage balancing described in [65] for different DOUs 20%, 30% and 40%, the DC voltage is set equal to 300 V, a modulation index is set to $m = 0.8$, a phase current equal to 4 A imposed by the phase current control implemented. The switching frequency of the devices is 1kHz. In Figures 7.5, 7.6, and 7.7 the waveforms of the upper arm capacitance voltages are shown. It can be seen from the graphs that once this balancing algorithm is applied, the voltages are almost instantaneously brought to their reference value of $V_c = 100V$. In order to obtain balanced voltages, this technique modifies the insertion instant and duration of each submodule according to the sign of the arm currents so that the charging and discharging of the capacitors of the SMs can be varied. This algorithm is based on the acquisition of the insertion index generated by the implemented modulation strategy therefore it is a method implemented at the modulator level. However, although it has excellent dynamic performance, contradistinct from short transients it generates an undesirable effect on the switching frequency of all the submodules. In particular, it occurs that the SMs are inserted repeatedly in a variable manner causing the devices to switch at a switching frequency fc, varying from a range of $fc - Nfc$. There are several papers in the literature that analyze the impact of voltage balance control on the switching frequency [79]. This effect is quite evident from the graphs shown in Figures 7.5, 7.6, and 7.7, as soon as the balancing technique is active, the submodules switch to a higher switching frequency, which increase the power losses of the MMC.

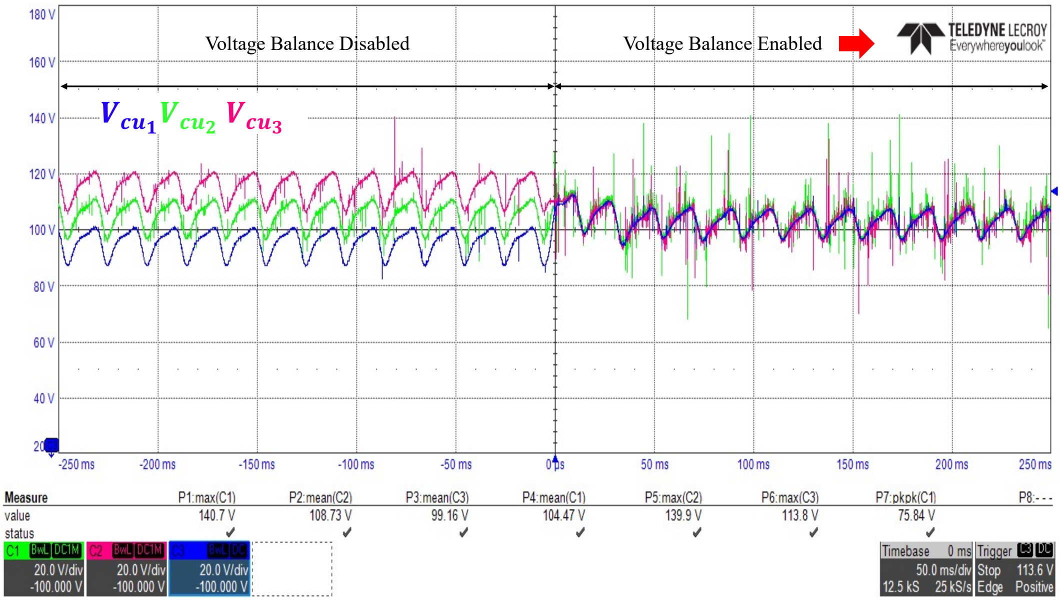

Figure 7.5: Voltage across of the submodule capacitors before and after activating the voltage balancing strategy with a DOU of 20%

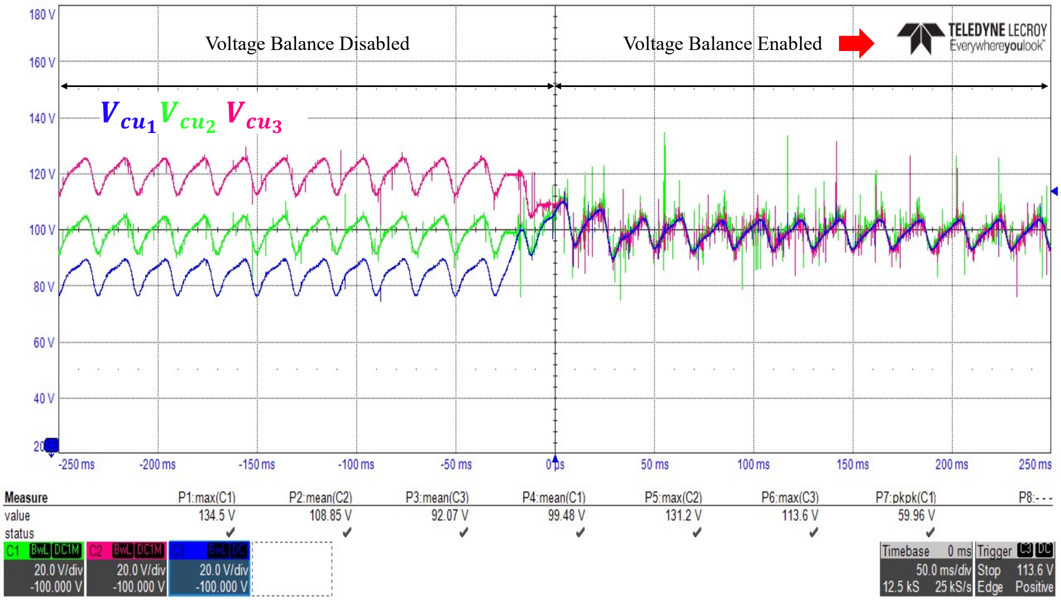

Figure 7.6: Voltage across of the submodule capacitors before and after activating the voltage balancing strategy with a DOU of 30%

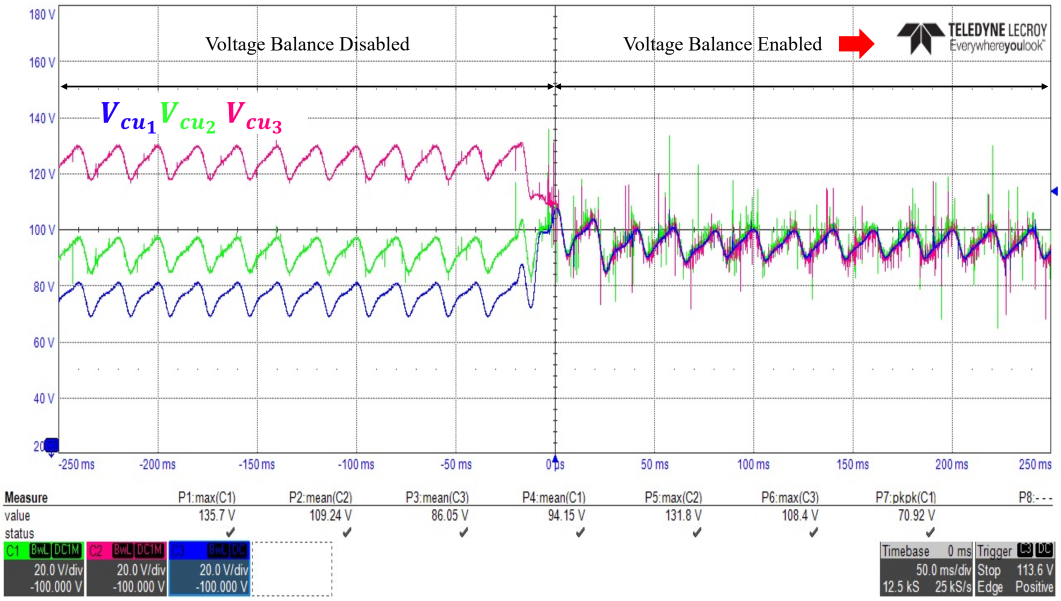

Figure 7.7: Voltage across the submodule capacitors before and after activating the voltage balancing strategy with a DOU of 40%

7.3.2 SCBI-Voltage Balance

This section shows the experimental results obtained by implementing the proposed balancing technique. The tests are performed by setting the same power and switching frequency used for the tests carried out by implementing the conventional balancing technique. The proposed technique is tested for three different DOU 20%, 30% and 40% so that the performance of the proposed balancing strategy could be validated. The injection signal gain K is chosen to achieve not only voltage balancing but also maximum circulating current reduction and thus set $K = 0.09$. The waveforms of the voltages of the upper arm capacitors are shown in Figures 7.8,7.9, 7.10. Unlike the previously described technique, this voltage balance method is implemented outside the modulator which avoids varying the switching frequency of the devices. For the different DOUs used, it can be seen that the proposed technique exhibits a transient from when it is applied to when the balancing of the voltages of the SMs is then ensured. In particular, it can be seen that with a DOU equal to 20% the transient has a duration of about 500 ms, with a DOU equal to 30% the transient is about 1s while when the DOU has been extremized to 40% the transient lasts longer and is about 1.5 s. Although this technique has slower dynamics the balancing times are still short and also it must be remembered that when the proposed technique is active at the same time the circulating current and voltage ripple of the capacitors of the SMs are reduced. The voltage ripple is reduced from a value of 13% to one of 10% when the injection method is active. The ripple turns out to be quite high due to capacitor capacitances that have a small value, $C = 500\mu$ F. Actually, low capacitance values generate higher voltage fluctuations that make the control of the MMC more difficult. However, the implemented technique reduces the voltage ripple by about 3%.

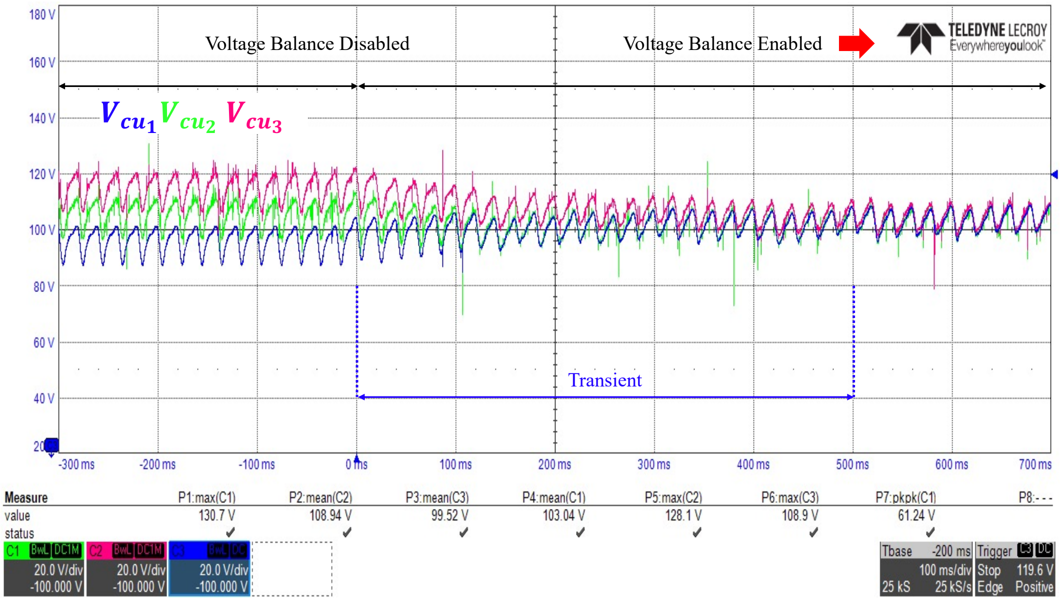

Figure 7.8: The experimental waveforms of the voltage at the ends of the submodule capacitors before and after activating the SCBI voltage balancing strategy with a DOU of 20%

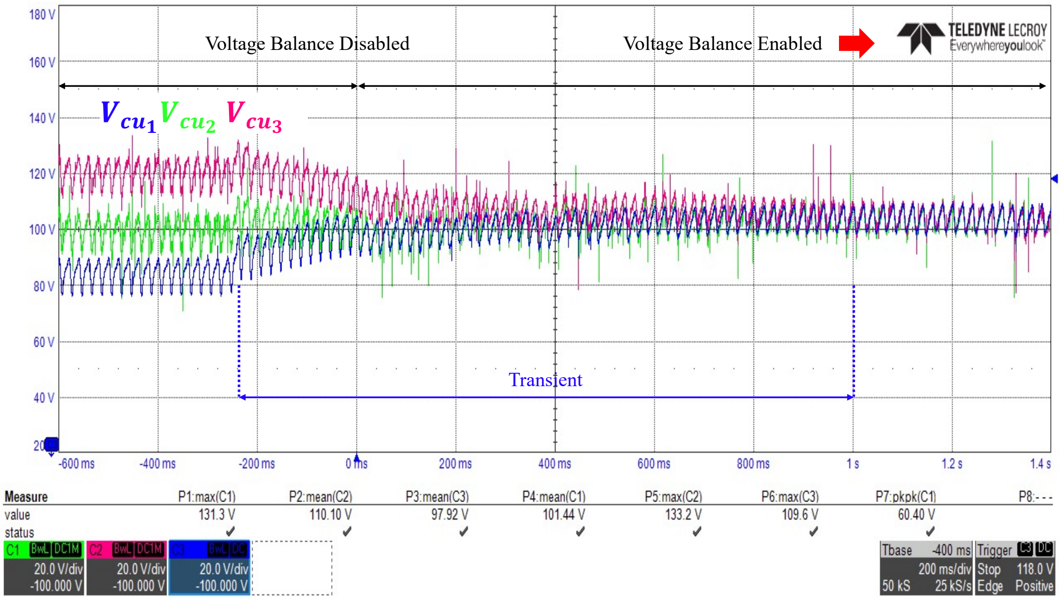

Figure 7.9: The experimental waveforms of the voltage at the ends of the submodule capacitors before and after activating the SCBI voltage balancing strategy with a DOU of 30%

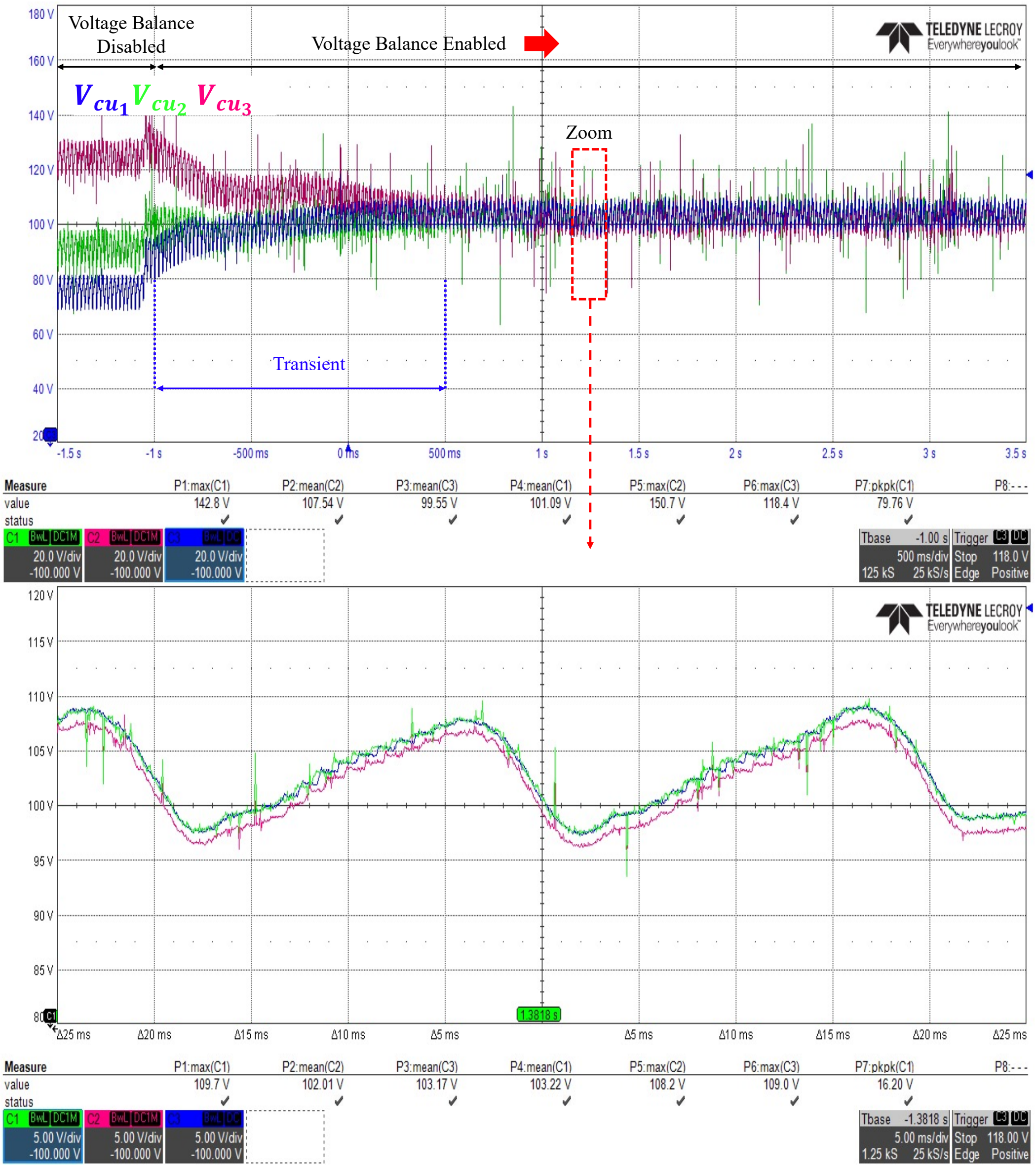

Figure 7.10: The experimental waveforms of the voltage at the ends of the sub-module capacitors before and after activating the SCBI voltage balancing strategy with a DOU of 40%. The graph below shows the zoom of the voltages at time 1.38 seconds.

In Fig. 7.11 are presented the efficiencies calculated by the YOKOGAWA power analyzer for the two techniques with P_{in} and P_{out} being the input and output powers, respectively. The efficiency obtained from the conventional voltage balance strategy is $94,06\%$, while that obtained by implementing the proposed SCBI technique is $95,30\%$. The higher efficiency obtained and the good performance validate the technique proposed in this thesis work.

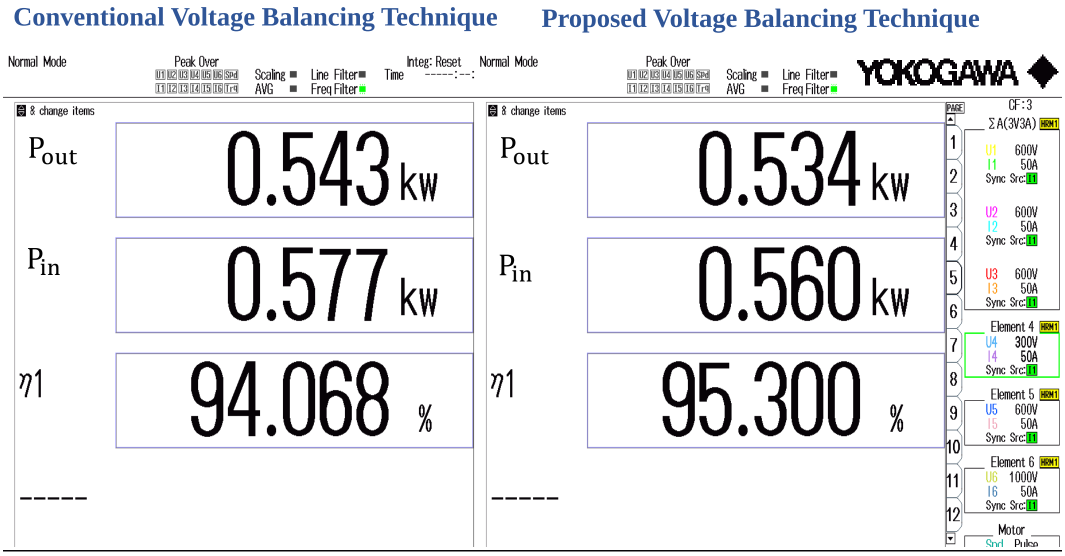
Conventional Voltage Balancing Technique

P_{out} 0.543 kW

P_{in} 0.577 kW

η1 94.068 %

Proposed Voltage Balancing Technique

P_{out} 0.534 kW

P_{in} 0.560 kW

η1 95.300 %

Figure 7.11: Efficiencies of the two techniques in comparison: On the left is shown the performance related to the conventional balancing strategy proposed in [65], on the right is shown the performance related to the proposed balancing strategy in this thesis work.

Chapter 8

Conclusions and Discussion

In this thesis, a novel method for suppressing the ac components of the circulating current in multilevel modular converters is proposed, based on the injection of a signal proportional to the circulating current itself into a single submodule of each converter arm. In addition, an analytical model of the electrical quantities governing the internal and external dynamics of the multilevel modular converter is provided. This analytical model is useful in determining the calibration guidelines for the proposed innovative control. Experimental tests were performed on a laboratory prototype to evaluate the effectiveness of the proposed injection method, showing that the technique effectively dampens the circulating current and reduces the ripple of the submodule capacitor voltage, improving the overall performance of the converter. The results also indicate that the proposed approach mitigates the overall losses of the converter by reducing the RMS value of the arm currents without requiring over-sizing of the compensation submodule or downgrading of the converter operation. In the end, an extension of the technique is also proposed so that the capacitor voltage of the submodules of the MMC can also be balanced through the implemented injection signal. The results show that the proposed method succeeds in effectively balancing the submodule voltages under different initial unbalanced conditions.

8.1 Outlook

The proposed technique has been experimentally validated and is suitable for circulating current reduction, ripple reduction, and submodule voltage balancing. The method is characterized by a simple approach that is easy to implement, and the guidelines for adjusting the signal to be injected have been obtained and validated with the experimental results.

Therefore, this thesis opens up the possibility for several insights, which can be summarized as follows.

- Conduct a thermal analysis by studying the effect that the injection signal has on the current flowing inside the capacitor.
- Analyze the scalability of the method using a MMC with a number of SMs greater than three.
- Benchmark with another injection technique that aims to reduce the circulating current.
- Experimentally validate the proposed voltage-balancing technique with another technique proposed in the literature that implanted the control of voltage balancing outside the modulator.
- The proposed voltage balancing method is mainly based on acquiring the instantaneous vaolors of voltages and the sign of arm currents, it may have lower performance for low values of current and voltage. Indeed, it may be difficult in noisy conditions and in regions close to the zero crossing. Although most of the commercially available MMCs that are already implemented in industrilai applications operate in MVDC, it is necessary to improve the technique in order to be able to offer the possibility of being allowed to estimate currents and tesnions in the case of high measurement noise.

Appendix A

Appendix

The analytical expressions of the electrical quantities are given in this appendix in their extended form.

A.1 Capacitor Current Ripple

The capacitor current is generated by the arm current through the switching actions. Consequently, the average ripple current of the capacitor can be described as the product of the average switching function and the arm current, as expressed in the following equations:

Without Injection

$$
\begin{aligned}
i_{Cxu} = & \underbrace{\frac{I_{xz}^{DC}}{2} - \frac{mI}{8}\cos(\phi)}_{dc-component} \underbrace{+\frac{I}{4}\sin(\omega t+\phi) - \frac{mI_{xz,2}}{4}\cos(\omega t+\Phi_{xz,2}) - \frac{mI_{xz}^{DC}}{2}\sin(\omega t)}_{fundamental-component} \\
& \underbrace{+\frac{I_{xz,2}}{2}\sin(2\omega t+\Phi_{xz,2}) + \frac{mI}{8}\cos(2\omega t+\phi)}_{2nd-component} \\
& \underbrace{+\frac{mI_{xz,2}}{4}\sin(3\omega t+\Phi_{xz,2})}_{3rd-component}
\end{aligned}
\tag{A.1}
$$

$$\begin{aligned} i_{Cxl} = & \underbrace{\frac{I_{xz}^{DC}}{2} - \frac{mI}{8}\cos(\phi)}_{dc-component} \underbrace{-\frac{I}{4}\sin(\omega t+\phi) + \frac{mI_{xz,2}}{4}\cos(\omega t+\Phi_{xz,2}) + \frac{mI_{xz}^{DC}}{2}\sin(\omega t)}_{fundamental-component} \\ & \underbrace{+\frac{I_{xz,2}}{2}\sin(2\omega t+\Phi_{xz,2}) + \frac{mI}{8}\cos(2\omega t+\phi)}_{2nd-component} \\ & \underbrace{-\frac{mI_{xz,2}}{4}\sin(3\omega t+\Phi_{xz,2})}_{3rd-component} \end{aligned} \tag{A.2}$$

With Injection

$$\begin{aligned} i_{Cxu_J} = & \underbrace{\frac{I_{xz}^{DC}}{2} + \frac{KI_{xz,2}}{4}\cos(\beta+\Phi_{xz,2}) - \frac{mI}{8}\cos(\phi)}_{dc-component} \\ & \underbrace{+\frac{I}{4}\sin(\omega t+\phi) - \frac{mI_{xz,2}}{4}\cos(\omega t+\Phi_{xz,2}) - \frac{mI_{xz}^{DC}}{2}\sin(\omega t) + \frac{KI}{8}\cos(\omega t+\beta-\phi)}_{fundamental-component} \\ & \underbrace{+\frac{I_{xz,2}}{2}\sin(2\omega t+\Phi_{xz,2}) + \frac{mI}{8}\cos(2\omega t+\phi) + \frac{KI_{xz}^{DC}}{2}\sin(2\omega t+\beta)}_{2nd-component} \\ & \underbrace{+\frac{mI_{xz,2}}{4}\sin(3\omega t+\Phi_{xz,2}) - \frac{KI}{8}\cos(3\omega t+\beta+\phi)}_{3rd-component} \\ & \underbrace{-\frac{KI_{xz,2}}{4}\cos(4\omega t+\beta+\Phi_{xz,2})}_{4th-component} \end{aligned} \tag{A.3}$$

$$
\begin{aligned}
i_{Cxl_J} = &\underbrace{\frac{I_{xz}^{DC}}{2} + \frac{KI_{xz,2}}{4}\cos(\beta + \Phi_{xz,2}) - \frac{mI}{8}\cos(\phi)}_{dc-component} \\
&\underbrace{-\frac{I}{4}\sin(\omega t + \phi) + \frac{mI_{xz,2}}{4}\cos(\omega t + \Phi_{xz,2}) + \frac{mI_{xz}^{DC}}{2}\sin(\omega t) - \frac{KI}{8}\cos(\omega t + \beta - \phi)}_{fundamental-component} \\
&\underbrace{+\frac{I_{xz,2}}{2}\sin(2\omega t + \Phi_{xz,2}) + \frac{mI}{8}\cos(2\omega t + \phi) + \frac{KI_{xz}^{DC}}{2}\sin(2\omega t + \beta)}_{2nd-component} \\
&\underbrace{-\frac{mI_{xz,2}}{4}\sin(3\omega t + \Phi_{xz,2}) + \frac{KI}{8}\cos(3\omega t + \beta + \phi)}_{3rd-component} \\
&\underbrace{-\frac{KI_{xz,2}}{4}\cos(4\omega t + \beta + \Phi_{xz,2})}_{4th-component}
\end{aligned}
\tag{A.4}
$$

A.2 Capacitor Ripple Voltage

The capacitor ripple voltage is derived from the capacitor ripple current equation. In fact, each harmonic component of the capacitor ripple voltage can be described as a product of the harmonic current and the capacitor reactance of the corresponding frequency. Consequently, the capacitor ripple of the main harmonic components can be obtained as in the following equations, where C denotes the capacitance of the submodule.

Without Injection

$$
\begin{aligned}
\Delta v_{c_{xu}} = & \underbrace{-\frac{I}{4\omega C}\cos(\omega t+\phi)-\frac{mI_{xz,2}}{4\omega C}\sin(\omega t+\Phi_{xz,2})+\frac{mI_{xz}^{DC}}{2\omega C}\cos(\omega t)}_{fundamental} \\
& \underbrace{-\frac{I_{xz,2}}{4\omega C}\cos(2\omega t+\Phi_{xz,2})+\frac{mI}{16\omega C}\sin(2\omega t+\phi)}_{second} \\
& \underbrace{+\frac{mI_{xz,2}}{12\omega C}\sin(3\omega t+\Phi_{xz,2})}_{Third}
\end{aligned}
\tag{A.5}
$$

$$
\begin{aligned}
\Delta v_{c_{xl}} = & \underbrace{+\frac{I}{4\omega C}\cos(\omega t+\phi)+\frac{mI_{xz,2}}{4\omega C}\sin(\omega t+\Phi_{xz,2})-\frac{mI_{xz}^{DC}}{2\omega C}\cos(\omega t)}_{fundamental} \\
& \underbrace{-\frac{I_{xz,2}}{4\omega C}\cos(2\omega t+\Phi_{xz,2})+\frac{mI}{16\omega C}\sin(2\omega t+\phi)}_{second} \\
& \underbrace{-\frac{mI_{xz,2}}{12\omega C}\sin(3\omega t+\Phi_{xz,2})}_{Third}
\end{aligned}
\tag{A.6}
$$

With Injection

$$\begin{aligned}
&\Delta v_{c_{xuJ}} = \\
&\underbrace{-\frac{I}{4\omega C}\cos(\omega t+\phi) - \frac{mI_{xz,2}}{4\omega C}\sin(\omega t+\Phi_{xz,2}) + \frac{KI}{8\omega C}\sin(\omega t+\beta-\phi) + \frac{mI_{xz}^{DC}}{2\omega C}\cos(\omega t)}_{fundamental} \\
&\underbrace{-\frac{I_{xz,2}}{4\omega C}\cos(2\omega t+\Phi_{xz,2}) + \frac{mI}{16\omega C}\sin(2\omega t+\phi) - \frac{mI_{xz}^{DC}}{4\omega C}\cos(2\omega t+\beta)}_{second} \\
&\underbrace{+\frac{mI_{xz,2}}{12\omega C}\sin(3\omega t+\Phi_{xz,2}) - \frac{KI}{24\omega C}\sin(3\omega t+\beta+\phi)}_{Third} \\
&\underbrace{-\frac{KI_{xz,2}}{16\omega C}\sin(4\omega t+\beta+\Phi_{xz,2})}_{Fourth}
\end{aligned} \tag{A.7}$$

$$\begin{aligned}
&\Delta v_{c_{xlJ}} = \\
&\underbrace{+\frac{I}{4\omega C}\cos(\omega t+\phi) + \frac{mI_{xz,2}}{4\omega C}\sin(\omega t+\Phi_{xz,2}) - \frac{KI}{8\omega C}\sin(\omega t+\beta-\phi) - \frac{mI_{xz}^{DC}}{2\omega C}\cos(\omega t)}_{fundamental} \\
&\underbrace{-\frac{I_{xz,2}}{4\omega C}\cos(2\omega t+\Phi_{xz,2}) + \frac{mI}{16\omega C}\sin(2\omega t+\phi) - \frac{mI_{xz}^{DC}}{4\omega C}\cos(2\omega t+\beta)}_{second} \\
&\underbrace{-\frac{mI_{xz,2}}{12\omega C}\sin(3\omega t+\Phi_{xz,2}) + \frac{KI}{24\omega C}\sin(3\omega t+\beta+\phi)}_{Third} \\
&\underbrace{-\frac{KI_{xz,2}}{16\omega C}\sin(4\omega t+\beta+\Phi_{xz,2})}_{Fourth}
\end{aligned} \tag{A.8}$$

A.3 The voltage ripple on submodule terminal of the upper and lower arm

The voltage ripple on a submodule terminal of the upper and lower arms can be expressed as:

Without Injection

$$\Delta v_{o_{xu}} = -\frac{1}{192\omega C}[24I\cos(\omega t+\phi)+24I_{xz,2}\cos(2\omega t+\Phi_{xz,2})+36mI_{xz,2}\sin(\omega t+\Phi_{xz,2})$$
$$-12m^2I_{xz,2}\cos(\Phi_{xz,2})+24m^2I_{xz}^{DC}\sin(2\omega t)+3m^2I\cos(\omega t+\phi)-18mI\sin(2\omega t+\phi)$$
$$-20mI_{xz,2}\sin(3\omega t+\Phi_{xz,2})-48mI_{xz}^{DC}\cos(\omega t)-3m^2I\cos(3\omega t+\phi)+$$
$$+16m^2I_{xz,2}\cos(2\omega t+\Phi_{xz,2})-4m^2I_{xz,2}\cos(4\omega t+\Phi_{xz,2})+12mI\sin(\phi)] \tag{A.9}$$

$$\Delta v_{o_{xl}} = -\frac{1}{192\omega C}[-24I\cos(\omega t+\phi)+24I_{xz,2}\cos(2\omega t+\Phi_{xz,2})-36mI_{xz,2}\sin(\omega t+\Phi_{xz,2})$$
$$+12m^2I_{xz,2}\cos(\Phi_{xz,2})+24m^2I_{xz}^{DC}\sin(2\omega t)-3m^2I\cos(\omega t+\phi)-18mI\sin(2\omega t+\phi)$$
$$+20mI_{xz,2}\sin(3\omega t+\Phi_{xz,2})+48mI_{xz}^{DC}\cos(\omega t)+3m^2I\cos(3\omega t+\phi)+$$
$$+16m^2I_{xz,2}\cos(2\omega t+\Phi_{xz,2})-4m^2I_{xz,2}\cos(4\omega t+\Phi_{xz,2})+12mI\sin(\phi)] \tag{A.10}$$

With Injection

$$
\begin{aligned}
\Delta v_{o_{xuJ}} = \frac{-1}{192\omega C}&[24I\cos(\omega t+\phi)+24I_{xz,2}\cos(2\omega t+\Phi_{xz,2})+36mI_{xz,2}\sin(\omega t+\Phi_{xz,2})+\\
&+24KI_{xz}^{DC}\cos(2\omega t+\beta)-4M_2^2I\cos(\omega t+\phi)-2M_2^2I\cos(5\omega t+2\beta+\phi)-\\
&-3M_2^2I_{xz,2}\cos(6\omega t+2\beta+\Phi_{xz,2})-12m^2I_{xz,2}\cos(\Phi_{xz,2})+24m^2I_{xz}^{DC}\sin(2\omega t)+\\
&+3m^2I\cos(\omega t+\phi)-18mI\sin(2\omega t+\phi)-20mI_{xz,2}\sin(3\omega t+\Phi_{xz,2})-48mI_{xz}^{DC}\cos(\omega t)+\\
&+16KI\sin(3\omega t+\beta+\phi)+18KI_{xz,2}\sin(4\omega t+\beta+\Phi_{xz,2})+3M_2^2I_{xz,2}\cos(2\omega t+\Phi_{xz,2})+\\
&+6M_2^2I\cos(3\omega t+2\beta-\phi)-3m^2I\cos(3\omega t+\phi)+16m^2I_{xz,2}\cos(2\omega t+\Phi_{xz,2})-\\
&-4m^2I_{xz,2}\cos(4\omega t+\Phi_{xz,2})+12KI_{xz,2}\sin(\beta-\Phi_{xz,2})+12M_2^2I_{xz}^{DC}\sin(4\omega t+2\beta)\\
&+12mI\sin(\phi)-12mKI_{xz}^{DC}\sin(\omega t+\beta)+3mKI\cos(\beta-\phi)-6mKI\cos(2\omega t+\beta-\phi)-\\
&-36mKI_{xz}^{DC}\sin(3\omega t+\beta)-2mKI\cos(2\omega t+\beta+\phi)+5mKI\cos(4\omega t+\beta+\phi)+\\
&+12mKI_{xz,2}\cos(\omega t+\beta-\Phi_{xz,2})-4mKI_{xz,2}\cos(\omega t-\beta+\Phi_{xz,2})-\\
&-15mKI_{xz,2}\cos(3t+\beta+\Phi_{xz,2})+7mKI_{xz,2}\cos(5\omega t+\beta+\Phi_{xz,2})]
\end{aligned}
\tag{A.11}
$$

$$
\begin{aligned}
\Delta v_{o_{xlJ}} = \frac{-1}{192\omega C}[& -24I\cos(\omega t+\phi)+24I_{xz,2}\cos(2\omega t+\Phi_{xz,2})-36mI_{xz,2}\sin(\omega t+\Phi_{xz,2})+ \\
& +24KI_{xz}^{DC}\cos(2\omega t+\beta)+4M_2^2I\cos(\omega t+\phi)+2M_2^2I\cos(5\omega t+2\beta+\phi)- \\
& -3M_2^2I_{xz,2}\cos(6\omega t+2\beta+\Phi_{xz,2})-12m^2I_{xz,2}\cos(\Phi_{xz,2})+24m^2I_{xz}^{DC}\sin(2\omega t)- \\
& -3m^2I\cos(\omega t+\phi)-18mI\sin(2\omega t+\phi)+20mI_{xz,2}\sin(3\omega t+\Phi_{xz,2})+48mI_{xz}^{DC}\cos(\omega t)- \\
& -16KI\sin(3\omega t+\beta+\phi)+18KI_{xz,2}\sin(4\omega t+\beta+\Phi_{xz,2})+3M_2^2I_{xz,2}\cos(2\omega t+\Phi_{xz,2})- \\
& -6M_2^2I\cos(3\omega t+2\beta-\phi)+3m^2I\cos(3\omega t+\phi)+16m^2I_{xz,2}\cos(2\omega t+\Phi_{xz,2})- \\
& -4m^2I_{xz,2}\cos(4\omega t+\Phi_{xz,2})+12KI_{xz,2}\sin(\beta-\Phi_{xz,2})+12M_2^2I_{xz}^{DC}\sin(4\omega t+2\beta)+ \\
& +12mI\sin(\phi)+12mKI_{xz}^{DC}\sin(\omega t+\beta)+3mKI\cos(\beta-\phi)-6mKI\cos(2+\beta-\phi)+ \\
& +36mKI_{xz}^{DC}\sin(3\omega t+\beta)-2mKI\cos(2\omega t+\beta+\phi)+5mKI\cos(4\omega t+\beta+\phi)- \\
& -12mKI_{xz,2}\cos(\omega t+\beta-\Phi_{xz,2})+4mKI_{xz,2}\cos(\omega t-\beta+\Phi_{xz,2})+ \\
& +15mKI_{xz,2}\cos(3t+\beta+\Phi_{xz,2})-7mKI_{xz,2}\cos(5\omega t+\beta+\Phi_{xz,2})]
\end{aligned}
\tag{A.12}
$$

Bibliography

[1] Marco Liserre, Thilo Sauter, and John Y. Hung. Future energy systems: Integrating renewable energy sources into the smart power grid through industrial electronics. *IEEE Industrial Electronics Magazine*, 4(1):18–37, 2010.

[2] Dolf Gielen, Francisco Boshell, Deger Saygin, Morgan D. Bazilian, Nicholas Wagner, and Ricardo Gorini. The role of renewable energy in the global energy transformation. *Energy Strategy Reviews*, 24:38–50, 2019.

[3] Frede Blaabjerg and Ke Ma. Wind energy systems. *Proceedings of the IEEE*, 105(11):2116–2131, 2017.

[4] Dentener F. Gielen D. Grubler A. Jewell J. Klimont Z. Krey V. McCollum D.L. Riahi, K. Energy pathways for sustainable development. *Global Energy Assessment: Toward a Sustainable Future. Eds. Team, GEA Writing.*, 2012.

[5] European commission 2020 europe's climate change opportunity. *COM (2008) 30 Final; European Commission: Brussels, Belgium*, 2008.

[6] CER UIC. Moving towards sustainable mobility: A strategy for 2030 and beyond for the european railway sector, paris. 2012.

[7] Kyoto protocol to the united nations framework convention on climate change. Kyoto. 1998.

[8] International Energy Agency (IEA); International Union of Railways (UIC). Railway handbook 2017—energy consumption and co2 emissions. *Tech. Rep. 6; IEA:*, Paris, 2017.

[9] IMO 2020. Global sulphur limit imo 2020," marpol consolidated edition 2011, fifth ed., imo 2020, london, uk.

[10] Marpol 73/78 2019 guidelines for consistent imple- mentation of the 0.50*International convention on the prevention of pollution from ships*, 2019.

[11] European Commission. New shipping fuel standards to reduce sulphur oxides in the mediterranean by 80*An official website of the European Union*, 2022.

[12] Toshiyuki Yanamoto, Mitsuru Izumi, Minoru Yokoyama, and Katsuya Umemoto. Electric propulsion motor development for commercial ships in japan. *Proceedings of the IEEE*, 103(12):2333–2343, 2015.

[13] Nastaran Shakeri, Mehdi Zadeh, and Jorgen Bremnes Nielsen. Hydrogen fuel cells for ship electric propulsion: Moving toward greener ships. *IEEE Electrification Magazine*, 8(2):27–43, 2020.

[14] Giorgio Sulligoi. All electric ships: present and future after 20 years of research and technical achievements. 2011.

[15] James L. Kirtley, Arijit Banerjee, and Steven Englebretson. Motors for ship propulsion. *Proceedings of the IEEE*, 103(12):2320–2332, 2015.

[16] Giorgio Sulligoi, Andrea Vicenzutti, and Roberto Menis. All-electric ship design: From electrical propulsion to integrated electrical and electronic power systems. *IEEE Transactions on Transportation Electrification*, 2(4):507–521, 2016.

[17] Jan Fredrik Hansen and Frank Wendt. History and state of the art in commercial electric ship propulsion, integrated power systems, and future trends. *Proceedings of the IEEE*, 103(12):2229–2242, 2015.

[18] Bijan Zahedi and Lars E. Norum. Modeling and simulation of all-electric ships with low-voltage dc hybrid power systems. *IEEE Transactions on Power Electronics*, 28(10):4525–4537, 2013.

[19] Bija Zahedi. *Shipboard DC Hybrid Power Systems*. PhD thesis, Norwegian University of Science and Technology, 2014.

[20] D. Bosich, A. Vicenzutti, R. Pelaschiar, R. Menis, and G. Sulligoi. Toward the future: The mvdc large ship research program. In *2015 AEIT International Annual Conference (AEIT)*, pages 1–6, 2015.

[21] Uzair Javaid, Francisco D. Freijedo, Drazen Dujic, and Wim van der Merwe. Mvdc supply technologies for marine electrical distribution systems. *CPSS Transactions on Power Electronics and Applications*, 3(1):65–76, 2018.

[22] Ieee recommended practice for 1 kv to 35 kv medium-voltage dc power systems on ships. *IEEE Std 1709-2018 (Revision of IEEE Std 1709-2010)*, pages 1–54, 2018.

[23] Zheming Jin, Giorgio Sulligoi, Rob Cuzner, Lexuan Meng, Juan C. Vasquez, and Josep M. Guerrero. Next-generation shipboard dc power system: Introduction smart grid and dc microgrid technologies into maritime electrical netowrks. *IEEE Electrification Magazine*, 4(2):45–57, 2016.

[24] Uzair Javaid, Dražen Dujić, and Wim van der Merwe. Mvdc marine electrical distribution: Are we ready? In *IECON 2015 - 41st Annual Conference of the IEEE Industrial Electronics Society*, pages 000823–000828, 2015.

[25] Carlos A. Reusser, Hector A. Young, Joel R. Perez Osses, Marcelo A. Perez, and Oliver J. Simmonds. Power electronics and drives: Applications to modern ship propulsion systems. *IEEE Industrial Electronics Magazine*, 14(4):106–122, 2020.

[26] Castellan Simone. et. al. A review of power electronics equipment for all-electric ship mvdc power systems. *International Journal of Electrical Power Energy Systems*, 96:306–323, 2018.

[27] M. Spichartz, V. Staudt, and A. Steimel. Modular multilevel converter for propulsion system of electric ships. In *2013 IEEE Electric Ship Technologies Symposium (ESTS)*, pages 237–242, 2013.

[28] Kamran Sharifabadi, Lennart Harnefors, Hans-Peter Nee, Staffan Norrga, and Remus Teodorescu. *MMC-HVDC Transmission Technology and MTDC Networks*. 2016.

[29] Sixing Du, Apparao Dekka, Bin Wu, and Navid Zargari. *Fundamentals of Modular Multilevel Converter*. 2018.

[30] Luis Camurca, Marius Langwasser, Rongwu Zhu, and Marco Liserre. Future mvdc applications using modular multilevel converter. In *2020 6th IEEE International Energy Conference (ENERGYCon)*, pages 1024–1029, 2020.

[31] Yogendra Reddy. *High-Power Converters and AC Drives(full)*. 08 2013.

[32] Jose I. Leon, Sergio Vazquez, and Leopoldo G. Franquelo. Multilevel converters: Control and modulation techniques for their operation and industrial applications. *Proceedings of the IEEE*, 105(11):2066–2081, 2017.

[33] Hirofumi Akagi. Classification, terminology, and application of the modular multilevel cascade converter (mmcc). *IEEE Transactions on Power Electronics*, 26(11):3119–3130, 2011.

[34] Anton Lesnicar and Rainer Marquardt. An innovative modular multilevel converter topology suitable for a wide power range. volume 3, page 6 pp. Vol.3, 07 2003.

[35] Rong Zeng, Biao Zhao, Tianyu Wei, Chaoqun Xu, Zhengyu Chen, Jiapeng Liu, Wenpeng Zhou, Qiang Song, and Zhanqing Yu. Integrated gate commutated thyristor-based modular multilevel converters: A promising solution for high-voltage dc applications. *IEEE Industrial Electronics Magazine*, 13(2):4–16, 2019.

[36] Gen Li and Jun Liang. Modular multilevel converters: Recent applications [history]. *IEEE Electrification Magazine*, 10(3):85–92, 2022.

[37] Yu Chen, Shanshan Zhao, Zuoyu Li, Xiaoguang Wei, and Yong Kang. Modeling and control of the isolated dc–dc modular multilevel converter for electric ship medium voltage direct current power system. *IEEE Journal of Emerging and Selected Topics in Power Electronics*, 5(1):124–139, 2017.

[38] Ran Mo, Hui Li, and Yanjun Shi. A phase-shifted square wave modulation (ps-swm) for modular multilevel converter (mmc) and dc transformer for medium voltage applications. *IEEE Transactions on Power Electronics*, 34(7):6004–6008, 2019.

[39] Arber Haxhiu, Ahmed Abdelhakim, Sami Kanerva, and Jostein Bogen. Electric power integration schemes of the hybrid fuel cells and batteries-fed marine vessels—an overview. *IEEE Transactions on Transportation Electrification*, 8(2):1885–1905, 2022.

[40] Peng Wu and Richard Bucknall. Hybrid fuel cell and battery propulsion system modelling and multi-objective optimisation for a coastal ferry. *International Journal of Hydrogen Energy*, 45(4):3193–3208, 2020.

[41] Huicui Chen, Pucheng Pei, and Mancun Song. Lifetime prediction and the economic lifetime of proton exchange membrane fuel cells. *Applied Energy*, 142:154–163, 2015.

[42] Pucheng Pei, Yining Meng, Dongfang Chen, Peng Ren, Mingkai Wang, and Xizhong Wang. Lifetime prediction method of proton exchange membrane fuel cells based on current degradation law. *Energy*, 265:126341, 2023.

[43] Danebergs J. Strømgren T. Aarskog, Fredrik G. and Ø. Ulleberg. Energy and cost analysis of a hydrogen driven high speed passenger ferry. *International Shipbuilding Progress*, 67, 2020.

[44] Armin Letafat, Mehdi Rafiei, Morteza Sheikh, Mosayeb Afshari-Igder, Mohsen Banaei, Jalil Boudjadar, and Mohammad Hassan Khooban. Simultaneous energy management and optimal components sizing of a zero-emission ferry boat. *Journal of Energy Storage*, 28:101215, 2020.

[45] W. Colella R. O'Hayre, S. W. Cha. *Fuel Cell Fundamentals*. John Wiley Sons, Ltd, 2016.

[46] Qi Li, Weirong Chen, Zhixiang Liu, Ming Li, and Lei Ma. Development of energy management system based on a power sharing strategy for a fuel cell-battery-supercapacitor hybrid tramway. *Journal of Power Sources*, 279, 04 2015.

[47] Cor Verdouw, Bedir Tekinerdogan, Adrie Beulens, and Sjaak Wolfert. Digital twins in smart farming. *Agricultural Systems*, 189:103046, 2021.

[48] Vepa. R. *Dynamic modeling, simulation and control of energy generation*. London: Springer, 2013.

[49] Suman Debnath, Jiangchao Qin, Behrooz Bahrani, Maryam Saeedifard, and Peter Barbosa. Operation, control, and applications of the modular multilevel

converter: A review. *IEEE Transactions on Power Electronics*, 30(1):37–53, 2015.

[50] Suman Debnath and Maryam Saeedifard. A new hybrid modular multilevel converter for grid connection of large wind turbines. *IEEE Transactions on Sustainable Energy*, 4(4):1051–1064, 2013.

[51] Tianxiang Yin, Chen Xu, Lei Lin, and Kaiyuan Jing. A sic mosfet and si igbt hybrid modular multilevel converter with specialized modulation scheme. *IEEE Transactions on Power Electronics*, 35(12):12623–12628, 2020.

[52] Shiqi Ji, Li Zhang, Xingxuan Huang, James Palmer, Fred Wang, and Leon M. Tolbert. A novel voltage balancing control with dv/dt reduction for 10-kv sic mosfet-based medium voltage modular multilevel converter. *IEEE Transactions on Power Electronics*, 35(11):12533–12543, 2020.

[53] Saleh Farzamkia, Masoud Noushak, Hossein Iman-Eini, Arash Khoshkbar-Sadigh, and Shahrokh Farhangi. Fault-tolerant method to reduce voltage stress of submodules in postfault condition for regenerative mmc-based drive. *IEEE Transactions on Industrial Electronics*, 68(6):4718–4726, 2021.

[54] Sixing Du, Bin Wu, Kai Tian, Navid R. Zargari, and Zhongyuan Cheng. An active cross-connected modular multilevel converter (ac-mmc) for a medium-voltage motor drive. *IEEE Transactions on Industrial Electronics*, 63(8):4707–4717, 2016.

[55] Binbin Li, Shaoze Zhou, Dianguo Xu, Stephen J. Finney, and Barry W. Williams. A hybrid modular multilevel converter for medium-voltage variable-speed motor drives. *IEEE Transactions on Power Electronics*, 32(6):4619–4630, 2017.

[56] Rong Zeng, Biao Zhao, Tianyu Wei, Chaoqun Xu, Zhengyu Chen, Jiapeng Liu, Wenpeng Zhou, Qiang Song, and Zhanqing Yu. Integrated gate commutated thyristor-based modular multilevel converters: A promising solution for high-voltage dc applications. *IEEE Industrial Electronics Magazine*, 13(2):4–16, 2019.

[57] H. Mohammadi P. and M. Tavakoli Bina. A transformerless medium-voltage statcom topology based on extended modular multilevel converters. *IEEE Transactions on Power Electronics*, 26(5):1534–1545, 2011.

[58] Makoto Hagiwara, Ryo Maeda, and Hirofumi Akagi. Negative-sequence reactive-power control by a pwm statcom based on a modular multilevel cascade converter (mmcc-sdbc). *IEEE Transactions on Industry Applications*, 48(2):720–729, 2012.

[59] Rong Zeng, Lie Xu, Liangzhong Yao, and Barry W. Williams. Design and operation of a hybrid modular multilevel converter. *IEEE Transactions on Power Electronics*, 30(3):1137–1146, 2015.

[60] Yu Jin, Qian Xiao, Josep Pou, Hongjie Jia, Yanchao Ji, Remus Teodorescu, and Frede Blaabjerg. A novel fault-tolerant operation approach for the modular multilevel converter-based statcom with the enhanced operation capability. *IEEE Journal of Emerging and Selected Topics in Power Electronics*, 10(5):5541–5552, 2022.

[61] Zheng Xu, Huangqing Xiao, and Zheren Zhang. Selection methods of main circuit parameters for modular multilevel converters. *IET Renewable Power Generation*, 10(6):788–797, 2016.

[62] Kalle Ilves, Antonios Antonopoulos, Staffan Norrga, and Hans-Peter Nee. Steady-state analysis of interaction between harmonic components of arm and

line quantities of modular multilevel converters. *IEEE Transactions on Power Electronics*, 27(1):57–68, 2012.

[63] Vito G. Monopoli, Abraham Marquez, Jose I. Leon, Marco Liserre, Giampaolo Buticchi, Leopoldo G. Franquelo, and Sergio Vazquez. Applications and modulation methods for modular converters enabling unequal cell power sharing: Carrier variable-angle phase-displacement modulation methods. *IEEE Industrial Electronics Magazine*, 16(1):19–30, 2022.

[64] Makoto Hagiwara and Hirofumi Akagi. Control and experiment of pulsewidth-modulated modular multilevel converters. *IEEE Transactions on Power Electronics*, 24(7):1737–1746, 2009.

[65] Apparao Dekka, Bin Wu, Navid R. Zargari, and Ricardo Lizana Fuentes. Dynamic voltage balancing algorithm for modular multilevel converter: A unique solution. *IEEE Transactions on Power Electronics*, 31(2):952–963, 2016.

[66] Minyuan Guan, Zheng Xu, and Hairong Chen. Control and modulation strategies for modular multilevel converter based hvdc system. In *IECON 2011 - 37th Annual Conference of the IEEE Industrial Electronics Society*, pages 849–854, 2011.

[67] Pengfei Hu and Daozhuo Jiang. A level-increased nearest level modulation method for modular multilevel converters. *IEEE Transactions on Power Electronics*, 30(4):1836–1842, 2015.

[68] Apparao Dekka, Bin Wu, Navid R. Zargari, and Ricardo Lizana Fuentes. A space-vector pwm-based voltage-balancing approach with reduced current sensors for modular multilevel converter. *IEEE Transactions on Industrial Electronics*, 63(5):2734–2745, 2016.

[69] Fujin Deng, Yanjun Tian, Rongwu Zhu, and Zhe Chen. Fault-tolerant approach for modular multilevel converters under submodule faults. *IEEE Transactions on Industrial Electronics*, 63(11):7253–7263, 2016.

[70] Jinyu Wang and Yi Tang. A fault-tolerant operation method for medium voltage modular multilevel converters with phase-shifted carrier modulation. *IEEE Transactions on Power Electronics*, 34(10):9459–9470, 2019.

[71] Weixing Lin, Dragan Jovcic, Samuel Nguefeu, and Hani Saad. Full-bridge mmc converter optimal design to hvdc operational requirements. *IEEE Transactions on Power Delivery*, 31(3):1342–1350, 2016.

[72] Yaqian Zhang, Jianzhong Zhang, and Fujin Deng. Improved cps-pwm approach for over-modulation operations of hybrid modular multilevel converter. *IEEE Journal of Emerging and Selected Topics in Power Electronics*, 10(5):5933–5943, 2022.

[73] Qiang Song, Wenhua Liu, Xiaoqian Li, Hong Rao, Shukai Xu, and Licheng Li. A steady-state analysis method for a modular multilevel converter. *IEEE Transactions on Power Electronics*, 28(8):3702–3713, 2013.

[74] Ricardo Lizana, Marcelo A. Perez, David Arancibia, Jose R. Espinoza, and Jose Rodriguez. Decoupled current model and control of modular multilevel converters. *IEEE Transactions on Industrial Electronics*, 62(9):5382–5392, 2015.

[75] Yunhu Yang, Keliang Zhou, and Ming Cheng. Phase compensation resonant controller for pwm converters. *IEEE Transactions on Industrial Informatics*, 9(2):957–964, 2013.

[76] Alessandro Lidozzi, Chao Ji, Luca Solero, Pericle Zanchetta, and Fabio Crescimbini. Resonant–repetitive combined control for stand-alone power supply units. *IEEE Transactions on Industry Applications*, 51(6):4653–4663, 2015.

[77] Alessandro Lidozzi, Marco Di Benedetto, Stefano Bifaretti, Luca Solero, and Fabio Crescimbini. Resonant controllers with three degrees of freedom for ac power electronic converters. *IEEE Transactions on Industry Applications*, 51(6):4595–4604, 2015.

[78] Prapart Ukakimaparn, Mathee Khwunthong, Thanit Trisuwannawat, and Pittaya Pannil. Discrete-time pida controller designed by tustin's method with and without frequency pre-warping. In *2018 3rd International Conference on Control and Robotics Engineering (ICCRE)*, pages 119–124, 2018.

[79] Yalong Li, Edward A. Jones, and Fei Wang. The impact of voltage-balancing control on switching frequency of the modular multilevel converter. *IEEE Transactions on Power Electronics*, 31(4):2829–2839, 2016.

[80] Apparao Dekka, Bin Wu, Navid R. Zargari, and Ricardo Lizana Fuentes. Dynamic voltage balancing algorithm for modular multilevel converter: A unique solution. *IEEE Transactions on Power Electronics*, 31(2):952–963, 2016.

[81] Apparao Dekka, Bin Wu, Ricardo Lizana Fuentes, Marcelo Perez, and Navid R. Zargari. Evolution of topologies, modeling, control schemes, and applications of modular multilevel converters. *IEEE Journal of Emerging and Selected Topics in Power Electronics*, 5(4):1631–1656, 2017.

[82] Jiangchao Qin and Maryam Saeedifard. Reduced switching-frequency voltage-balancing strategies for modular multilevel hvdc converters. *IEEE Transactions on Power Delivery*, 28(4):2403–2410, 2013.

[83] Arman Hassanpoor, Staffan Norrga, Hans-Peter Nee, and Lennart Ängquist. Evaluation of different carrier-based pwm methods for modular multilevel converters for hvdc application. In *IECON 2012 - 38th Annual Conference on IEEE Industrial Electronics Society*, pages 388–393, 2012.

[84] Shengfang Fan, Kai Zhang, Jian Xiong, and Yaosuo Xue. An improved control system for modular multilevel converters with new modulation strategy and voltage balancing control. *IEEE Transactions on Power Electronics*, 30(1):358–371, 2015.

[85] Frederik Hahn, Markus Andresen, Giampaolo Buticchi, and Marco Liserre. Thermal analysis and balancing for modular multilevel converters in hvdc applications. *IEEE Transactions on Power Electronics*, 33(3):1985–1996, 2018.

[86] Qingrui Tu, Zheng Xu, and Lie Xu. Reduced switching-frequency modulation and circulating current suppression for modular multilevel converters. *IEEE Transactions on Power Delivery*, 26(3):2009–2017, 2011.

[87] Lennart Angquist, Antonios Antonopoulos, Daniel Siemaszko, Kalle Ilves, Michail Vasiladiotis, and Hans-Peter Nee. Open-loop control of modular multilevel converters using estimation of stored energy. *IEEE Transactions on Industry Applications*, 47(6):2516–2524, 2011.

[88] Germán Pizarro, Pablo Poblete, Gabriel Droguett, Javier Pereda, and Felipe Núñez. Extended kalman filtering for full-state estimation and sensor reduction in modular multilevel converters. *IEEE Transactions on Industrial Electronics*, 70(2):1927–1938, 2023.

[89] Stefano Fabbri, Davide D'Amato, Marco Palmieri, Francesco Cupertino, Matthias Nienhaus, and Emanuele Grasso. Performance comparison of different estimation techniques of the external load-torque applied on a pmsm using

direct flux control. In *2020 International Symposium on Power Electronics, Electrical Drives, Automation and Motion (SPEEDAM)*, pages 688–693, 2020.

[90] Zixin Li, Ping Wang, Zunfang Chu, Haibin Zhu, Yongjie Luo, and Yaohua Li. An inner current suppressing method for modular multilevel converters. *IEEE Transactions on Power Electronics*, 28(11):4873–4879, 2013.

[91] Shaohua Li, Xiuli Wang, Zhiqing Yao, Tai Li, and Zhong Peng. Circulating current suppressing strategy for mmc-hvdc based on nonideal proportional resonant controllers under unbalanced grid conditions. *IEEE Transactions on Power Electronics*, 30(1):387–397, 2015.

[92] Pengfei Hu, Zhengxu He, Shuqi Li, and Josep M. Guerrero. Non-ideal proportional resonant control for modular multilevel converters under sub-module fault conditions. *IEEE Transactions on Energy Conversion*, 34(4):1741–1750, 2019.

[93] Liqun He, Kai Zhang, Jian Xiong, and Shengfang Fan. A repetitive control scheme for harmonic suppression of circulating current in modular multilevel converters. *IEEE Transactions on Power Electronics*, 30(1):471–481, 2015.

[94] Shunfeng Yang, Peng Wang, Yi Tang, Michael Zagrodnik, Xiaolei Hu, and King Jet Tseng. Circulating current suppression in modular multilevel converters with even-harmonic repetitive control. *IEEE Transactions on Industry Applications*, 54(1):298–309, 2018.

[95] Limin Yang, Yaohua Li, Zixin Li, Ping Wang, Shukai Xu, and Ruifeng Gou. Loss optimization of mmc by second-order harmonic circulating current injection. *IEEE Transactions on Power Electronics*, 33(7):5739–5753, 2018.

[96] Jiangchao Qin and Maryam Saeedifard. Predictive control of a modular multilevel converter for a back-to-back hvdc system. *IEEE Transactions on Power Delivery*, 27(3):1538–1547, 2012.

[97] Jianzhao Wei, Anirudh Budnar Acharya, Lars Norum, and Pavol Bauer. Comparison of current control strategies in modular multilevel converter. In *2018 International Power Electronics Conference (IPEC-Niigata 2018 -ECCE Asia)*, pages 2630–2637, 2018.

[98] R. Picas, J. Pou, S. Ceballos, J. Zaragoza, G. Konstantinou, and V. G. Agelidis. Optimal injection of harmonics in circulating currents of modular multilevel converters for capacitor voltage ripple minimization. In *2013 IEEE ECCE Asia Downunder*, pages 318–324, 2013.

[99] Josep Pou, Salvador Ceballos, Georgios Konstantinou, Vassilios G. Agelidis, Ricard Picas, and Jordi Zaragoza. Circulating current injection methods based on instantaneous information for the modular multilevel converter. *IEEE Transactions on Industrial Electronics*, 62(2):777–788, 2015.

[100] Jun Wang, Xu Han, Hao Ma, and Zhihong Bai. Analysis and injection control of circulating current for modular multilevel converters. *IEEE Transactions on Industrial Electronics*, 66(3):2280–2290, 2019.

[101] Xiaoqian Li, Qiang Song, Wenhua Liu, Shukai Xu, Zhe Zhu, and Xiaolin Li. Performance analysis and optimization of circulating current control for modular multilevel converter. *IEEE Transactions on Industrial Electronics*, 63(2):716–727, 2016.

[102] Can Wang, Quanrui Hao, and Boon Teck Ooi. Reduction of low-frequency harmonics in modular multilevel converters (mmcs) by harmonic function analysis. *Generation, Transmission Distribution, IET*, 8:328–338, 02 2014.

[103] Deliang Wu and Li Peng. Analysis and suppressing method for the output voltage harmonics of modular multilevel converter. *IEEE Transactions on Power Electronics*, 31(7):4755–4765, 2016.

[104] Kalle Ilves, Staffan Norrga, Lennart Harnefors, and Hans-Peter Nee. On energy storage requirements in modular multilevel converters. *IEEE Transactions on Power Electronics*, 29(1):77–88, 2014.

[105] Antonios Antonopoulos, Lennart Ängquist, Lennart Harnefors, and Hans-Peter Nee. Optimal selection of the average capacitor voltage for variable-speed drives with modular multilevel converters. *IEEE Transactions on Power Electronics*, 30(1):227–234, 2015.

[106] Gaopeng Guo, Qiang Song, Wenbo Yang, Yu Wang, Wenhua Liu, Hong Rao, and Shukai Xu. Application of third-order harmonic voltage injection in a modular multilevel converter. *IEEE Transactions on Industrial Electronics*, 65(7):5260–5271, 2018.

[107] Ming Huang, Zhen Kang, Weilin Li, Jianlong Zou, Xikui Ma, and Jianhua Li. Modified modular multilevel converter with third-order harmonic voltage injection to reduce submodule capacitor voltage ripples. *IEEE Transactions on Power Electronics*, 36(6):7074–7086, 2021.

[108] Zhijie Liu, Ke-Jun Li, Jinyu Wang, Wentao Liu, Zahid Javid, and Zhuo-di Wang. General model of modular multilevel converter for analyzing the steady-state performance optimization. *IEEE Transactions on Industrial Electronics*, 68(2):925–937, 2021.

[109] Stefano Bifaretti, Alessandro Lidozzi, Luca Solero, and Fabio Crescimbini. Modulation with sinusoidal third-harmonic injection for active split dc-bus four-leg inverters. *IEEE Transactions on Power Electronics*, 31(9):6226–6236, 2016.